# *Coherent far-infrared excitation processes with ultrafast pulses in multilevel systems*

ISBN/EAN `978-90-9023323-9`

Coherent far-infrared excitation processes with ultrafast pulses in multilevel systems

PhD Thesis Radboud University Nijmegen
With summary in Dutch
Design: Cover by Julio D. Meijer and LaTeX-style by Mark P.J. van de Loo
Printed by `PrintPartners Ipskamp, Enschede (2008)`
Typeset by LaTeX

# *Coherent far-infrared excitation processes with ultrafast pulses in multilevel systems*

Een wetenschappelijke proeve op het gebied van de
Natuurwetenschappen, Wiskunde en Informatica

Proefschrift

ter verkrijging van de graad van doctor
aan de Radboud Universiteit Nijmegen
op gezag van de rector magnificus prof. mr. S.C.J.J. Kortmann,
volgens besluit van het College van Decanen
in het openbaar te verdedigen op vrijdag 26 september 2008
om `13:30` uur precies

door

Afric Simone Meijer

geboren op 30 maart 1977
te Amsterdam

| | |
|---|---|
| Promotor: | Prof. dr. W.J. van der Zande |
| Manuscriptcommissie: | Prof. dr. J.J. ter Meulen (voorzitter)<br>Dr. E. Bründermann (Ruhr-Universität Bochum)<br>Dr. H.L. Offerhaus (Universiteit Twente) |

This research has been financially supported by Stichting Technische Wetenschappen (STW). Part of the research is funded by Stichting voor Fundamenteel Onderzoek der Materie (FOM) and the Netherlands Organization for Scientific Research (NWO).

*Voor mijn ouders en grote broer,*

## *Publications*

*Imaging of terahertz radiation using a Rydberg atom photocathode*
A. Gürtler, A.S. Meijer and W.J. van der Zande
Applied Physics Letters, 83 (2), 222 (2003)

*Controlling rotational state distribution using two-pulse stimulated Raman excitation*
A.S. Meijer, Y. Zhang, D.H. Parker, A. Gijsbertsen, M.J.J. Vrakking and W.J. van der Zande
Physical Review A, 76, 023411 (2007)

*A simple cesium iodine prism based terahertz spectrometer*
A.S. Meijer, J.J.H. Pijpers, H.K. Nienhuys, M. Bonn and W.J. van der Zande
(Submitted to Journal of Optics A)

*Effects of narrow band pulse shaping on a resonant multilevel system*
A.S. Meijer, A.V. Kimel, Th. Rasing and W.J. van der Zande
(Submitted to Physical Review A)

*Velocity map imaging of atomic and molecular processes at the free electron laser in Hamburg (FLASH)*
P. Johnsson, W. Siu, A. Gijsbertsen, J. Verhoeven, A.S. Meijer, W.J. van der Zande and M.J.J. Vrakking
(Journal of Modern Optics, inprint)

# Contents

# CHAPTER 1

# Light and matter - A brief history

This thesis describes experimental research, in which the interaction between matter and radiation is present in every aspect. Coherent radiation from lasers, in the form of a terahertz half-cycle pulse or a femtosecond optical pulse, is on purpose modified in order to manipulate the atomic or molecular interaction.

The research started with the construction of a prototype real-time far-infrared camera based on ionization of gas-phase Rydberg atoms. Such a photosensitive layer, i.e. photocathode, is sensitive for coherent as well as incoherent radiation. The radiation, we used, and the atoms, we prepared, stress the importance of nonlinear processes.

We modify radiation in such a manner that we steer the light-matter interaction and control the generation of product states. Here, we combine optical physics, atomic and molecular physics, and quantum mechanics to utilize the fundamental principle of quantum interference.

We emphasize in this introduction the coherent light-matter interaction of ultrafast pulses and the consequence of deforming the temporal pulse structure. Therefore, aspects concerning the far-infrared spectrometer and far-infrared camera are not included in the introduction, but are discussed in detail in their Chapters. The introduction will give an elucidation of what is radiation and how manipulation of light and with light can be achieved.

A.S. Meijer

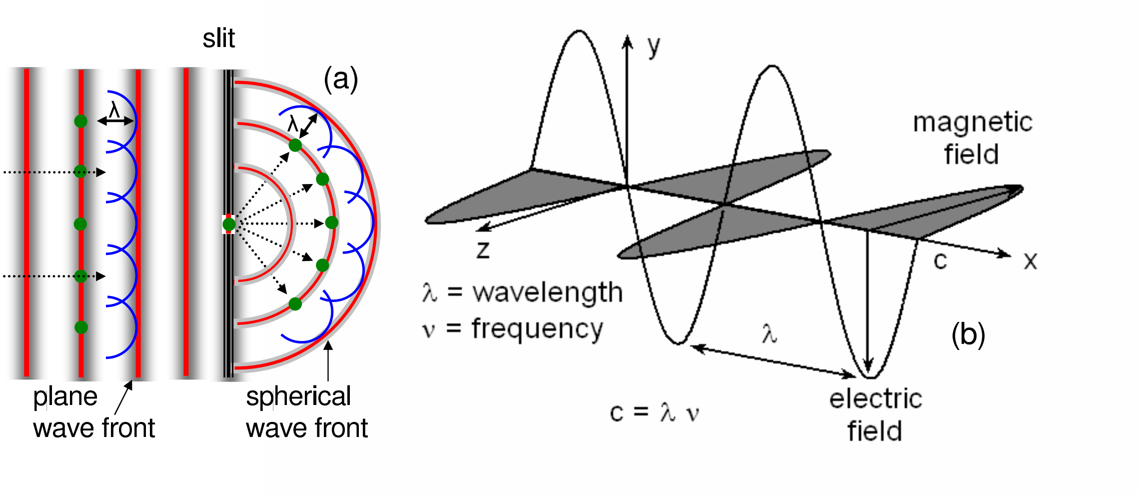

**Figure 1.1:** (a) Diffraction becomes evident when the wavelength of a propagating monochromatic plane wave has the same dimension as openings and obstacles. On a screen, only the outcome of the interference between spherical wavelets is observed. (b) Orthogonal electric and magnetic field of a plane polarized wave. The $\vec{E}$-field is considerably more effective at exerting forces and doing work on charges than the $\vec{B}$-field. Therefore, we refer to $\vec{E}$ as the optical field.

## 1.1 Light

One of the earliest physicists to suggest that light was wave-like in nature was Fransesco Grimaldi in 1666[1]. He introduced a beam of sunlight through a hole into a dark room and observed the shadow cast upon a white surface. To his surprise, the shadow was wider than the computed geometrical shadow; moreover, it was bordered by one, two, and sometimes three colored bands. Grimaldi was observing the bending of light, something he called "diffractio", today known as "diffraction"[2,3].

It was this observation of the "phenomenon of colours" that attracted Isaac Newton to the study of optics. In the 1670s, Newton investigated the refraction of light, demonstrating that a prism could decompose white light into a color spectrum and concluding that light was corpuscular, i.e. made up of "particles". Although Newton was aware of the diffraction of light and interference effects (the Newton rings between two surfaces), his convictions were mainly made to account for the rectilinear propagation of light. The corpuscular theory was at the same time heavily debated by Robert Hooke and Christian Huygens, who argued that a wave-theory could best explain the appearance of a color spectrum and the phenomena of reflection, refraction and diffraction. In 1678, Huygens formulated his principle of light waves: "every point on a wave front is a source of new spherical secondary wavelets" (Fig. 1.1(a)), like ripples in water.

However, the corpuscular view did not die easily. Until early in the 19th century, when Thomas Young did his famous experiment observing diffraction from two closely spaced slits. He explained his results with a new fundamental concept, the so-called "Principle of Interference", and deduced that light must propagate as waves. Unaware of the effort of Young, Augustin-Jean Fresnel successfully modified Huygens' wave-theory by mathematically adding in the concept of interference and soon scientists were convinced that light must be a wave.

In 1872, James Clerk Maxwell made it evident that light is electromagnetic in nature with wave-like behavior. This leads to the picture of a continuous transfer of energy through time-varying electric and magnetic fields, which mutually induce each other. The combined electromagnetic field propagates with the speed of light $c$ of 299 792 458 m/s through vacuum (Fig. 1.1(b)).

Maxwell died at the age of 48, eight years too soon to see the experimental confirmation. Heinrich Hertz verified the existence of electromagnetic waves by generating and detecting radio frequencies. He also discovered the photoelectric effect: the phenomenon in certain metals, which produces an electrical potential when exposed to light. As scientists studied the photoelectric effect, it became clear that the wave-theory could not account for this behavior; in fact, the effect seemed to indicate the presence of light "particles". For the first time in more than a century there was new support for Newton's corpuscular theory of light.

The dual nature of light became more evident when in 1900, Max Planck formulated his famous Planck-black-body radiation law by including the statistical mechanics of Boltzman. The physical interpretation was the so-called "quantum" (Latin, "how much") hypothesis: electromagnetic energy from a black-body could only be emitted in quantized form and is a multiple of the elementary unit $h$, known as Planck's constant ($6.626 \cdot 10^{-34} Js$).

Building on these ideas, Albert Einstein proposed in 1905 a new form of the corpuscular theory. Electromagnetic interaction can be described as a transport of energy in terms of massless elementary "particles", known as "photons", and each photon has an energy $E$ proportional to its frequency $\nu$, that is

$$E = h\nu. \tag{1.1}$$

The dual nature of light is apparent by the fact that it propagates through space in a wave-like fashion and yet displays particle-like behavior during the process of emission and absorption. Electromagnetic radiation is created and destroyed in quanta or photons. Nonetheless, its motion through a lens, a hole or a set of slits is governed by wave characteristics.

## 1.2 Matter

Light can be seen as the most tenuous form of matter and its apparent wave-like motion is in "quantum mechanics" applied to all particles like atoms, electrons, protons or whatever. If we are unfamiliar with the wave-like behavior of matter in the macroscopic world, it is because the particle wavelengths are too small to be observed in daily life.

The phrase "quantum mechanics" was first introduced in 1924 by Max Born. However, the quantum was already included by Niels Bohr in his theory on discrete atomic spectra: a planetary picture where the orbit of electrons around the core can only have discrete values and the quantum jump of the electron to another orbit equals the energy of a photon $E$. By the end of 1920s, through the effort of Born, Heisenberg, Schrödinger, De Broglie, Pauli, Dirac, and many others, quantum mechanics had become a well-verified theory. The great insight of Erwin Schrödinger in 1925 was

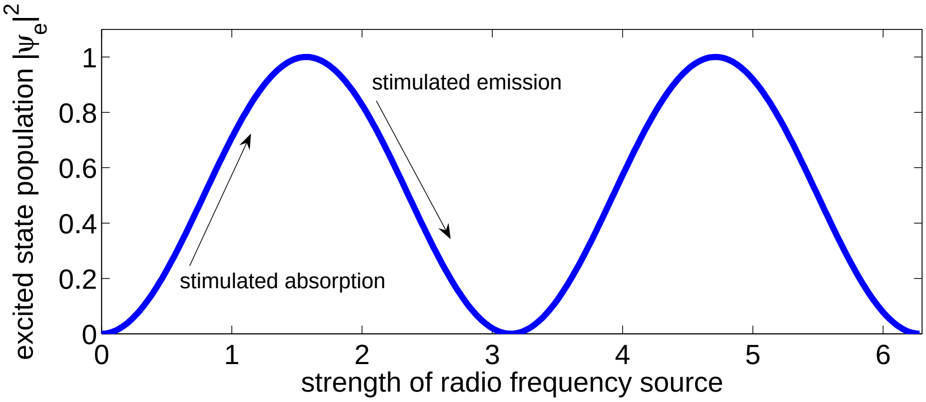

**Figure 1.2:** Rabi-cycling: the system is usually in a superposition of the ground $\psi_g$ and excited state $\psi_e$. The excited state probability ($P_e \equiv |\psi_e|^2$) oscillates with increasing strength of the radio frequency source. These oscillations went beyond Einstein's prediction that stimulated emission would prevent population inversion.

to express the wave-like motion of matter as a complex plane wave, thereby properly including the concept of interference as a phase factor. The well-known and famous Schrödinger equation reads[4]

$$i\hbar\frac{\partial}{\partial t}\Psi(t) = H\Psi(t), \tag{1.2}$$

where $H$ is the Hamiltonian operator of an atom or molecule and is associated with the energy of a system. This operator contains all possible outcomes of a measurement. The statevector $\Psi(t)$ can be written as a superposition of time-independent quantum states $\psi_n$, known as eigenstates with eigenenergy $E_n$, where n = 1,2,3,.., and may be written as

$$\begin{aligned}\Psi(r,t) &= C_1(t)\psi_1(r)e^{-iE_1t/\hbar} \\ &\quad + C_2(t)\psi_2(r)e^{-iE_2t/\hbar} + C_3(t)\psi_2(r)e^{-iE_3t/\hbar} + ... \\ &= \sum_{n=1}^{m} C_n(t)\psi_n(r)e^{-iE_nt/\hbar}.\end{aligned} \tag{1.3}$$

Light interacting with matter is mostly described by the electromagnetic field equation of Maxwell as a plane wave $\cos(\frac{E}{\hbar}t)$. The wave-like behavior of matter in its interaction with light was first visualized[a] by Isidor Rabi who in 1938 developed the nuclear magnetic resonance (NMR) technique[5]. Rabi measured with radio frequency sources the predicted quantum mechanical effect of an oscillating excited state population in a two-level system. These oscillations are nowadays known as Rabi-cycles (Fig. 1.2) and are defined as a periodic change between stimulated absorption and the re-emittance of photons by stimulated emission.

In similar two-level systems, his former PhD-student Norman Ramsey measured the production of excited atoms when using two separated radio sources[6]. The amount of excited molecules grows and dwindles when varying the velocity of the molecular

---

[a] I refer to the prediction that the related phase of wave functions determine the outcome of the interaction.

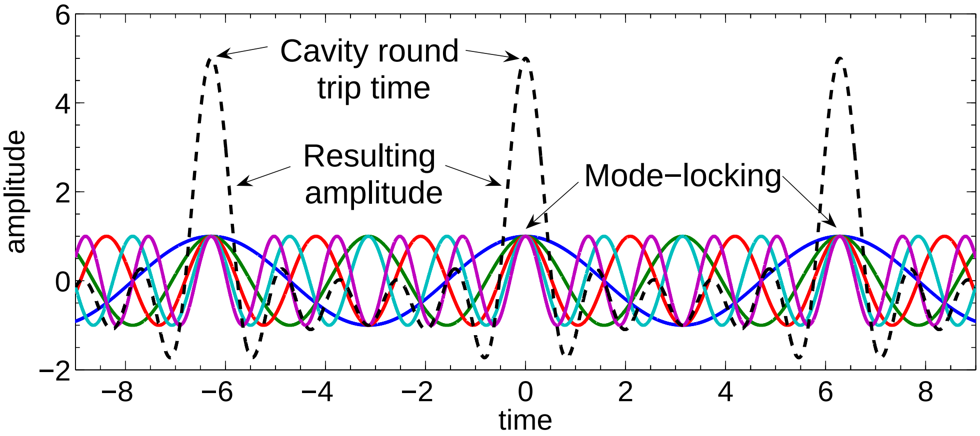

**Figure 1.3:** Mode-locking techniques produce short pulses by forcing modes (frequencies or waves) in a laser cavity to have the same phase relation. All waves of different frequency will then interfere constructively at one point, resulting in a very intense and short burst of light, while elsewhere destructive interference occurs. Pulse compression techniques are based on the same principle of mode-locking.

beam. From a quantum mechanical point of view, the observed oscillations are the result of interfering state population via different quantum mechanical pathways to the same final state: one excitation path in the first source and the other path in the second source. In a semiclassical picture, this process can be seen as the absorption and stimulated emission of photons.

The nearly single radio frequency with a well defined phase was an ideal source to perform coherent spectroscopy. Before these quantum phenomenons could be observed in the optical domain, scientists had to wait 20 years until the advent of the laser.

## 1.3 The laser

In the 1960s, Theodore Maiman was the first to prove experimentally the function of a laser using a ruby crystal, almost 50 years after Einstein proposed his theory on stimulated emission. This process is the reverse process of absorption and is capable of triggering an avalanche of photons - all in-phase. Light Amplification by Stimulated Emission of Radiation (laser) is a quantum mechanical device that manages to produce "marvelous light".

The advent of the colliding pulse mode-lock (CPM) ring dye laser[7] in 1981 made it possible to produce pulses below 100 fs (1 fs = $10^{-15}$ s). By the mid-1980s, mode-locking and nonlinear pulse compression techniques (Fig. 1.3) produce pulses as short as 6 fs in the visible, which corresponds to only a few optical cycles[8,9]. In the 1990s, the solid-state Ti:sapphire femtosecond laser brought a substantial improvement with advantages in the production of extremely short (<5 fs) and powerful pulses[10].

These accomplishments have established a new field of research known as "ultrafast phenomena" and nowadays, pulses as short as 0.65 fs are produced at XUV frequencies[11,12]. Confining energy in such ultra short pulses implies an enormous peak intensity ($> 10^{12}\ Wcm^{-2}$). Moreover, according to the uncertainty principle ($\Delta E \Delta t \approx \frac{\hbar}{2}$), it also implies a wide range of frequencies with all well-defined phases. Easily, the visible femtosecond light pulses are converted to UV, near- and far-infrared radiation by nonlinear processes in birefringent crystals, semiconductors and polymers. For instance, a biased semiconductor illuminated with femtosecond pulses, generates far-infrared pulses of $\approx 475$ fs with a nearly "white light" spectrum extending from 1000 - 100 $\mu m$ (see Section 7.2)[13–17].

Such short pulses have made it possible to drive various multiphoton processes within a single pulse. In the following paragraph, we show that the light pulses can be used to imprint information on atoms and molecules in such a manner that their dynamics are controlled and that the excitation process leads to a desirable outcome.

## 1.4 Coherent control

Since the advent of the laser, scientists have tried to use laser light to manipulate atomic and molecular processes, and chemical reactions[10,18,19]. The initial idea was simple: tune the single-frequency light source to the characteristic frequency of a bond you wish to break and increase the intensity of the laser. It was assumed that the molecule would fall apart with a minimal amount of byproducts. However, in the laboratory this idea was a complete failure. The energy that was pumped into specific bonds redistributes itself throughout the molecule on a femtosecond to picosecond timescale. This process of intramolecular vibrational redistribution (IVR) is simply explained in quantum mechanical terms: the states that carry the transition strength are not pure eigenstates. Increasing the energy only broke the weakest bond in the molecule and no control seemed possible. The decoherence of quantum states spoiled the dream of scientist to use photons as "reagents" in chemical reaction and manipulate matter with light.

However, in the late 1980s, scientist realized that atomic and molecular quantum states are waves that can interfere. The manipulation of these quantum interference is called "coherent control": the ability to steer a quantum mechanical reaction towards a desired final state through its interaction with light, while canceling out other paths leading to undesired outcomes" (Fig. 1.4)[20]. Coherently controlling quantum mechanical systems involves multiphoton excitation and multilevel systems. In the late 1980s, two schemes, both utilizing interfering pathways, have been demonstrated to be successful in achieving quantum control in atomic and small molecular systems[21,22].

### 1.4.1 Intermezzo: decoherence of quantum interference

The term interference is in close connection with Young's double-slit experiment in optics and refers to a "coherent" interaction of two or more waves having a well-defined phase with respect to each other[2]. From the resulting intensity, one can conclude whether the waves, i.e. frequencies, are in phase or out of phase. The term coherence is directly related to the visibility of the interference pattern. This requires an overlap of a wave front in a finite time interval $\Delta t_c = \frac{1}{\Delta\nu}$ and in a finite extent in space $\Delta L = \frac{c}{\Delta\nu}$. However, quantum mechanical interference processes are not restricted by these classical assumptions. For instance, the separated oscillatory fields in the Ramsey experiment[6] had no spatial overlap and in a two-pulse experiment

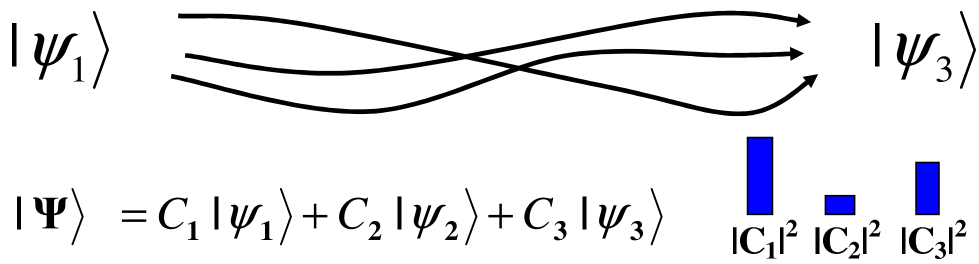

**Figure 1.4:** Coherent control in atoms or molecules is accomplished by manipulating the inference of different quantum mechanical pathways to the same final state through its interaction with light.

as described in Chapter 3, the gaussian pulses of 100 fs ($\Delta\nu = 4.41$ THz) have no temporal coherence for time delays larger than 227 fs. Nevertheless, in both cases interference patterns are measured.

In quantum mechanics, the visibility of quantum interference is limited by the time of a quantum state to remain in a coherent superposition. Due to spontaneous emission, IVR or to its unavoidable interaction with the environment, quantum states lose their coherence. Therefore, the term "decoherence time" replaces the classical "coherence time"[18]. Within this decoherence time, an atom or molecule can be coherently excited multiple times. For instance, in Chapter 3, the first femtosecond pulse initiates a "phase clock" $\Delta\phi$ in the plane of excited NO molecules and depending on the time delay $\Delta T$ of the second pulse, constructive ($n\Delta T\omega_{J,J'} = \Delta\phi_{J,J'}$) or destructive interference ($(n+\frac{1}{2})\Delta T\omega_{J,J'} = \Delta\phi_{J,J'}$) populates or depletes specific rotational states ($\omega_{J,J'}$ is the rotational transition frequency).

### 1.4.2 Quasi cw laser

Brumer and Shapiro developed a theoretical approach of two phase-locked quasi cw lasers exciting two different quantum mechanical pathways leading to the same final state (Fig. 1.5(a))[18,25]. The interference is constructive or destructive, depending on the relative phase between the two lasers, $\Delta\phi = \phi_\omega - \phi_{3\omega}$. This technique was first utilized by Elliot to demonstrate the controlled modulation of the ionization probability in mercury[26], quickly followed by many experimentalists showing the control on photoexcitation in HI, photodissociation in $H_2S$, $CH_3I$ and $Na_2$, and photo-generated carriers in semiconductors[27–31]. A particularly interesting scheme in the strong field has been stimulated Raman adiabatic passage (STIRAP)[32] and is depicted in Fig. 1.6. Bergman *et al.*[32] used two narrow band nanosecond lasers to accomplish complete population transfer from an initial state to a selected final state.

### 1.4.3 Pulse laser

The approach with quasi cw lasers has been quite successful. However, propelled by the rapid development of the solid-state Ti:sapphire femtosecond laser, Tannor, Kosloff and Rice suggested an alternative scheme using pairs of short pulses. This

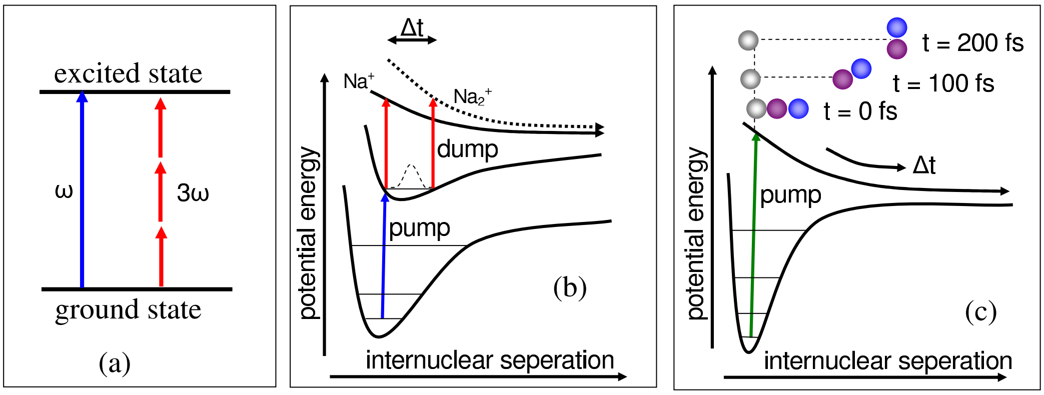

**Figure 1.5:** (a) The contribution of an one- and a three-photon process interferes in the same final state and is coherently controlled by the relative phase of the two lasers $\Delta\phi$. (b) $Na_2$ is pumped into a higher energetic state. The production of $Na_2^+$ is favorable when the excitation is at the inner turning point, whereas the excited $Na_2$ decays to the $Na^+$ product if excitation is at the outer turning point[23]. (c) ICN $\rightarrow$ I+CN: the molecule is pumped into a higher energetic state. A probe frequency corresponding to a particular bond distance is scanned for several time delays. The probe laser is then set to a different frequency and a new time delay scan is taken. The compilation of all data sets shows the bond stretching until it breaks[24].

scheme became the major playground of coherent control[21,33]. In a pump-dump (or pump-pump) scheme, as depicted in Fig. 1.5(b)[23], the evolution of photoexcited molecular wave packets is controlled by the time delay between the pulses. For specific time delays, the $Na_2^+/Na^+$-ratio is enhanced or reduced by dumping the wave packet in a particular channel. This scheme has been successfully incorporated in controlling the fragmentation of molecules[34–36]. In the 1980s, Zewail used the pump-dump scheme to obtain femtosecond "snap shots" of the dynamics in molecules. Figure 1.5(c) illustrates how for the first time, in slow motion, the breaking of a molecular bond could be followed[24,37]. For this discovery, he received the Nobel Prize in 1999. While Zewail probed the intrinsic time-dependence of the intramolecular processes, the desire in coherent control is to manipulate these atomic and molecular dynamics.

Because the pulse duration is considerably shorter than all life- and decoherence times involved, it is possible to drive various multiphoton processes in a multilevel system within a single femtosecond pulse. By shaping the light pulses, the transition rate to a final state is modified and the phases of interfering quantum mechanical pathways are controlled. New techniques were developed, able to tailor the temporal profile of a single femtosecond pulse in such a way that what is accomplished with pulse pairs can be done within one single femtosecond pulse.

## 1.5 Ultrafast pulse shaping

In "ultrafast phenomena", the used electromagnetic energy is confined in time to an ultrashort pulse. The time-dependent electric field $\varepsilon(t)$ may be written as a pure real

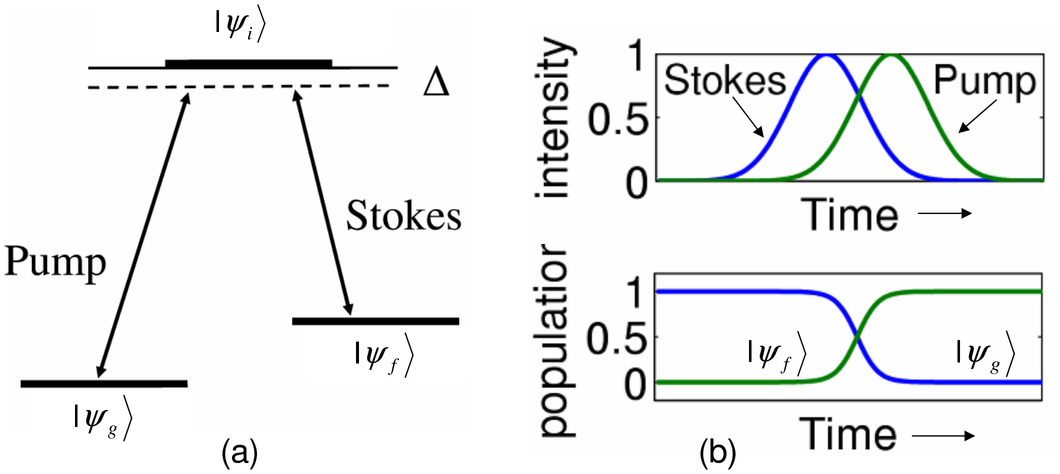

**Figure 1.6:** (a) STIRAP: two separated laser pulses couple in a $\Lambda$-system the ground $|\psi_g\rangle$ to the final $|\psi_f\rangle$ state via the intermediate $|\psi_i\rangle$. (b) A counterintuitive pulse sequence, first the Stokes and then partially overlapping in time the pump pulse, transfers through the process of adiabatic passage the complete ground state population to the final state, while never populating the intermediate state.

oscillating wave given by[10]

$$\varepsilon(t) = \varepsilon_0(t)\cos(\omega_c t + \phi), \tag{1.4}$$

where $\varepsilon_0(t)$, $\omega_c$ and $\phi$ are the slowly time-varying electric field, the carrier frequency and the carrier phase. The envelope of the electric field $\varepsilon_0(t)$ can take arbitrary forms, but in cases of pulses from a Ti:sapphire femtosecond laser, we assume gaussian shaped pulses ($e^{\frac{-4t^2 \ln 2}{\tau^2}}$).

A Fourier transform decomposes the time-dependent waveform in a complex spectral intensity $\tilde{E}(\omega)$, which is given by

$$\tilde{E}(\omega) = \int_{-\infty}^{\infty} \varepsilon(t) e^{-i\omega t} dt, \tag{1.5}$$

where $|\tilde{E}(\omega)|$ and $\arg(\tilde{E}(\omega))$ are the spectral amplitude and phase, respectively. The inverse Fourier transform reads

$$\varepsilon(t) = \frac{1}{2\pi} \int_{-\infty}^{\infty} \tilde{E}(\omega) e^{i\omega t} d\omega. \tag{1.6}$$

Hence, time and frequency are coupled in a fashion that a so-called "transform limited" pulse has the minimum possible pulse duration $\Delta\tau$ for a given spectral bandwidth $\Delta\nu$. The bandwidth limited product for a gaussian pulse reads

$$\Delta\nu\Delta\tau \approx 0.441, \tag{1.7}$$

and equals 0.315 for a *sech*$^2$ pulse[10]. Therefore, tailoring the temporal shape of short pulses can be performed both in time as well as in frequency space.

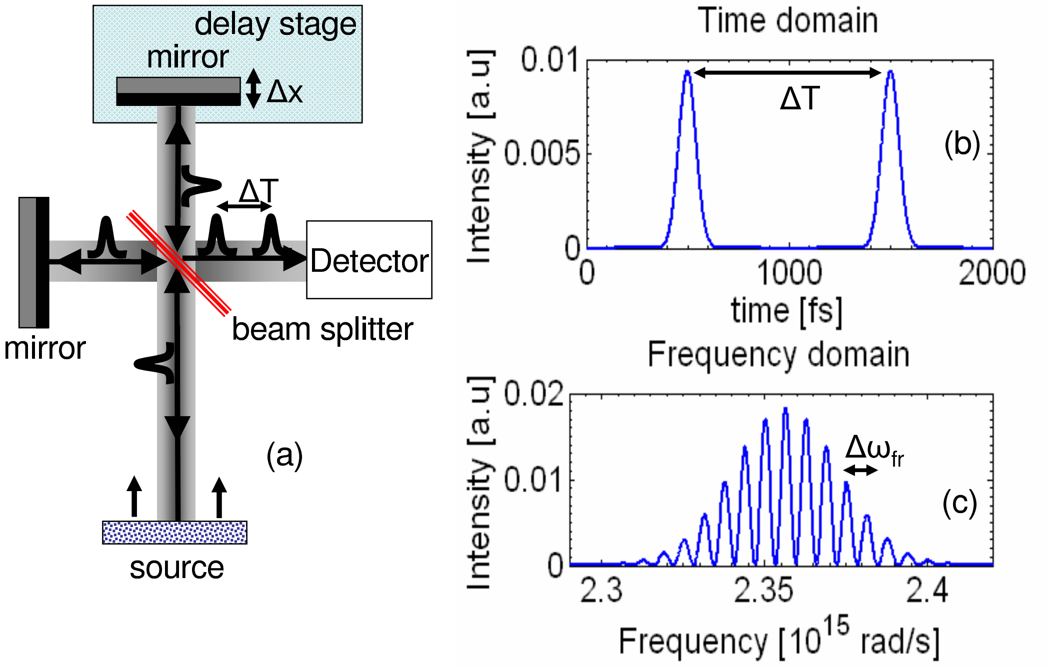

**Figure 1.7:** (a) Michelson-interferometer. (b) Two-pulse sequence from the interferometer with time delay $\Delta T$ equal to $\frac{2\Delta x}{c}$. (c) Frequency distribution of the two-pulse sequence.

### 1.5.1 Time domain pulse shaping

In the time domain, pulse shaping approaches are based on linear filtering schemes, characterized by a time response function $g(t)$. Electric signals ranging from low radio frequencies to very high microwave frequencies are time-dependently modulated using common electrical engineering concepts of resistors, capacitors, and inductors. Their applications are found for instance in nuclear magnetic resonance (NMR)[5].

However, the electronic hardware for filtering in the optical domain is intrinsically too slow, $\ll 1$ THz. Therefore, amplitude splitting devices, such as the Mach-Zehnder and Michelson-interferometer (Fig. 1.7(a)) are used. These devices can produce pulse trains with variable delay times and polarization[2], simply by introducing an extra path length or a wave plate in one arm of the interferometer. In Chapter 3, we use the Michelson-interferometer to create a two-pulse sequence. The Fourier transform of the two-pulses, using Eq.(1.5), shows in Fig. 1.7(c) a frequency distribution with a fringe pattern. The spacing between two maxima $\Delta\omega_{fr}$ is inverse proportional to the time delay, $\Delta\omega_{fr} = \frac{2\pi}{\Delta T}$. Frequencies are present and frequencies are absent. Such a modulation of the amplitude spectrum has a profound influence on atomic and molecular excitation processes and can be used to coherently control the light-matter interaction.

### 1.5.2 Frequency domain pulse shaping

A creative solution to the problem of slow modulators is indirect pulse shaping in the frequency domain. The most common case of a spectral modulation is dispersion in a dielectric material (i.e. glass), see Fig. 1.8(a). A frequency-dependent refractive

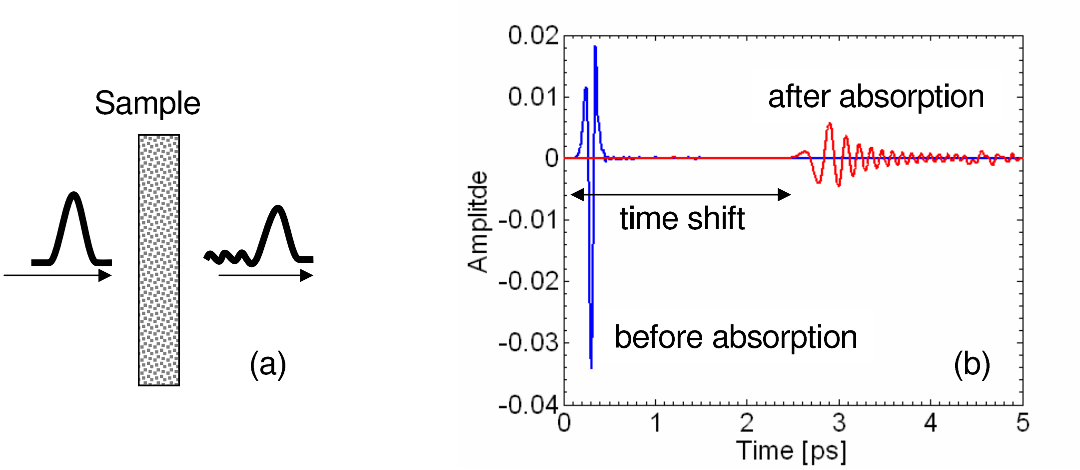

**Figure 1.8:** (a) The propagation of a light pulse through a medium is governed by absorption. The pulse excites atoms in a medium and due to free-induction decay the absorbed energy is coherently re-emitted in the forward direction. The pulse obtains a weak oscillating tail that contains the absorbed frequency, but with a phase shift of $\pi$, such that it interferes destructively with the same frequency component in the main pulse and leads to a frequency spectrum with missing frequencies. (b) Measurement of 5 mm thick CsI sample at 10 K with a terahertz time domain spectrometer (THz-TDS) (see Chapter 5).

index $n(\omega)$ and absorption $\alpha(\omega)$ modulate the frequency distribution of a plane wave as follows

$$\tilde{E}(\omega) = \tilde{E}_0(\omega) e^{-\alpha(\omega)d/2} e^{i(n(\omega)-1)\omega d/c}, \tag{1.8}$$

where $\tilde{E}_0(\omega)$, d and $c$ are the original plane wave, the thickness of the sample and the speed of light. It is of interest to note that different frequency components within a pulse propagate through a medium with different velocities ($v(\omega) = \frac{c}{n(\omega)}$) and therefore disperse in time, called group velocity dispersion (GVD). In Chapter 5, we perform terahertz (THz) transmission measurements to obtain the dielectric properties of CsI in order to calibrate the prism spectrometer. A measurement is shown in Fig. 1.8(b) to illustrate the influence of GVD as an elongated pulse.

A Taylor expansion of the phase $\Phi(\omega) = \frac{\omega n(\omega) d}{c}$ around the central frequency $\omega_0$ provides insight in the consequence of a frequency-dependent phase profile and is written as[10]

$$\Phi(\omega) = \Phi(\omega_0) + \frac{d\Phi(\omega)}{d\omega}(\omega - \omega_0) + \frac{1}{2}\frac{d^2\Phi(\omega)}{d\omega^2}(\omega - \omega_0)^2 + ... \tag{1.9}$$

or

$$\Phi(\omega) = a_0 + a_1(\omega - \omega_0) + \frac{1}{2}a_2(\omega - \omega_0)^2 + ... \tag{1.10}$$

The first term is a constant phase and determines the relative group phase of the pulse. A linear phase change, $a_1 = \frac{d\Phi(\omega)}{d\omega}$, results (after Fourier transform) in a temporal shift of the pulse along the time axis as a group delay. This effect is responsible for the time shift of the absorbed pulse in Fig. 1.8(b) and can be related to the thickness of the medium. The coefficient $a_2 = \frac{d^2\Phi(\omega)}{d\omega^2}$ is the linear chirp ($fs^2$) and is responsible for pulse lengthening, as observed in Fig. 1.8(b). This dispersion, $a_2$, of CsI separates

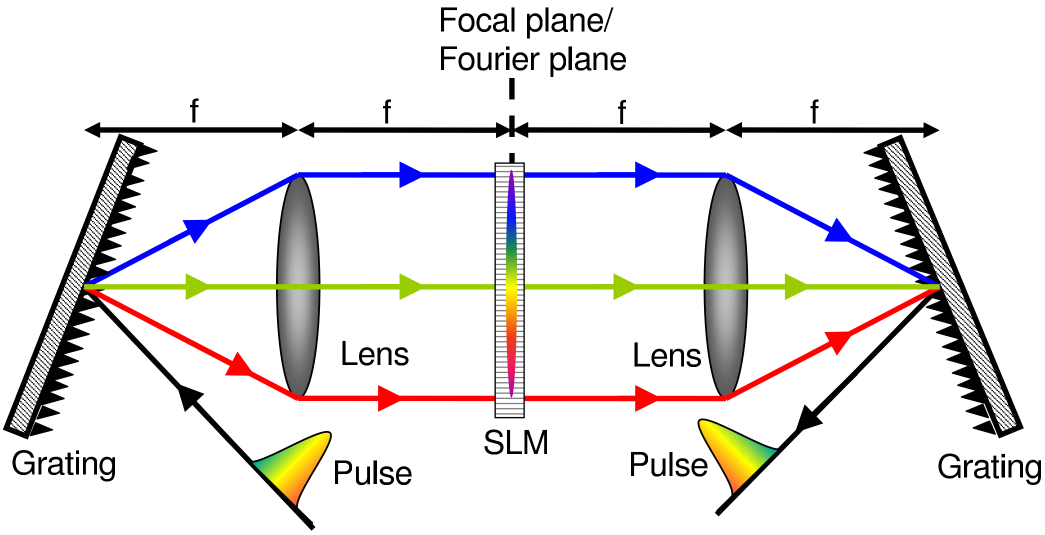

**Figure 1.9:** The pulse shaper is symmetric in the Fourier plane and a mirror can be placed in the Fourier plane to fold the setup. With the ability of the SLM to rotate the polarization $\frac{\pi}{2}$, a simple polarizing beam splitter can separate the incoming from the returning beam.

THz frequencies in a prism and possesses a positive chirp (first red frequencies then blue). Negative chirps (first blue frequencies then red) are observed in other materials. In both cases, the instantaneous frequency drifts in time.

Sometimes one requires dispersion up to higher orders $a_m = \frac{d^m\Phi(\omega)}{d\omega^m}$[38]. The Taylor expansion loses its value for extremely short pulses <5 fs and when the dispersion is highly nonlinear, like close to a resonance in a medium. It is therefore convenient in numerical modeling to directly work with a table of frequency-dependent refractive indices $n(\omega)$ that are represented by the Sellmeier equation. An empirical relationship between refractive index $n$ and wavelength $\lambda$ for a particular transparent medium. The description of the Sellmeier representation is given in Section 5.2.1.

A far more flexible solution to tailor arbitrary waveforms was first suggested by Weiner *et al.*[39] and is shown in Fig. 1.9. In analogue with a spectrometer, a grating separates the spectral components in the pulse and a lens images the frequency distribution as a line in the Fourier plane. All frequency components are again recombined into a short pulse by a second lens and grating pair. In the Fourier plane, the frequencies are equally spaced and available for manipulation. In many cases, a liquid crystal display (LCD) is used as a spatial light modulator (SLM), such as we have used in Chapter 4[40]. This one-dimensional spatial light modulator has typically 320 pixels of 100 $\mu m$ wide (spaced by 3 $\mu m$), which can individually be controlled by applying a voltage across the liquid crystal cells. Two one-dimensional SLMs after each other are able to perform simultaneous amplitude, phase and polarization modulation. Arbitrary waveforms can be synthesized, either complex pulse structures or multiple pulse sequences as produced by interferometers, see Fig. 1.7. The incident spectral distribution $\tilde{E}_{in}(\omega)$ is modulated by the SLM with a response function $\tilde{M}(\omega)$. This results in an outgoing shaped spectral distribution $\tilde{E}_{out}(\omega)$

$$\tilde{E}_{out}(\omega) = \tilde{E}_{in}(\omega)\tilde{M}(\omega), \tag{1.11}$$

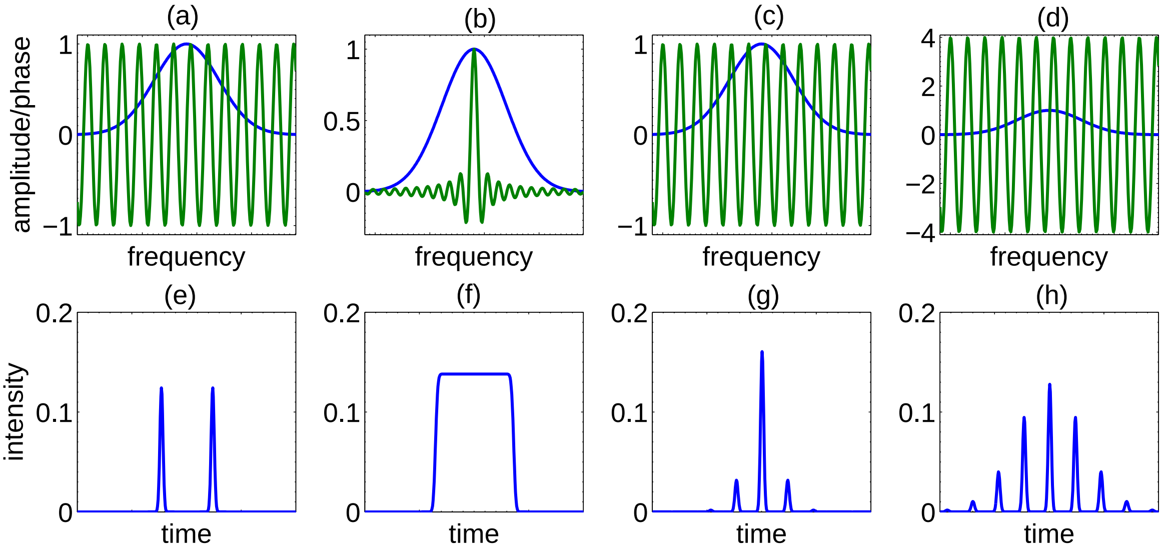

**Figure 1.10:** Spectral amplitude modulation: (a) $\cos(\omega\beta)$, (b) $sinc((\omega-\omega_c)\beta)$. Spectral phase modulation: (c) $\cos(\omega\beta)$ (d) $4\cos(\omega\beta)$. (e)-(h) resulting temporal profiles after amplitude and phase modulations.

with

$$\tilde{E}_{in}(\omega) = \tilde{S}(\omega)e^{-i\varphi}, \tag{1.12}$$

where $S(\omega)$ and $\varphi$ are the spectral amplitude and phase according to Eq. (1.5). Figure 1.10 illustrates the consequence of a periodic amplitude or phase modulations on the temporal pulse structure. In Fig. 1.10(e) a two-pulse sequence is created like in the Michelson-interferometer (Fig. 1.7) by a $\cos(\omega\frac{\Delta T}{2})$ spectral amplitude modulation (Fig. 1.10). This result can be understood as followed: if we write $\cos(\omega\frac{\Delta T}{2})$ as $\frac{1}{2}(\exp(\omega\frac{i\Delta T}{2}) + \exp(-i\omega\frac{\Delta T}{2}))$, the inverse Fourier transform gives two delta pulses, one shifted earlier in time by $\frac{\Delta T}{2}$ and another shifted later in time by $\frac{\Delta T}{2}$. The net result is a double pulse (two copies of the input pulse), which are separated in time by $\Delta T$ and $\varepsilon_{out}(t) = \frac{1}{2}(\varepsilon_{in}(t-\frac{\Delta T}{2}) + \varepsilon_{in}(t+\frac{\Delta T}{2}))$.

A natural question is: how may one design a controlling pulse that after an excitation produces a desired outcome? In simple two- or three-level systems, first- and second-order perturbation theory provides insight in the frequency-dependent behavior of the transition rates and an optimal pulse can be designed intuitively. The time-independent analytical solutions directly show that the quantum interference can be controlled by manipulating the amplitude and phase of the photons. A detailed description of the second-order perturbation for a two-photon process is given in Section 2.2.2.

In large molecules and complex biological systems, adaptive laser pulse shaping techniques are used to design the optimal pulse shape, as illustrated in Fig. 1.11[18,22,41–43]. Coherent control techniques have evolved from focusing solely on chemical systems to a wide range of quantum mechanical systems, and have been applied successfully to semiconductor systems, terahertz radiation sources, shaping of Rydberg wave functions, quantum dots and single atoms[44–48].

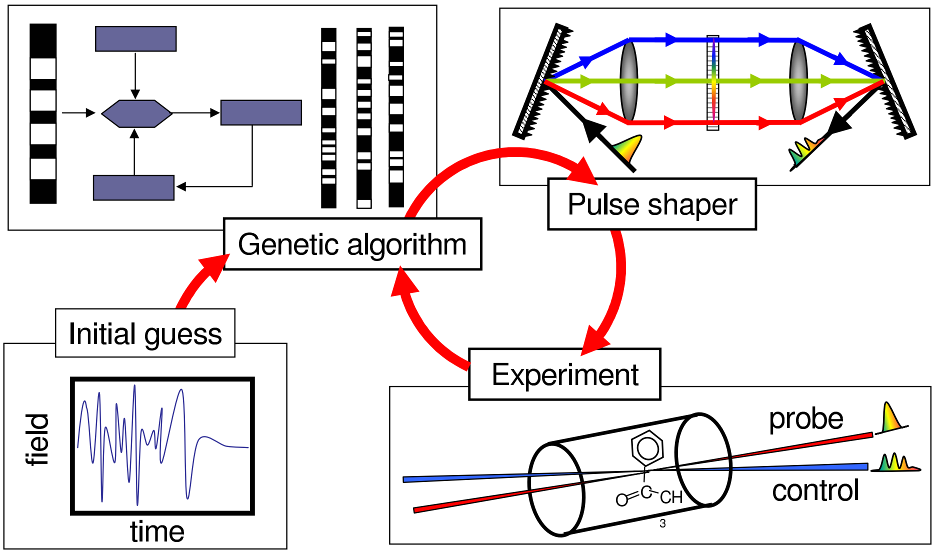

**Figure 1.11:** This so-called "optimal control theory" uses in a close-loop first an initial guess of a laser pulse temporal structure. This pulse structure is programmed in the pulse shaper and is then applied to the sample. The response of the atom or molecule is measured and fed back to an optimization algorithm, which suggests an improved pulse design. Iteratively, the driving optical field is refined to achieve a chosen target objective, i.e. enhancement of a specific reaction product[48].

## 1.6 My thesis

The interaction between electromagnetic radiation and matter dominates the research presented in this thesis. We have studied the quantum mechanical interference in rubidium (Rb) as well as in nitric oxide (NO) for the fundamental understanding of excitation processes in multilevel systems. We employ "physics-inspired" tailoring mechanisms, like absorption in a gas and diffraction on obstacles to reshape the temporal structure of femtosecond and terahertz pulses. Additionally, for each experiment computational studies are carried out to verify the measurements and to give insight into the quantum mechanical aspects. A summary of the conducted studies and their aims are given below. In the four presented studies, measurements are carried out each time on different setups. Each setup is therefore described in the chapters itself.

**Chapter 3** In the pursuit of experimental control over molecular quantum state preparation, optical excitation provides an alternative means. Therefore, we investigate the process of femtosecond stimulated Raman (FSR) in molecular NO as a tool to selectively excite rotational levels. Within the bandwidth of the femtosecond pulse, each pair of photons with a difference frequency $\omega_p - \omega_s$ equal to a rotational transition frequency $\omega_{J,J'}$ are able to excite a rotational state in NO. A two-pulse sequence with a fringe pattern in the frequency distribution (Fig. 1.7(c)) is used to coherently control the state population. From our results, we can conclude that one can selectively discriminate between two quantum mechanical pathways climbing the rotational ladder in NO, by choosing a particular time delay $\Delta T$ between the two femtosecond pulses. We measure quantum interferences with time delays up to 20 ps. The process of FSR is a versatile tool to selectively excite dense samples of rotationally excited molecules.

**Chapter 4** The use of femtosecond pulses implies a wide range of frequencies, which all participate in the excitation process. This results in a loss of spectral selectivity, since all the transitions within the bandwidth may be excited. Therefore, we investigate the process of narrow band absorption as a tool for tailoring femtosecond pulses in order to selectively enhance or deplete excited state population in a multilevel system. We perform our measurements in the three-level system of rubidium (5s-5p-5d) and probe the two-photon absorption signal. The linear combination of a frequency-dependent phase and amplitude, according to the Kramers-Kronig dispersion relation, is programmed in the spatial light modulator of a pulse shaper to simulate absorption. Three sets of measurements are recorded; only-phase, only-amplitude and, both combined called absorption. Semi-monochromatic transient electric fields appear around the main pulse and reshaped pulses by absorption have only a post-transient, due to causality. We conclude that these semi-monochromatic transients are ideal sources of radiation to populate and deplete selective states. In the strong field, a theoretical optimal pulse is designed, which holds the ability for complete inversion, due to Rabi-cycling of the state population.

**Chapter 5** We generate coherent radiation with a nearly "white light" spectrum in the far-infrared regime. We realized that the large frequency spread in the far-infrared range is one of the causes as to why a simple spectrometer has not been developed. Therefore, a terahertz CsI prism spectrometer is designed and tested. Radiation from a large biased semi-conductor, illuminated with femtosecond pulses, is collimated and dispersed by a cryogenically cooled 25 K CsI prism mounted in a cryostat. Transmission THz-TDS measurements have been used to obtain the temperature-dependent dielectric function of CsI as well as of KBr and KCl. The obtained refractive indices are fitted accurately using a two-term Sellmeier representation. The spectrum from a THz emitter is obtained and the transmission spectra of 300 and 600 GHz frequency selective surface filters. We find that the CsI prism spectrometer is transparent from 0.2 to 1.1 THz with an overall energy throughput better than 10%. The resolving power is about 35 GHz near 1 THz reducing to 173 GHz at 300 GHz. This spectrometer can be used as a fast monitor for time-depended studies in large molecules, organic and biological samples.

**Chapter 6** Infrared (IR) cameras are widely used to monitor temperature differences between objects and record infrared sources, such as stars. Therefore, a prototype far-infrared camera is developed based on ionization of gas-phase Rydberg atoms. The photocathode of highly excited rubidium atoms as photo-detectors operates from 1 - 1000 $\mu m$ and has an exposure time of 10 ns, which removes the need for cryogenic cooling. In a overview, we present a theoretical background of the far-infrared camera. We discuss the designed open electrostatic optics, the Rydberg atoms, and the one-photon photo-ionization and -excitation cross sections. Calculating the detection efficiency shows that the camera becomes more sensitive towards lower frequencies. Only tens of nanoJoules of far-infrared radiation is needed to create an image. We have tested the imaging properties, the spatial resolution and distortion with 1064 nm light from a YAG laser. These measurements illustrate that the Rydberg camera is capable of capturing real two-dimensional images.

**Chapter 7** The basics of a camera is to distinguish the shadow cast by an object whenever an obstacle is placed midway between a far-infrared source and the photocathode. We use the Rydberg camera in combination with broadband coherent terahertz (THz) radiation from a large biased semi-conductor, illuminated with femtosecond pulses. The emitted THz pulses are in the form of half a cycle with a high nonlinear ionization behavior on Rydberg atoms. We characterize the performance of the Rydberg camera for THz pulses by measuring the intensity-dependence, the spatial resolution, and using lenses. Simple obstacles are placed in the freely propagating THz beam. However, diffraction greatly affects the half-cycle pulse structure and also the ionization probability of Ryberg atoms. Therefore, we verified the Rydberg camera measurements with a linear bolometer detector, which measures the energy of the radiation, irrespective of the THz pulse shape. Model calculations solving the diffraction integrals provide the spatiotemporal distribution of THz beam. We find a strong correlation between the presence of multiple oscillations in the simulations and suppression of Rydberg ionization in the photocathode of the Rydberg camera. We can conclude that broadband THz radiation is not a good far-infrared source for the Rydberg camera. The nonlinear spatial ionization of THz half-cycle pulses makes the interpretation of the obtained images with the Rydberg camera difficult.

# CHAPTER 2

## Short pulse photoexcitation in a multilevel system

The light-matter interaction discussed in this thesis emphasizes nonlinear photoexcitation of short optical and far-infrared pulses in the multilevel system of rubidium. Several pictures can be used to describe the coherent excitation processes:

(1) Semiclassically as a momentum 'kick' to the electron in its orbit around the core. We use this 'planetary' model to simulate the ionization behavior of highly excited Rydberg atoms by terahertz (THz) half- and full-cycle pulses. As the coherent contribution of many low energetic photons in the far-infrared THz pulse ionizes the Rydberg atoms through almost an infinite number of discrete intermediate levels, full quantum mechanical calculations are impractical.

(2) Quantum mechanically as a time-dependent perturbation of the electron cloud. The electric field of a light pulse creates a superposition of coherent states, which may be populated (pump) or depleted (dump), depending on the 'shape' of the temporal pulse structure. We use the time-dependent Schrödinger equation to calculate the outcome of a stimulated absorption process in the first three levels of ground state rubidium with reshaped pulses by narrow band absorption.

(3) Quantum mechanically as a time-independent perturbation by many photons, all participating simultaneously in an excitation process. We use the second-order perturbation theory to provide an intuitive insight in the coherent two-photon absorption process in the first three levels of ground state rubidium. In this photon-picture, the amplitude and phases of the photons are of importance and can be used as 'control knobs' to steer the outcome of a light-matter interaction. The same picture can used to predict the outcome of the stimulated Raman process in molecular nitric oxide ($\mathrm{NO}$).

A.S. Meijer

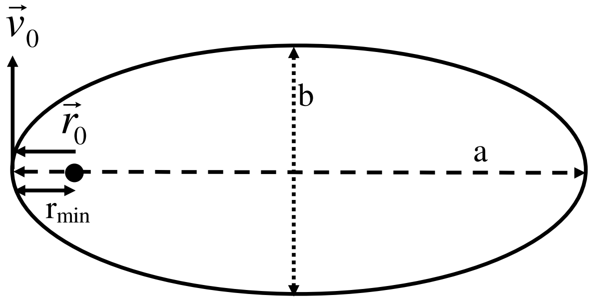

**Figure 2.1:** Elliptical orbit (of the electron) around a focal point (the nucleus) with quantized semi-major axis $a = n^2$ (n is principle quantum number) and semi-minor axis $b = nl$ ($l = \frac{1}{2}...\frac{1}{2} - n$) (l is angular quantum number)

## 2.1 The semiclassical model of Rydberg atoms

In the semiclassical atomic model of Bohr and Sommerfeld, the electron moves in a $-\frac{1}{r}$ Coulomb potential along elliptical orbits around the core, like the earth around the sun. However, quantum mechanics abandoned this idea that a physical path could be ascribed to the electron, but the Ehrenfest principle demands that when expectation values are taken, the quantum mechanical observables obey the classical equation of motion. Therefore, the classical laws of Kepler planetary motion are enriched with the quantization of the orbits and angular momentum. The resulting model (Bohr-Sommerfeld) is in excellent agreement with experimental results on Rydberg atoms and provide an intuitive insight into the physics. However, note that this semiclassical model has its limitations and difficulties when interpreting quantum mechanical phenomenons.

### 2.1.1 The equation of motion of a Rydberg atom

The equation of motion in the classical atomic model, an electron in the Coulomb potential of the atomic core, is given by the Kepler equation[49] (note that atomic units are used unless stated otherwise)

$$\ddot{\vec{r}} = -\frac{1}{r^3}\vec{r}, \tag{2.1}$$

where the centrifugal force, $|\vec{F_c}| \propto 1/r^2$, is always directed towards the nucleus, located in the focal point of the ellipse, as depicted in Fig. 2.1. The classical motion of the Rydberg electron is uniquely determined by the solution of Eq. (2.1) with initial conditions derived from quantum mechanics. A stationary Rydberg state is described by the quantum numbers $n$, $l$, $m$, representing the state's energy, the angular momentum and its projection on the quantization axis. The major axis of the ellipse $a$ is determined by the state energy $E_n = -\frac{1}{2n^2}$ (Rydberg formula). The minor axis is determined by the angular momentum (Sommerfeld quantization condition). As a result

$$a = n^2, \tag{2.2}$$

$$b = nl, \qquad l = \tfrac{1}{2}....n - \tfrac{1}{2}. \tag{2.3}$$

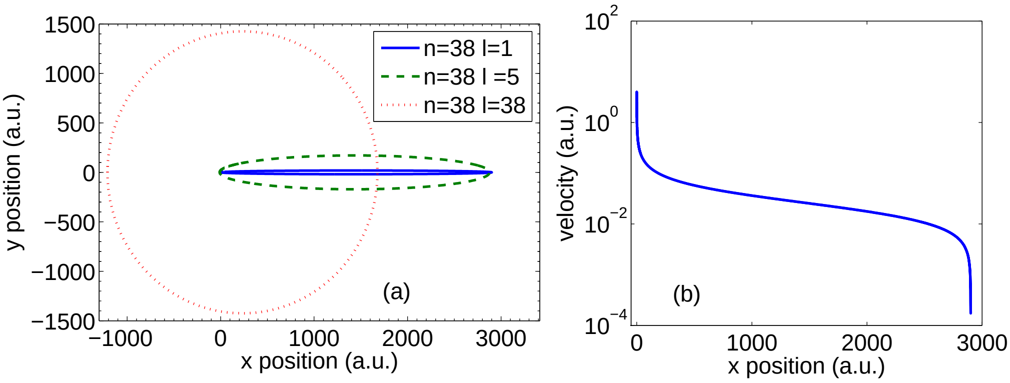

**Figure 2.2:** (a) Classical orbits of n=38 with l=1, l=5 and l=38 states. (b) The absolute velocity distribution of the Rydberg electron in a n=38, l=2 state.

To solve the equation of motion the second-order differential equation is rewritten in a pair of first-order equations:

$$\begin{aligned} \frac{dx}{dt} &= v_x, \quad \tfrac{dv_x}{dt} = -\tfrac{1}{r^3}x, \\ \frac{dy}{dt} &= v_y, \quad \tfrac{dv_y}{dt} = -\tfrac{1}{r^3}y, \end{aligned} \tag{2.4}$$

where the vectorial representation of position and velocity are completely determined by their x- and y-components: $\vec{r} = (x, y)$ and $\vec{v} = (v_x, v_y)$. The trajectory starts at $\vec{r}_0$ at the inner turning point with velocity $\vec{v}_0$. These initial conditions are given by

$$r_0 = r_{min} = a - \sqrt{a^2 - b^2}, \tag{2.5}$$

$$v_0 = \sqrt{2\left(-\frac{1}{2n^2} + \frac{1}{r_{min}}\right)}. \tag{2.6}$$

The ordinary differential equations in Eq. (2.4) are numerically integrated using the $4^{th}$-order Runga-Kutta method with adaptive stepsize to get accurate closure of the orbits and good energy conservation, since the velocity of the electron can easily vary by four orders of magnitude on different parts of its orbit, as depicted in Fig. 2.2(a). Figure 2.2(b) shows classical orbits for several n=38 states. As can be seen, low $l$-states have long-drawn elliptical orbits and spend most of the time at large $r$, as the velocity far away from the core is very low (Fig. 2.2(a)). High $l$-states have more circular orbits and do not come near the nucleus. Therefore, high $l$-states are insensitive to the exact configuration of the core. For instance, rubidium has 37 electrons around the nucleus and the Coulomb potential of the outer electron deviates from $-\frac{1}{r}$ (see Section 6.3).

Some well known scaling laws for Rydberg atoms can be derived from this classical model and are given in table 2.1. The Rydberg orbital time $\tau_K = 2\pi n^3$ follows directly from Kepler's Third Law, $\tau_K^2/a^3 = const.$ These scaling laws provide an intuitive insight in the behavior of Rydberg atoms with external electric fields, like light. A detailed description of the atomic configuration of rubidium and the Rydberg series is given in Section 6.3.

**Table 2.1:** Classical scaling laws for Rydberg electrons.

| Property | n-dependence | Rydberg state: n = 38 |
|---|---|---|
| Binding energy | $n^{-2}$ | 9.4 meV |
| Orbital radius | $n^2$ | 0.076 $\mu m$ |
| $\tau_K$ | $n^3$ | 8.3 ps |
| Radiative lifetime | $n^3$ | 64 $\mu s$ |
| Energy spacing | $n^{-3}$ | 0.50 meV |
| Field ionization | $n^{-4}$ | 120 V/cm |

### 2.1.2 Short pulse photoionization of Rydberg atoms

Photoexcitation of Rydberg atoms with narrow band radiation is a linear interaction of one photon being absorbed or a multi-cycle electric field perturbing the system. However, in Chapter 7, we use ultrashort ($\approx 500fs$) terahertz pulses in the form of half a cycle (HCP) with a nearly 'white light' spectrum in the far-infrared regime, ranging from 100 GHz - 3 THz (3 mm - 300$\mu m$)[13–17]. Such an HCP has a strong nonlinear interaction[50–53] with highly excited Rydberg atoms and their ionization behavior can be described as a multiphoton process or as a momentum 'kick' to the Rydberg electron. For a detail description see section 7.3.1.

We investigate in Chapter 7 the spatial disturbance of the THz beam when obstacles are placed midway between the THz emitter and the Rydberg photocathode. Propagation effects, optical elements and diffraction greatly affects the HCP spectral distribution[54–57] and thus the HCP temporal profile. Both low and high frequency components are diffracted from the beam and the HCP evolves via a single full-cycle pulse (FCP) into a multi-cycle pulse. For instance, in a freely propagating THz beam, high frequency components remain in the center, while low frequency components are concentrated on the outside. On the outside of the beam, the HCP evolves via a single full-cycle pulse (FCP) into a multi-cycle pulse. Recently, Bitzer et al.[56] have experimentally detected full-cycle pulses in the focal point of a lens, due to reshaping of the THz pulse, which was predicted by You *et al.*[54].

The half- and full-cycle THz electric fields $\vec{\varepsilon}_{THz}(t)$ are implemented in the classical equation of motion Eq. (2.1) of the electron in a Coulomb potential. The equations read

$$\vec{\ddot{r}} = -\tfrac{\vec{r}}{r^3} + \vec{\varepsilon}_{THz}(t - t_{THz}), \tag{2.7}$$

$$\vec{\varepsilon}_{HCP}(t) = \vec{\varepsilon_0} e^{\frac{-4t^2 \ln 2}{\tau^2}}, \qquad \vec{\varepsilon}_{FCP}(t) = -\vec{\varepsilon_0} \frac{4t \ln 2}{\tau^2} e^{\frac{-4t^2 \ln 2}{\tau^2}}, \tag{2.8}$$

where the THz pulse with a FWHM ($\tau$) arrives at time $t_{THz}$. Integration delivers $\vec{r}$ and $\vec{v}$ after the THz pulse, which determine the final binding energy, $E_n = -\frac{1}{r} + \frac{1}{2}v^2$. A positive $E_n$ implies ionization. This final binding energy depends on $t_{THz}$ with respect to the position of the electron in its orbit around the nucleus. The ionization probability is determined by the number of times that the binding energy is positive. This method has shown to agree well with fully quantum mechanical calculations and predicts experimental data on HCP ionization of Rydberg atoms correctly[53,58,59].

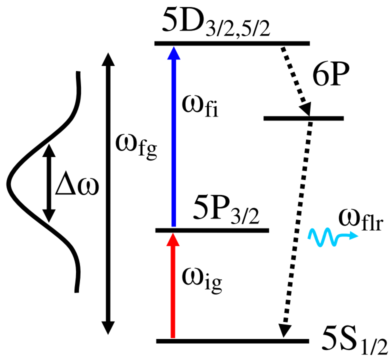

**Figure 2.3:** The three-level system in rubidium with transition frequencies $\omega_{i,g}$ and $\omega_{f,i}$. All photons pairs $\tilde{E}(\omega)+\tilde{E}(\omega_{fg}-\omega)$ within the bandwidth of the femtosecond pulse, resonant as well as nonresonant with the intermediate state, will contribute to the final state population $|\psi_f|^2$.

Classical calculations provide information in a fast and intuitive manner on the ionization probability of the Rydberg wavefunction for different temporal pulse structures.

## 2.2 Quantum mechanical model of a three-level system

In this paragraph, we set up the quantum mechanical model for the first three energetic states of rubidium, as depicted in Fig. 2.3. The ground $\psi_g$, intermediate $\psi_i$ and final $\psi_f$ state correspond to the 5s-5p-5d ladder where $\lambda_{i,g} = 780.2$ nm and $\lambda_{f,i} = 776.2$ nm are the transition wavelengths with transition dipole moments $\mu_{ig} = 5.87$ atomic units (a.u.) and $\mu_{fi} = 1.77$ a.u[60]. The dynamics of this atomic system can be described by the time-dependent Schrödinger equation[4],

$$i\hbar\frac{\partial}{\partial t}|\Psi(t)\rangle = \hat{H}(t)|\Psi(t)\rangle, \tag{2.9}$$

where $\Psi(t)$ and $\hat{H}(t)$ are the time-dependent wave function, describing the behavior of the atom and the Hamiltonian, which contains the properties of the atom as well as the time-dependent electric field of light. The eigenenergies $E_g$, $E_i$ and $E_f$ are eigenvalues of the atom Hamiltonian $\hat{H}_{atom}$. Note that $E_g < E_i < E_f$ and the energy difference $E_n - E_m$ are related to the transition frequencies, $\omega_{n,m} = (E_n - E_m)/\hbar$.

In the absence of the light electric field, the Hamiltonian $\hat{H}$ is solely determined by the atom and is time-independent. The solution for the atomic system is given by

$$|\Psi(t)\rangle = \sum_{n=g,i,f} C_n(t=0)\exp(-i\frac{E_n}{\hbar})|\psi_n\rangle, \tag{2.10}$$

in which $C_n(t = 0)$ are prescribed by the initial conditions. Equation (2.10) shows that the coefficients before the eigenstates $|\psi_n(t)\rangle$ have similarities with a plane wave and only accumulate an overall complex phase factor with no observable consequences.

Equation (2.10) is one of the motivations, why scientist are interested in finding the accurately energy eigenstates.

### 2.2.1 Time-dependent

If we switch on a laser, the dynamical effects of a time-dependent electromagnetic laser field $\varepsilon(t)$ on the three system states $|\psi_g\rangle$, $|\psi_i\rangle$ and $|\psi_f\rangle$ is introduced by the interaction Hamiltonian $\hat{H}_{laser}(t)$. In the absence of spontaneous emission, the total Hamiltonian $\hat{H}(t)$ reads

$$\hat{H}(t) = \hat{H}_{atom} + \hat{H}_{laser}(t). \tag{2.11}$$

The presence of the interacting light field moves population between the three states. This can be accommodated by making the coefficients $C_n(t=0)$ explicitly time-dependent: $C_g(t)$, $C_i(t)$ and $C_f(t)$. The choice of the phase factors separates the fast oscillations from the slower population changes. For instance, in the experiment of Chapter 4, a femtosecond pulse is used of which the carrier frequency $\omega_c$ is close to the transition frequencies $\omega_{i,g}$ and $\omega_{f,i}$. The wavefunction of the atom in Eq. (2.10) is expressible as a superposition of the eigenstates that we write as

$$\begin{aligned} |\Psi(t)\rangle &= C_g(t)e^{-iE_gt/\hbar}|\psi\rangle \\ &\quad + C_i(t)e^{-i(\frac{E_g}{\hbar}+\omega_c)t}|\psi_i\rangle + C_f(t)e^{-i(\frac{E_g}{\hbar}+2\omega_c)t}|\psi_f\rangle. \end{aligned} \tag{2.12}$$

All time dependence is contained within the time-varying coefficients $C_n(t)$ and evolves with an exponentiated phase. The quantities of interest are the time-dependent probabilities $P_n(t) = |C_n(t)|^2$ of finding the system in state $\psi_n$ at time t. We assume the ground state to be populated before the light hits the atoms: $C_g(0) = 1, C_i(0) = C_f(0) = 0$. Substitution of the expansion into the Schrödinger equation (Eq. (2.9)) produces a set of coupled ordinary differential equations for the probability amplitudes which is given by:

$$\begin{aligned} i\hbar\frac{d}{dt}C_g(t) &= C_i(t)e^{-i\omega_ct}M_{12}(t), \\ i\hbar\frac{d}{dt}C_i(t) &= C_g(t)e^{-i\omega_ct}M_{21}(t) + C_i(t)\Delta_{i,g} + C_f(t)e^{-i2\omega_ct}M_{23}, \\ i\hbar\frac{d}{dt}C_f(t) &= C_i(t)e^{-i2\omega_ct}M_{32}(t) + C_f(t)\Delta_{f,g}, \end{aligned} \tag{2.13}$$

where $\Delta_{i,g} = |\omega_{i,g} - \omega_c|$ is the detuning of the carrier frequency from the first resonance. $\Delta_{f,g} = |\omega_{f,g} - 2\omega_c|$ is the detuning of the carrier frequency from the two-photon resonance. The transition matrix element $M_{n,m}$ are given by

$$\hbar M_{n,m} = \int \psi_m^* \hat{H}_{laser}\psi_n dV = \langle\psi_m|\hat{H}_{laser}|\psi_n\rangle, \tag{2.14}$$

with $M_{11}$=$M_{22}$=0 as one can see from symmetry and

$$\hat{H}_{laser} = \varepsilon(t) = e\vec{D}\varepsilon_0(t)cos(\omega_ct), \tag{2.15}$$

where $\varepsilon_0(t)$ is the temporal envelope of the electric field ($\varepsilon_0 = e^{\frac{-4t^2\ln 2}{\tau^2}}$) and $e\vec{D}$ the transition dipole operator $\mu_{n,m}$ along the electric field direction. This is in analogy to the classical expression for the energy of a single electron moving in an electromagnetic field. A solution for the transition matrix element $M_{n,m}$ then reads

$$M_{n,m} = \frac{\varepsilon_0(t)\mu_{n,m}}{\hbar} cos(\omega_c t). \tag{2.16}$$

The time-dependent term $\cos(\omega_c t)$ can be rewritten as $\cos(\omega_c t) = \frac{1}{2}(e^{i\omega_c t}+e^{-i\omega_c t})$. The fast oscillating terms are neglected in the rotating-wave approximation (RWA) and the evolution of the system will be governed by the slow varying $\varepsilon_0(t)$. Substitution of the transition matrix elements (Eq. (2.14)) into Eq. (2.13) give rise to

$$\begin{aligned} i\hbar\frac{d}{dt}C_g(t) &= \Omega_{i,g}C_i(t), \\ i\hbar\frac{d}{dt}C_i(t) &= \Omega_{g,i}(t)C_g(t) + \Delta_{i,g}C_i(t) + \Omega_{f,i}(t)C_f(t), \\ i\hbar\frac{d}{dt}C_f(t) &= \Omega_{i,f}(t)C_i(t) + \Delta_{f,i}C_i(t). \end{aligned} \tag{2.17}$$

$\Omega_{n,m}$ is the Rabi frequency, which represents the strength of the light-matter coupling and hence the exchange of energy between light and matter.

$$\Omega_{n,m}(t) \equiv \frac{\varepsilon_0(t)\mu_{n,m}}{2\hbar}. \tag{2.18}$$

Without any restrictions, one can always consider the Rabi frequency as real. The reason is that any possible phase factor $e^{i\phi}$ can be compensated by adding an overall phase factor to the state $|\psi_n\rangle$, since global phase factors have no physical effect. The differential equations may also be written in matrix form as

$$i\hbar \begin{pmatrix} \dot{C}_g(t) \\ \dot{C}_i(t) \\ \dot{C}_f(t) \end{pmatrix} = \begin{pmatrix} 0 & \Omega_{i,g}(t) & 0 \\ \Omega_{g,i}(t) & \Delta_{i,g} & \Omega_{f,i}(t) \\ 0 & \Omega_{i,f}(t) & \Delta_{f,i} \end{pmatrix} \begin{pmatrix} C_g(t) \\ C_i(t) \\ C_f(t) \end{pmatrix}. \tag{2.19}$$

The time-evolution of the atomic system $|C_n(t)|^2$ can be examined on a femto- to picosecond time scale and carries the signature of the excitation process. In this way, we obtain insight in the linear and nonlinear excitation process of the spectrally broad band femtosecond pulse.

The coupled differential equations in Eq. (2.17) can numerically be solved using the $4^{th}$-order Runge-Kutta method or matrix manipulation with initial conditions on the state amplitudes (Eq. (2.12)). We observe the time-dependent state population $P \equiv |C_n(\infty)|^2$ that the pulse has produced when completed. The weak field limit is defined as $\Omega_{i,g} = 10^8$ rad/s and the strong field regime as $|\Omega_{i,g}| \gg |\Delta_{i,g}|$ ($\approx 10^{12}$ rad/s).

### 2.2.2 Second-order perturbation theory

In this paragraph, we formulate an analytical expression for the two-photon absorption (TPA) in the multilevel system of rubidium (see Fig. 2.3) for short pulses using the time-independent second-order perturbation theory[4]. The idea is to start with the unperturbed atom and gradually turn on an electric field (light), which "perturbs" the (matter) Hamiltonian $H_{atom}$. In case of a weak perturbation, the various physical quantities associated with the system (e.g. its energy levels and eigenstates) do not change during the excitation process. We will find a time-independent expression by rewriting the time-dependent electric field $\varepsilon(t)$ as a distribution of photon energies by employing a Fourier transform. This provides insight in the coherent TPA process where quantum interference plays an important role. The effect of changing the amplitude and phases of the photons become directly apparent. Only what happens during the pulse remains elusive.

Using perturbation theory still requires solving the time-dependent Schrödinger equation Eq. (2.9). As described in the previous paragraph, in the absence of the light field time $t = 0$, the multilevel system is initially in a single state, the ground state, where $C_g(0) = 1$ and $C_n(0) = 0$. Using the expansion of the wavefunction $|\Psi\rangle$ in Eq. (2.10), a weak perturbation on the transition frequencies $\omega_{n,m}$ implies that

$$\begin{aligned} &\int_{-\infty}^{\infty} dt \sum_n |\langle\psi_f|\mu_{f,n}|\psi_n\rangle\langle\psi_n|\mu_{n,g}|\psi_g\rangle \\ &\times\varepsilon(t_1)\exp(i\omega_{f,n})\varepsilon(t_2)\exp(i\omega_{n,g})| \ll 1, \end{aligned} \tag{2.20}$$

where $\mu_{n,g}$ and $\mu_{f,n}$ are the dipole matrix elements. Under these circumstances, the second-order perturbation approximates that the amplitude of the final state $C_f(t)$ are given by[18,61]

$$\begin{aligned} C_f^{(2)}(t) &= -\left(\frac{1}{\hbar^2}\right)\sum_i \mu_{f,n}\mu_{n,g}\int_{-\infty}^{t}\int_{\infty}^{t_1}\varepsilon(t_1)\varepsilon(t_2) \\ &\quad\times\exp(i\omega_{f,n}t_2)\exp(i\omega_{n,g}t_1)dt_2dt_1. \end{aligned} \tag{2.21}$$

### Resonant two-photon absorption in a three-level system

The summation in Eq. (2.21) is performed over all possible intermediate states of the unperturbed atom. In this paragraph, the system is reduced to the three-level system, as depicted in Fig. 2.3. Again, decoherence processes are ignored. It is instructive to examine first the integration over the intermediate state $|\psi_i\rangle$. Rewriting Eq. (2.21) and substituting $t_2 = t_1 + \alpha$, we arrive at

$$\begin{aligned} C_f^{(2)}(t) &= -\left(\frac{1}{\hbar^2}\right)\sum_i \mu_{f,i}\mu_{i,g}\int_{-\infty}^{t}\varepsilon(t_1)\exp(i\omega_{f,g}t_1) \\ &\quad\times\int_{-\infty}^{0}\varepsilon(t_1+\alpha)\exp(i\omega_{i,g}\alpha)d\alpha dt_1. \end{aligned} \tag{2.22}$$

First, we introduce the Fourier transform integral

$$\varepsilon(t+\alpha) = \int_{-\infty}^{\infty}\tilde{E}(\omega)\exp(-i\omega(t+\alpha))d\omega. \tag{2.23}$$

Integration over $\alpha$ gives

$$\begin{aligned} C_f^{(2)}(t) &= -\left(\frac{1}{\hbar^2}\right)\sum_i \mu_{f,i}\mu_{i,g}\int_{-\infty}^{\infty}d\omega\tilde{E}(\omega)\frac{1}{i(\omega_{i,g}-\omega)} \\ &\quad\times\int_{-\infty}^{t}dt_1\varepsilon(t_1)\exp(i(\omega_{f,g}-\omega)t_1). \end{aligned} \tag{2.24}$$

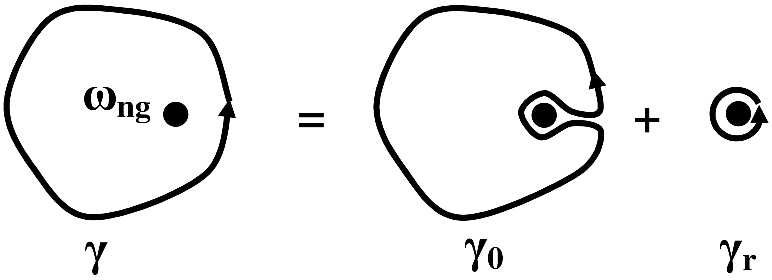

**Figure 2.4:** Contour to evaluate integral in Eq. (2.27) with a singularity $\omega_{n,g}$ and the path $\gamma = \gamma_0 + \gamma_r$.

Note that $\tilde{E}(\omega) = \tilde{A}(\omega)e^{i\theta(\omega)}$, where $\tilde{A}(\omega)$ and $\theta(\omega)$ are the spectral amplitude and phase, respectively. Next, we also Fourier transform $\varepsilon(t_1)$ which yields

$$\begin{aligned} C_f^{(2)}(t) &= -\left(\frac{1}{\hbar^2}\right)\sum_i \mu_{f,i}\mu_{i,g}\int_{-\infty}^{\infty} d\omega \tilde{E}(\omega)\frac{1}{i(\omega_{i,g}-\omega)} \\ &\times \int_{-\infty}^{t} dt_1 \tilde{E}(\omega^{'})\exp(i(\omega_{f,g}-\omega-\omega^{'})t_1). \end{aligned} \tag{2.25}$$

Our interest is observing or controlling the final state product $|C_f(t)|^2$. Then, we only require the wavefunction $|\Psi(t)\rangle$ to approach $t \rightarrow +\infty$. In this limit, we can insert the equality[18]

$$\int_{-\infty}^{\infty} dt_1 \exp(i(\omega_{f,g}-\omega-\omega^{'})t_1) = 2\pi\delta(\omega_{f,g}-\omega-\omega^{'}), \tag{2.26}$$

and the integration is performed explicitly, which yields

$$C_f^{(2)} = -\left(\frac{2\pi}{i\hbar^2}\right)\mu_{f,i}\mu_{i,g}\int_{-\infty}^{\infty}\frac{\tilde{E}(\omega)\tilde{E}(\omega_{f,g}-\omega)}{(\omega_{i,g}-\omega)}d\omega. \tag{2.27}$$

We can show, using contour integration, that the evaluation of this integral in Eq. (2.27) with a singularity is possible. To do so, we use the Cauchy integral theorem, as shown in Fig. 2.4. A path ($\gamma_r$) is defined as an infinitesimal counterclockwise circle around the singularity $\omega_{i,g}$. Also, we define a path ($\gamma_0$) as an arbitrary loop with a cut line (on which the forward and reverse contributions cancel each other out) excludes the singularity $\omega_{i,g}$. The total path is then $\gamma = \gamma_0 + \gamma_r$ and the Cauchy theorem reads

$$\int_{-\infty}^{\infty}\frac{F(\omega)}{(\omega_i-\omega)}d\omega = 2i\pi F(\omega) + \wp\int_{-\infty}^{\infty}\frac{F(\omega)}{(\omega_i-\omega)}d\omega, \tag{2.28}$$

where $\wp$ is the principle value of Cauchy. Plugging Eq. (2.27) in Eq. (2.28), we obtain[62]

$$\begin{aligned} C_f^{(2)} &= -\left(\frac{2\pi}{i\hbar^2}\right)\mu_{f,i}\mu_{i,g}\Bigg[2i\pi\tilde{E_{i,g}}(\omega)\tilde{E}(\omega_{f,g}-\omega) \\ &+\wp\int_{-\infty}^{\infty}\frac{\tilde{E}(\omega)\tilde{E}(\omega_{f,g}-\omega)}{(\omega_{i,g}-\omega)}d\omega\Bigg], \end{aligned} \tag{2.29}$$

where $\omega_{f,i}$ and $\omega_{i,g}$ are the resonant frequencies, as depicted in Fig. 2.3. As can be seen from Eq. (2.29), the first term depends only on the resonant components, whereas the second term integrates over the contribution of all other spectral components of the pulse. Because the lifetime of the final state $|\psi_f\rangle$ is longer then the pulse duration, the final state population is the integration over all possible photon pairs $(\omega)$ and $(\omega_{f,g} - \omega)$ that add up to $\omega_{f,g}$.

It is instructive to examine the two terms i.e. the resonant and the nonresonant in more detail. For a transform limited pulse both terms contribute to the final state population without interference, since the first term is imaginary and the second term real. Looking at the nonresonant term, one observes a sign change (phase change of $\pi$) below and above the resonance $\omega_{i,g}$. This has two consequences, first the nonresonant term is zero when the single resonant intermediate state coincides with the pulse central frequency $\omega_{i,g} = \omega_c$ and the intermediate state is perfectly half way in the three-level system $(\omega_{f,g}/2)$. In this case, the final state population is solely determined by the resonant contribution. Secondly, a transform limited femtosecond pulse is not the optimal pulse for population transfer, as shown by Dudovich *et al.*[62]. Their results show that the two-photon absorption process could be enhanced by a factor of 7, simply by using a $\pi/2$ step phase-mask at frequencies between the two resonances. In this way, the integrant in Eq. (2.29) is positive for all $\omega$.

### Nonresonant two-photon absorption in multi-level systems

In similar fashion, a purely nonresonant TPA process can also be described by second-order perturbation theory and implies that all intermediate states are far from resonance. The contribution of all intermediate levels adds up coherently only for a short time duration and we can approximate[20]

$$\begin{aligned} &= \sum \mu_{f,n}\mu_{n,g} \exp\left[i\omega_n(t_2 - t_1)\right] \\ &\simeq \left\{ \begin{array}{cc} \langle f|\mu^2|g\rangle, & |t_2 - t_1| < \bar{\omega}^{-1} \\ 0, & |t_2 - t_1| \geqslant \bar{\omega}^{-1} \end{array} \right. , \end{aligned} \tag{2.30}$$

where $\hbar\bar{\omega}$ is an appropriately weighted average energy, which defines merely the lifetime of the virtual level[63]. Using the projection operator $P = \sum_i |i\rangle\langle i| = 1$, Eq. (2.21) and Eq. (2.30), the nonresonant excited state amplitude for a TPA process can be approximated by

$$C_f^{(2)} = \left(\frac{2\pi}{i\hbar^2}\right) \frac{\mu_{f,i}\mu_{ig}}{\bar{\omega}} \int_{-\infty}^{\infty} d\omega \tilde{E}(\omega)\tilde{E}(\omega_{f,g} - \omega) \tag{2.31}$$

In case of one nonresonant intermediate state being dominant, we also can approximate an appropriately weighted average frequency in Eq. (2.27) by $\frac{1}{\omega_{n,g}-\omega} \approx \bar{\omega}^{-1}$, which is constant and can be taken out from the integration. Note that $\varepsilon(\omega)$ is real and $\tilde{E}(\omega) = \tilde{E}^*(-\omega)$.

Equation (2.31) reflects that the TPA process occurs for all photon pairs within the bandwidth of the pulse with frequencies $\omega_1 + \omega_2 = \omega_{f,g}$. In chapter 3 of this thesis, stimulated Raman is studied, which is also a nonresonant TPA process. All photon pairs within the bandwidth of the pulse with difference frequencies $\omega_1 - \omega_2 = \omega_{f,g}$

contributes to population transfer. In case of stimulated Raman, $\omega_{f,g}$ equals a molecular rotational or vibrational transition and the transition amplitude is approximated by

$$C_f^{(2)} \approx \int_{-\infty}^{\infty} \tilde{E}(\omega)\tilde{E}^*(\omega - \omega_{f,g})d\omega. \tag{2.32}$$

A transform limited pulse yields the most effective excitation. As it can be shown that the integrated contribution is proportional $\int_{-\infty}^{\infty} I(t)e^{i\omega_{f,g}t}dt$, which is the resonant frequency component of the intensity $I(t)$. Most spectral modulations will attenuate the Raman yield. However, periodic phase functions of $\pi/2$ with periodicity $\omega_{f,g}$ transfer the same amount of population despite the pulse structure is longer than a bandwidth limited pulses and less intense. Such phase functions will split an initial transform limited pulse in a pulse sequence (see Section 1.5.2) with a repetition time $\omega_{f,g}/2\pi$. Tuning the periodicity of the phase function gives control on the Raman yield[64,65]. In Chapter 3, we show that a two-pulse sequence provides the selectivity to excite or de-excited desired states in the rotational ladder of nitric oxide.

# CHAPTER 3

# Controlling rotational state distributions using two-pulse stimulated Raman excitation

The femtosecond stimulated Raman process is a versatile technique to excite rotational states in molecules. We demonstrate control over the rotational state population in a sample of NO molecules by varying the time delay between two identical laser pulses. Product of the rotational state distribution is probed by a 1+1 REMPI scheme and simulated quantum mechanically. There is good agreement between theoretical and experimental results. The product in selected quantum states show an oscillatory dependence on the time-delay. Spectral analysis reveals rotational transition energies and the presence of multiple Raman steps. We show that the relative strength of these frequency components can be related to excitation pathways with predominant $\Delta J = 2$ transitions towards higher rotational states. The initial step from $J = 1/2$ involves either $\Delta J = 1$ or $\Delta J = 2$. We find that one can discriminate between two excitation ladders. The results demonstrate the coherent effects of tailoring the shape of an ultra short excitation pulse.

**Phys. Rev. A** 76, 023411 (2007)[65]

## 3.1 Introduction

In studies of molecular structure and reactivity, initial quantum state preparation of the molecular sample is a vital element. Electronic, vibrational and rotational excitation have a profound influence on bi-molecular reaction rates and the outcome of photo-induced uni-molecular reactions[66]. Electronic excitation alters the potential energy surfaces that are relevant to a chemical reaction, vibrational excitation alters the distribution of configurations that participate in the experiment and rotational excitation affects the angular properties of both photonic, electronic and atomic/molecular collisions. For instance, in atom-molecule collisions a strong influence of the collision cross sections on the alignment and orientation of the collision partners has been observed[67], while in optical experiments a strong dependence of excitation and ionization rates on molecular alignment is the rule rather than the exception[68]. Furthermore, the dependence of processes like high harmonic generation on molecular alignment has recently been exploited in orbital tomography experiments where the ground state wave function of small molecules like nitrogen has been determined[69].

In the pursuit of experimental control over molecular initial quantum state preparation, beam expansion techniques are often a first step to limit the number of states involved[70]. In a supersonic expansion substantial cooling of the internal degrees of freedom can be achieved. When combined with electrostatic multipole fields full state-selection becomes possible[71]. Molecules with permanent dipole moments such as NO, OH, $CH_3I$ and others can be focused in specific states that may behave substantially different from the mixture of states in a beam after expansion[72]. Moreover, such selected states can subsequently be oriented so that the two 'ends' of the molecule selectively point in specific directions[73].

Optical excitation provides an alternative means of preparing quantum states. Resonant photo-absorption and two-color Raman excitation or stimulated emission pumping are common techniques to state-selectively prepare atoms or molecules prior to their use in a collision experiment[74–77]. In many of these experiments the narrow bandwidth of a tunable laser or an optical parametric amplifier provides the means to control the excitation. A particularly interesting preparation scheme has been stimulated rapid adiabatic passage (STIRAP) where two narrowband nanosecond lasers are used in a counter-intuitive time sequence to accomplish complete population transfer from an initial state to a selected target state[78]. STIRAP has been used to generate vibrationally pure samples[79] and can be viewed as a first example of the use of coherent control (CC) as a means to achieve quantum state preparation in a controlled manner[18,20,21,80–82].

More recently, efforts to control molecular quantum state preparation have increasingly made use of femtosecond laser techniques. The very short interaction time that can be achieved with femtosecond lasers means that undesirable processes such as intra-molecular vibrational relaxation (IVR) can be avoided. At the same time the high peak power of most femtosecond laser sources allows for manipulation by means of non-linear excitation.

The broad bandwidth of femtosecond pulses and the availability of tools to experimentally control the spectral amplitude-, phase- and/or polarization of the pulses, provide the experimentalist with a large number of "control knobs", that allows that a quantum mechanical system can be steered into a desired quantum state. The use of these degrees of freedom under control of a genetic or evolutionary algorithm has led to the development of the popular field of laser optimal control[21,41,48].

In the present paper, we will be concerned with the application of femtosecond lasers towards controlling the preparation of rotationally excited molecular samples as well as the molecular alignment that accompanies the excitation. When molecules are placed at the focus of an intense laser field, they undergo so-called dynamic alignment. In this process the most polarizable axis of a molecule aligns itself to the polarization axis of the laser. If the laser field is turned on and off very slowly, then the molecular axes slowly adapt to the laser field, and the alignment that occurs during the pulse disappears when the pulse is over[83]. However, if the laser pulse is turned on and off very fast, within a small fraction of the rotational period of the molecule, then the laser excitation leads to the formation of a rotational wavepacket, and the molecule displays alignment both during and after the laser excitation pulse. In the latter case the alignment reoccurs under field-free conditions at revival times that are determined by the rotational constant(s) of the molecule[84,85]. Quantum mechanically, both adiabatic and non-adiabatic dynamic alignment are understood in terms of the formation of a rotational wavepacket by means of a sequence of stimulated Raman-transitions that couple different rotational energy levels of the ground state molecule. Dynamic alignment can be probed by means of Coulomb explosion imaging[85], by means of dissociative ionization using an ultrashort extreme-ultraviolet pulse[86] or by its manifestation in time-domain measurements[87–90]. In fact, one of the most important applications of the use of Femtosecond Stimulated Raman (FSR) schemes has been the development of several rotational recurrence spectroscopies, that have allowed the determination of the rotational constants of moderately large molecules[91]. Alternatively, the induced time-dependent macroscopic polarization may also be a source of ultra fast THz radiation[92], or can be used to compress of femtosecond pulses to the few-cycle limit[93,94].

Recently, Hasegawa and Ohshima[95] investigated the rotational state distribution in non-adiabatic rotational excitation of a sample of cold NO molecules by a single femtosecond pulse. They focussed on the dependence of this distribution on the laser intensity and were able to identify excitation pathways typical to molecules in a doubly degenerate state. We studied the rotational excitation of NO molecules after a sequence of two identical femtosecond pulses with a variable time-delay. The Fourier spectrum of the two pulses changes as function of the delay and allows one to control coherently the excitation to the different rotational levels.

Population transfer occurs whenever the energy difference between rotational states is within the bandwidth of the laser. The non-resonant transition amplitude ($\alpha^{(2)}_{FSR}$) associated with FSR processes, can - in a perturbative picture - be approximated by[62,96]:

$$\Gamma^{(2)}_{FSR} \approx \int_{-\infty}^{\infty} E(\omega)E^{*}(\omega - \omega_{J,J'})d\omega, \tag{3.1}$$

where $E(\omega)$ is the Fourier Transform of the time-dependent electric (laser) field. $J$ and $J'$ provide the total angular momentum quantum numbers before and after the laser interaction, respectively. As the Stokes electric field is the complex conjugate of the pump electric field, the transition amplitude may be affected by the relative phase of the different frequencies in the pulse. In the special case of Fourier Transform Limited pulses, $E(t)$ is real and only the spectral amplitude of the photon pairs is relevant. By modifying the power spectrum of the ultra short pulse, one can achieve control over the excited rotational state population. If one uses two identical femtosecond pulses with a relative time delay $\Delta T$, then the spectral distribution contains a fringe pattern with a fringe spacing $\Delta\omega_{fr} = 2\pi/\Delta T$. When multiple of the fringe spacing matches the frequency of a rotational transition, $\Delta\omega_{fr} = n\omega_{J,J'}$, the FSR excitation probability has a maximum, since both photons necessary to drive this process are present in the spectral distribution. When the fringe period equals $\Delta\omega_{fr} = (n+\frac{1}{2})\omega_{J,J'}$, however, the transition amplitude has a minimum since at frequencies where the fringe pattern has a maximum, no suitable accompanying photons exist. We note that the FSR efficiency never becomes zero when using two pulses. From the above, we can easily predict optimum time delays for excitation to different rotational states. An alternative view of the action of the two pulses is that the first pulse produces a rotational wave packet, where the second pulse is either in phase such that the amplitude transferred by the second pulse is in phase with the amplitude transferred by the first pulse, or out of phase, such that the excited state population is coherently pumped back to the initial state.

With the intensity and bandwidth of present day femtosecond pulses, multiple Raman steps within one pulse are possible. The duration of a femtosecond pulse is considerably shorter than lifetimes and decoherence times of the created wave packets. Hence, stimulated Raman excitation is a way to coherently and selectively prepare rotationally excited samples of molecules that can subsequently be used in (collision) experiments.

## 3.2 Experiment

The experiments were performed in the setup that is depicted in Fig. 3.1. A molecular beam, consisting of $\sim 2\%$ NO seeded in Ar, was generated using a pulsed water-cooled Jordan valve with a stagnation pressure of 3 bar. The valve was followed by a skimmer with an opening of 1 mm. The rotational temperature of the NO molecules was estimated to be 5K (+5K / - 2K), based on the measured rotational state population.

The cold NO beam was crossed by two femtosecond (pump) laser pulses with a variable time delay, up to 20 ps. The initial pulses were generated by a 1 kHz regeneratively amplified Ti-sapphire laser producing transform limited 300 $\mu$J pulses of $\sim$150 fs. A Michelson interferometer with a computerized motor-driven delay stage was used to split the pulse and controlled the relative time delay between the coherent pulses in time steps of approximately 0.14 ps. Temporal overlap of the pulses was deduced from the typical fringe pattern. The femtosecond pulses were focused onto the molecular beam with a 300 mm lens. The focus conditions were chosen such that no direct ionization signal was observed from the femtosecond laser. We estimate the pulse intensity at the interaction region to be equal to $2.8 * 10^{12} Wm^{-2}$.

Population changes in each rotational state of NO where probed, 50 ns after interaction with the femtosecond pulses, using the $R_{21}$ branch of a (1+1) REMPI scheme along the electronic $A^2\Sigma^+ \leftarrow X^2\Pi$ transition. A mildly-focused 200 $\mu$J laser pulse from a tuneable dye laser, tuned around 225 nm, was used for both excitation and ionization. The frequency-doubled output of a YAG-pumped dye laser system (using Coumarin 450) had a resolution of 0.1 cm$^{-1}$. To enhance the S/N ratio, the probe

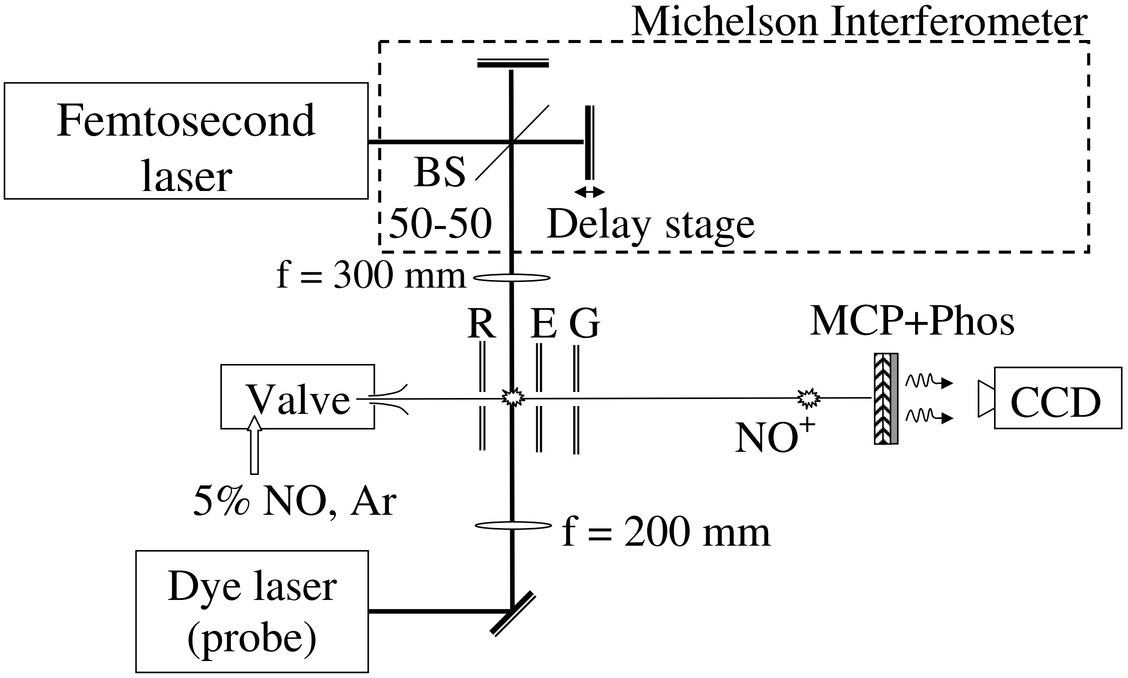

**Figure 3.1:** A beam of rotationally cold NO seeded in Ar was expanded in vacuum and crossed by two lasers. An amplified Ti-Sapphire laser is used for stimulated Raman excitation and a tunable dye laser at 20 Hz for state selective ionization of NO rotational levels. The Michelson interferometer produces two identical pulses with a relative delay between 0 and 20 ps. Ion optics transport the NO ions to a MCP detector. A CCD camera is used to quantify the $NO^+$ yield.

laser was focused with a 200 mm lens to a beam waist smaller than the pump laser.

The produced $NO^+$ ions were accelerated in an electrostatic field and subsequently detected by a time-gated set of micro-channel plates (MCP), followed by a phosphorous screen and a CCD-camera (LaVision). The ions were de-focused to avoid saturation of the MCP detector. It should be noted that the detector was built for velocity map imaging, but was not used as such in this experiment.

The 1 kHz femtosecond laser was used as master trigger and a 20 Hz signal was extracted to synchronize the YAG-dye laser system while the Jordan valve, MCP and the camera were operated at 10 Hz. The time delay between the pump laser, the probe laser and the molecular beam was controlled using a digital delay generator (SRS DG-535).

Multi-photon ionization of $NO(A^2\Sigma^+)$ molecules by the femtosecond laser was used to find overlap between the pump and probe lasers. The direct CCD signals after integration are presented in Fig. 3.5. The constant background in the experimental results is presumably due to $J \neq 1/2$ state population in the NO beam. The noise is attributed predominantly to power fluctuations of the dye laser as well as the femtosecond laser and intensity fluctuations of the NO molecular beam.

The experimental results will be discussed and compared to simulations in section

3.4. Before that, we will describe the quantum mechanical treatment providing the theoretical results.

## 3.3 Theory

The presented experiments involve multiple Raman transitions from pairs of femtosecond pulses and allow for an exact quantum mechanical treatment. The Nitric Oxide (NO) molecule has a degenerate $^2\Pi$ open shell ground state resulting in half integer total angular momentum quantum numbers[97–99]. The rotational energy levels of the NO molecule are given by Zare[98] (page 303), providing two regular rotational ladders for the two molecular spin-orbit states:

$$\begin{aligned} E_{rot}(J) = \Big(J - \frac{1}{2}\Big)\Big(J + \frac{3}{2}\Big) \\ \pm\sqrt{4\Big(J + \frac{1}{2}\Big)^2 + Y\Big(Y - 4\Big)} \mp (Y - 2), \end{aligned} \tag{3.2}$$

with

$$Y = \frac{A}{B}.$$

Note that $E_{rot}$ is dimensionless and is given in units of the rotational constant $B$. The spin-orbit constant $A$ and the rotational constant necessary to calculate the rotational energy of a NO molecule in the $\nu = 0$, $X^2\Pi$ state are $A = 123.13\ cm^{-1}$ and $B = 1.6961\ cm^{-1}$ [100]. The ± sign in Eq. (3.2) distinguishes between (+) the upper $F_2$ ($\overline{\Omega} = \frac{3}{2}$) and (-) the lower $F_1$ ($\overline{\Omega} = \frac{1}{2}$) spin-orbit states ($\overline{\Omega}$ is the absolute value of the projection of the total angular momentum onto the internuclear axis $\Omega$). For NO, the two spin orbit states differ by 121 $cm^{-1}$ in energy. In the current work - due to cooling in the gas jet - most molecules will be in the lower ($F_1$) state and those in the $F_2$ state will be neglected.

For the $^2\Pi_{\frac{1}{2}}$ states that are well approximated by Hund's case (a) coupling, the $\Lambda$-type splitting is sufficiently small to be neglected in the experiments described in this work. Both $\Lambda$-doublet components (having opposite parity) are equally populated in the molecular beam. It is however possible (using for example a hexapole) to select a single component and therefore we will not sum over the $\Lambda$-doublet components $\epsilon = -1, 1$ ($\epsilon$ is the symmetry index) at this point. As a consequence of the presence of the two electronic parities in NO, the selection rule of $\Delta J = 2$ does not hold for Raman transitions in molecules with a $\Pi$-character ground state and $\Delta J = 1$ is also allowed[101]. The total parity $p$ of a NO rotational state is provided by Brown *et al.*[102].

$$p = (-1)^{J-\epsilon/2}. \tag{3.3}$$

A Raman transition requires conservation of total parity and thus for $\Delta J = 1$ it is necessary that $\epsilon = -\epsilon'$ and a $\Delta J = 2$ transition can only occur if $\epsilon = \epsilon'$.

The interaction potential between a molecule and a non-resonant linearly polarized laser field can be written as[103]:

$$\begin{aligned} V &= -\Delta\omega \cos^2\theta + \omega_\perp, \\ &= -\frac{2}{3}\Delta\omega P_2(\cos\theta) + \frac{1}{3}\Delta\omega + \omega_\perp, \end{aligned} \tag{3.4}$$

with dimensionless parameters:

$$\omega_{||,\perp} = \frac{\alpha_{||,\perp} I_l}{2B} \quad \text{and} \quad \Delta\omega = \omega_{||} - \omega_{\perp} = \frac{\Delta\alpha I_l}{2B}.$$

In these equations, $\theta$ is the angle between the laser polarization and the molecular axis and $I_l$ is the time-dependent laser intensity. As the term $1/3\,\Delta\omega + \omega_\perp$ is constant (independent of the rotational state) for a symmetric top, it will be neglected from here onwards. For this reason, only the polarization anisotropy $\Delta\alpha = \alpha_{||} - \alpha_\perp$ is needed in the calculations.

The rotational part of the NO wave function (assuming Hund's case (a)) is given by:

$$|J, \overline{\Omega}, M, \epsilon\rangle = \frac{1}{\sqrt{2}}\Big[|J\overline{\Omega}M\rangle + \epsilon|J - \overline{\Omega}M\rangle\Big], \tag{3.5}$$

with M being the space quantization of the rotational states and total Hamiltonian by (note $M = M'$ and $\overline{\Omega} = \overline{\Omega}'$):

$$\begin{aligned} H^{M,\overline{\Omega}}_{J,J',\epsilon,\epsilon'} &= \langle J', \overline{\Omega}, M, \epsilon'|H_{rot} - \frac{2}{3}\Delta\omega P_2(\cos\theta)|J, \overline{\Omega}, M, \epsilon\rangle, \\ &= E_{rot}(J)\delta_{J',J} - \frac{1}{3}\Delta\omega\sqrt{(2J+1)(2J'+1)} \\ &\quad \begin{pmatrix} J' & 2 & J \\ M & 0 & -M \end{pmatrix} \times \Bigg[(-1)^{M-\overline{\Omega}} \begin{pmatrix} J' & 2 & J \\ \overline{\Omega} & 0 & -\overline{\Omega} \end{pmatrix} \\ &\quad + (-1)^{M+\overline{\Omega}}\,\epsilon\epsilon' \begin{pmatrix} J' & 2 & J \\ -\overline{\Omega} & 0 & \overline{\Omega} \end{pmatrix}\Bigg]. \end{aligned} \tag{3.6}$$

As mentioned above, the equation predict $\Delta J = 1$ ($\epsilon' = -\epsilon$) and $\Delta J = 2$ ($\epsilon' = \epsilon$) transitions. The J-dependent matrix elements contain the 3j-symbols and are directly related to rotational transition probabilities. For increasing values of $J$, the $J$-dependent matrix elements clearly favor $\Delta J = 2$ transitions as shown in Fig. 3.2. For example, for $J = 1/2 \rightarrow J'$, the matrix elements for $\Delta J = 1$ and $\Delta J = 2$ are 0.283 and 0.346, respectively, whereas for $J = 5/2 \rightarrow J'$, these values are 0.0329 and 0.369.

The Hamiltonian is averaged over the rapid oscillations of the laser field. For the 800 nm wavelength used and in the case of NO, the rapid oscillations can be eliminated since the laser frequency is far away from any resonances and thus the population transfer is adiabatic. Cos$^2$-pulses have been used in the calculations, where the laser intensity for a single pulse (within $-\tau \leq t \leq \tau$) is approximated by

$$I_l(t) = I_0 \cos^2\left(\pi t \;/\; 2\tau\right). \tag{3.7}$$

The time for the pulse to rise from zero to the peak intensity ($I_0$) is indicated by $\tau$ and is also the full width at half maximum of the pulse. In the time between the two laser pulses the Hamiltonian is independent of time and an analytical expression for time evolution can be used. This way, the need of numerical integration in between the two femtosecond pulses is avoided. The delay $\Delta T$ between two laser pulses is

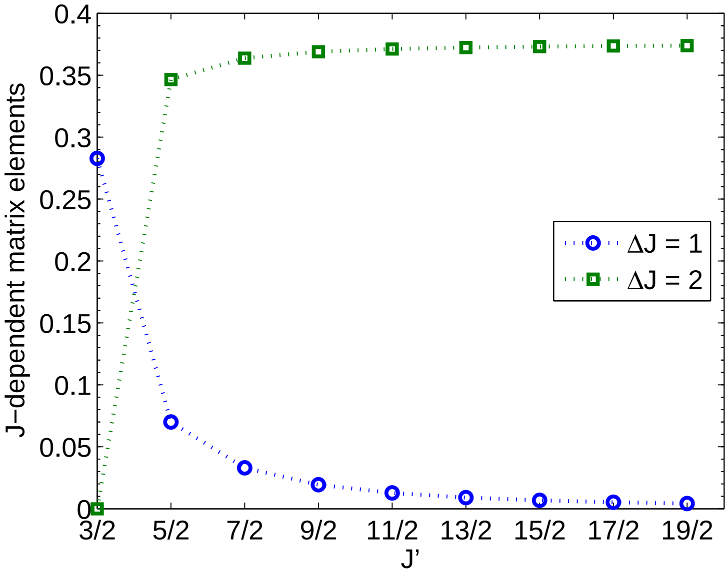

**Figure 3.2:** The overall $J$-dependence of the matrix elements for $\Delta J = 1$ and $\Delta J = 2$ transitions. With increasing values of $J$, the coefficients favors a $\Delta J = 2$ excitation. $J'$ indicates the state after the laser pulse.

specified as the time between their maxima. The pulse sequence $I_l(t)$ is described as:

$$\begin{array}{rcl} I_0 \cos^2(\pi t \;/\; 2\tau) & \text{for} & -\tau \leq t \leq \tau \\ 0 & \text{for} & \tau \leq t \leq \Delta T - \tau \\ I_0 \cos^2(\pi(t-\Delta T) \;/\; 2\tau) & \text{for} & \Delta T - \tau \leq t \leq \Delta T + \tau. \end{array} \tag{3.8}$$

Note that in Eq. (3.8), as in Fig. 3.4, $t = 0$ corresponds to the moment at which the first pulse reaches a maximum intensity.

With this expression for the laser intensity, we can propagate the rotational wave function by solving the time-dependent Schrödinger equation numerically:

$$i\hbar \frac{\partial \Psi}{\partial t} = H(t)\Psi. \tag{3.9}$$

For small steps $\Delta t$:

$$\Psi(t + \Delta t) = U(t)\Psi(t), \tag{3.10}$$

where,

$$U(t) = 1 - \frac{i\Delta t}{\hbar} H(t). \tag{3.11}$$

During both laser pulses, the wave function is propagated numerically. In between the laser pulses, the Hamiltonian is independent of time and the behavior of the wave function is described with:

$$\Psi(t) = \Psi(\tau)\; e^{-iE_{rot}(t-\tau)/\hbar}. \tag{3.12}$$

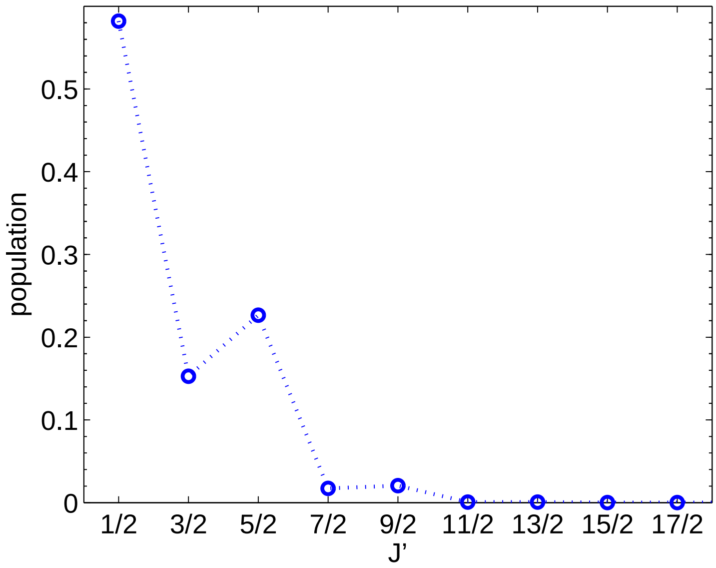

**Figure 3.3:** The simulated redistribution of the population to different rotational levels starting from the $J = 1/2$ for a single 150 fs laser pulse ($\Delta\omega = 49$). Both components of the $\Lambda$-doublet are equally populated, which means that all $J'$ states can be populated after the laser pulse. $J'$ indicates the final state. Note, however, that the $J = 5/2$ state is more populated than the $J = 3/2$ state.

The experiment involves scanning the time delay between the two identical femtosecond pulses while probing the asymptotic population of selected final states. We numerically solve Eq. (3.6) using $\Delta\alpha = 2.8$ $\mathring{A}^3$ [104a], $\tau = 150$ fs, with time steps of 0.1 fs during the laser pulses. The time delay between the pulses was varied from 0 to 20 ps in steps of 0.05 ps. The laser intensity in the experiment leads to $\Delta\omega = 49$. Figure 3.3 shows the calculated redistribution after one pulse starting from $J = 1/2$ (both $\Lambda$-components equally populated). One can observe that $J = 5/2$ is more populated than $J = 3/2$.

The redistribution of the population is highly pulse energy dependent and towards higher intensities almost complete depletion of the ground state can be observed[95]. In Fig. 3.4 we present a sample calculation that follows the populations of the different states as function of time, showing the selectivity in generating selected excited states using two 10.14 ps time delayed pulses. This sample calculation clearly shows how the use of a two pulse sequence allows selective excitation of specific rotational levels. The population of $J = 3/2$ disappears by the second femtosecond pulse, whereas the population of other states increase. Some states are pumped back by the second pulse, other grow about a factor of 4 due to the time dependent phase of the different $J$-states. Obviously, the two time delayed pulses have a considerable impact on the asymptotic population transfer.

---

[a] Remark: the polarization anisotropy $\Delta\alpha$ should be 0.82 $\mathring{A}^3$ [105]. This leads to an experimental laser intensity of $\Delta\omega = 167.32$.

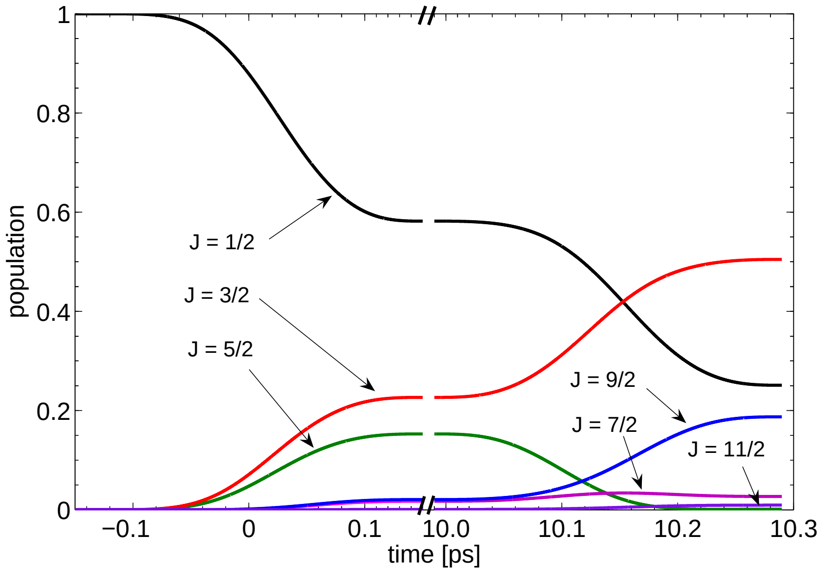

**Figure 3.4:** The time-dependent asymptotic population of the selected final state $J = 1/2, 3/2, 5/2, 7/2, 9/2$ and $11/2$ using two 150 fs pulse time delayed by 10.14 ps. At this particular time delay, the second pulse favors the states $J = 5/2$ and $9/2$ to be populated, while $J = 3/2, 7/2$ and $11/2$ are almost depleted. The redistribution after the pulse sequence shows selectivity in generating selected excited states. Note that the first pulse is set to have a maximum at t = 0.

## 3.4 Results and discussion

The dependence of the population of the NO ($J = 1/2 \dots 11/2$) rotational levels on the time delay between the femtosecond pulses is depicted in Fig. 3.5. Experimental and theoretical results are plotted in the same figure. A small and constant background signal is subtracted. This experimentally observed background is presumably due to nascent NO($J \neq 1/2$) in the beam and decreases with an increase of the final rotational state. The graphs in Fig. 3.6 show the Fourier spectra of the results in Fig. 3.5. Our calculations indicate that a depletion of the initial ($J = 1/2$) state can be as large as 90% at specific time delays. An attempt to detect this depletion failed, as the high efficiency of the (1+1) REMPI process makes it impossible to limit the probe region to the focus of the femtosecond laser only. Therefore there is no experimental result for $J = 1/2$ in Figs. 3.5 and 3.6. Only theoretical results are plotted in Figs. 3.5(a) and 3.6(a). Note that the sum over the rotational states of the theoretical results equals 1 for every delay.

The time traces and the Fourier spectra in Fig. 3.5 and Table 3.1, reveal a good overall agreement between the theoretical and experimental results for all but the highest rotational states, $J = 11/2$.

The simulations were preformed up to a delay of approximately 20 ps to match the experimental conditions. The peaks are labeled as $\nu_{n,m} = (E_{rot}(\frac{m}{2}) - E_{rot}(\frac{n}{2}))/h$. Table 3.1 lists the relevant rotational transition frequencies as well as cross-correlation frequencies, which are the sum and difference frequencies thereof. Due to the regular spacings between the rotational energy levels, some cross-correlation frequencies in

**Table 3.1:** The oscillating population in the different rotational states has frequencies which equals rotational transition frequencies: $\nu_{n,m} = (E_{\frac{m}{2}} - E_{\frac{n}{2}})/h$ and the cross-correlation frequencies which appear in the spectra indicate that multiple Raman steps are made. The frequencies obtained from calculations which could not be detected in the experimental data are marked as (-).

| Transition | Frequency [a] (THz) | J3/2[b] | J5/2[b] | J7/2[b] | J9/2[b] | J11/2[b] |
|---|---|---|---|---|---|---|
| $\nu_{1,3}$ | 0.15 | 0.15 | 0.15 | 0.15 | 0.15 | 0.15 |
| $\nu_{3,5}$ | 0.25 | - | - | - | - | - |
| $\nu_{5,7}$ | 0.35 | | | - | | - |
| $\nu_{1,5}$ | 0.40[c] | | 0.40[c] | | 0.40 | |
| $(\nu_{7,11} - \nu_{3,7})$ | 0.40[c] | 0.40 | | | | 0.40 |
| $(\nu_{5,9} - \nu_{1,5})$ | 0.40[c] | | 0.40[c] | | 0.40 | |
| $\nu_{3,7}$ | 0.59 | - | | 0.59 | | 0.59 |
| $(\nu_{3,7} + \nu_{1,3})$ | 0.74 | - | | 0.74 | | - |
| $\nu_{5,9}$ | 0.79 | | 0.79 | | 0.79 | |
| $\nu_{7,11}$ | 0.99 | | | | | 0.99 |
| $(\nu_{5,9} + \nu_{1,5})$ | 1.19 | | 1.19 | | 1.19 | |
| $(\nu_{7,11} + \nu_{3,7})$ | 1.58 | | | - | | - |

[a] Calculated rotational transition frequencies using Eq. (3.2)[98].

[b] Experimental resolved rotational frequencies.

[c] Identical frequencies, whereas the assignment follows from Fig. 3.5.

Table 3.1 are identical to transition frequencies. If the assignment could not be made unambiguously, peaks were labeled according to the highest (theoretical) transition probability as provided in Fig. 3.2. The height of the peaks in the Fourier spectra indicates how strong rotational transitions (and combinations thereof) are involved in populating and depopulating the concerned rotational state.

Figure 3.5(b) shows the result of probing the $J = 3/2$ state. A dominant slow oscillation is observed corresponding to the rotational transition frequency $\nu_{1,3}$ of 0.15 THz. The smaller oscillations seen in the calculations are not resolved experimentally. That multiple frequencies play a role in populating and depopulating the $J = 3/2$ level is clear from the asymmetry of the observed recurrences. These substructures are due to subsequent Raman steps to higher rotational states, which depopulate the $J = 3/2$ state. The difference frequency $(\nu_{7,11} - \nu_{3,7})$ appear in the Fourier spectra, see Fig. 3.6(b), when a sequence of Raman steps takes place. For example: when starting from $J = 3/2$, first the $J = 7/2$ state may be populated, followed by excitation to $J = 11/2$. The time trace of $J = 5/2$ in Fig. 3.5(c) shows oscillations with a period equal to a transition of $\nu_{1,5}$. Moreover, experimental dips are observed in the population near the maxima. These dips can be attributed to depletion of the rotational state $J = 5/2$ due to further excitation to the $J = 9/2$ state. The corresponding Fourier spectrum in Fig. 3.6(c) shows also a peak at 1.14 THz, which corresponds to the sum frequency $(\nu_{5,9} + \nu_{1,5})$. Note that the difference frequency $(\nu_{5,9} - \nu_{1,5})$ equals the transition frequency $\nu_{1,5}$ and cannot be distinguished. The simulations show contributions that can be labeled $\nu_{1,3}$ and $\nu_{5,9}$.

The delay dependent population of $J = 7/2$ in Fig. 3.5(d) shows frequencies corresponding to $\nu_{1,3}$, $(\nu_{3,7} + \nu_{1,3})$ and $\nu_{3,7}$. Note the very good agreement between experiment and simulation. Further note that the coherence is well preserved during the 20 ps delay. In the graph of $J = 9/2$ in Fig. 3.6(e), two strong contributions are visible in both the experimental and theoretical Fourier spectra at frequencies $\nu_{1,5}$ and $\nu_{5,9}$. The sum frequency $(\nu_{5,9} + \nu_{1,5})$ appear in the spectra. The small contribution of the transition frequency $\nu_{1,3}$ indicates that the excitation pathway to $J = 9/2$ favors two $\Delta J = 2$ transitions.

At relatively high rotational levels, the delay dependence of the population becomes more complicated and more frequencies are noticeable in the spectra. The $J = 11/2$ final rotational state is the highest one probed in this work. It is especially interesting as it requires at least three Raman steps starting from the ground state, encompassing a $\Delta J = 1$ transition. The experimental Fourier spectrum for $J = 11/2$ in Fig. 3.6(f) shows three transition frequencies corresponding to $\nu_{1,3}$, $\nu_{3,7}$ and $\nu_{7,11}$ with cross-correlation frequency $(\nu_{7,11} - \nu_{3,7})$. The $J = 11/2$ experimental and calculated delay-dependent populations are clearly different. This is remarkable in view of the good agreement of the other traces. The Fourier spectrum differs especially in the strength of the cross-correlation peak $(\nu_{7,11} - \nu_{3,7})$, the reason of this difference is not yet clear. Computational tests to determine whether part of the signal is due to nascent $J = 3/2$ NO molecules in the molecular beam did not produce a better agreement. A possible explanation is that our Hunds case (a) approximation for the NO rotational wave function breaks down at this rotational state.

Choosing a particular time difference between the two femtosecond pulses one has control over the final rotational state distribution, but one can not create a sample of molecules in a single excited rotational state in the current experiments. More specificity can in principle be achieved if Raman transitions are strongly saturated, which opens up the possibility of population transfer by adiabatic transfer mechanisms. In the current experiment, however, one can selectively discriminate between two different excitation paths, which we label as A($\nu_{1,3}$, $\nu_{3,7}$, $\nu_{7,11}$, ...) and B($\nu_{1,5}$, $\nu_{5,9}$, $\nu_{9,13}$, ...), climbing the rotational ladder with predominantly $\Delta J = 2$ transitions, see the inset in Fig. 3.7. The first step, starting from the $J = 1/2$ state, is either a $\Delta J = 1$ (A-path) or a $\Delta J = 2$ (B-path) transition. The formation of molecules in the $J = 3/2$ state is enhanced if the delay is $\Delta T = n/\nu_{1,3}$ (with $n = 1, 2, \ldots$), while its formation is minimized if $\Delta T = (n - 1/2)/\nu_{1,3}$. Maxima in the population of the state are found at $\Delta T = m/\nu_{1,5}$ with $m = 1, 2, \ldots$ while minima are observed at $\Delta T = (m - 1/2)/\nu_{1,5}$. For example, the B-ladder is maximized - while strongly suppressing the A-ladder - at a delay of $\Delta T = 10.14$ ps. Inspecting the time evolution of the different rotational states at 10.14 ps in Fig. 3.4 it is clearly seen that the $J = 3/2$ state is depopulated by the second pulse. The same holds for a time-delay between the two pulses of $\Delta T = 6.3$ ps, that minimizes the population transfer via the B-path.

Upon further inspection of Fig. 3.7 we observe nonzero populations for the $J = 7/2$ in the A-path and $J = 9/2$ in the B-path. Hence selectivity is not perfect for these states due to the presence of multiple Raman steps in each of the two fast pulses. This can be understood as the time delay is chosen to maximize selectivity at the first Raman step and in general then the following Raman steps can not give rise to complete depopulation or maximum population. No time delay $\Delta T$ can be found such

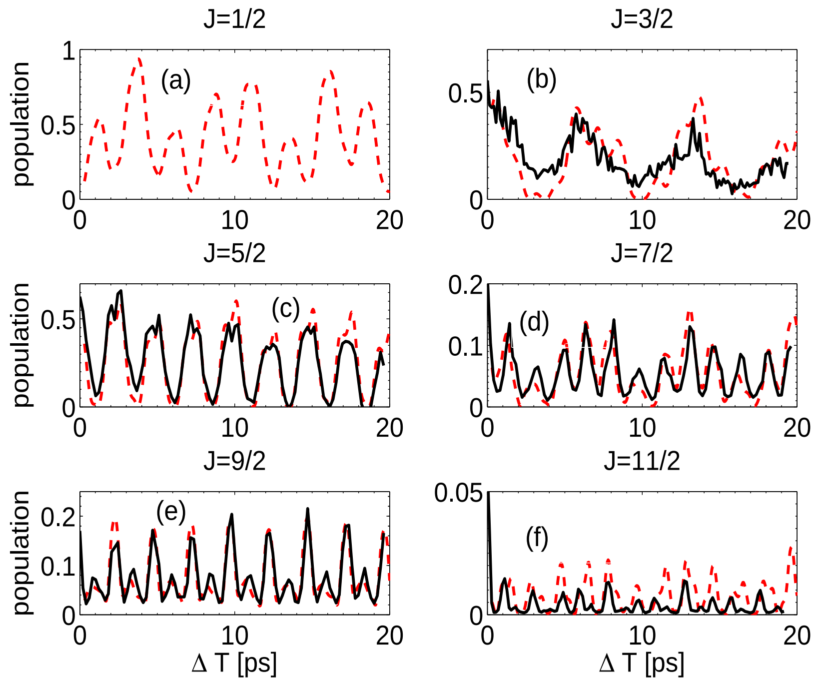

**Figure 3.5:** The experimental and simulated delay dependence of the NO rotational state population is depicted in six separate graphs for each final rotational state. Note that there is no experimental result for $J = 1/2$. The oscillating patterns consist of multiple frequency components, revealing the presence of multiple Raman steps. The Fourier spectra of these graphs are plotted in Fig. 3.6.

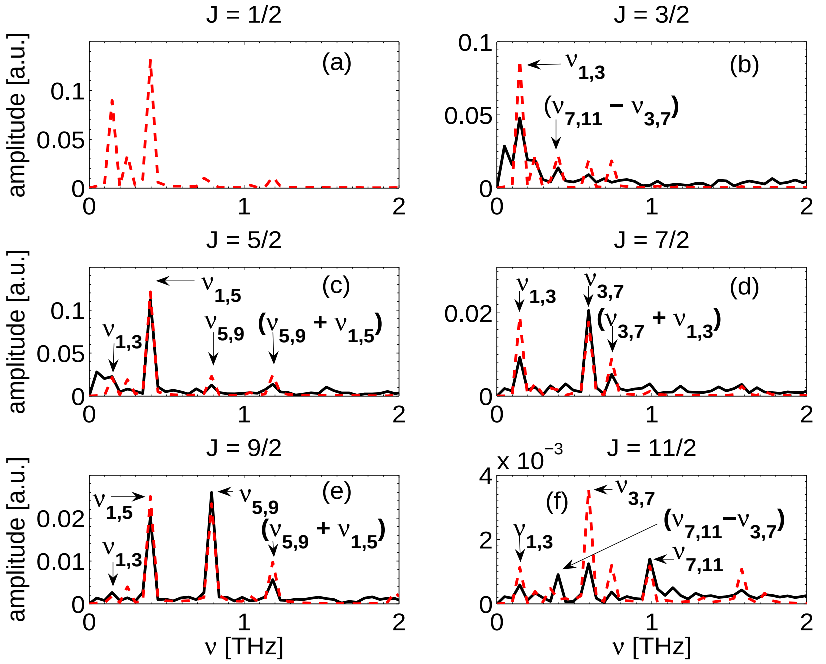

**Figure 3.6:** Fourier spectra of the experimental and simulated delay dependent behavior of the population in the $J = 1/2$, $J = 3/2$, $5/2$, $7/2$,$9/2$ and $11/2$ rotational states. The peaks in the spectra can be assigned to rotational transition and cross-correlation frequencies as provided in Table 3.1.

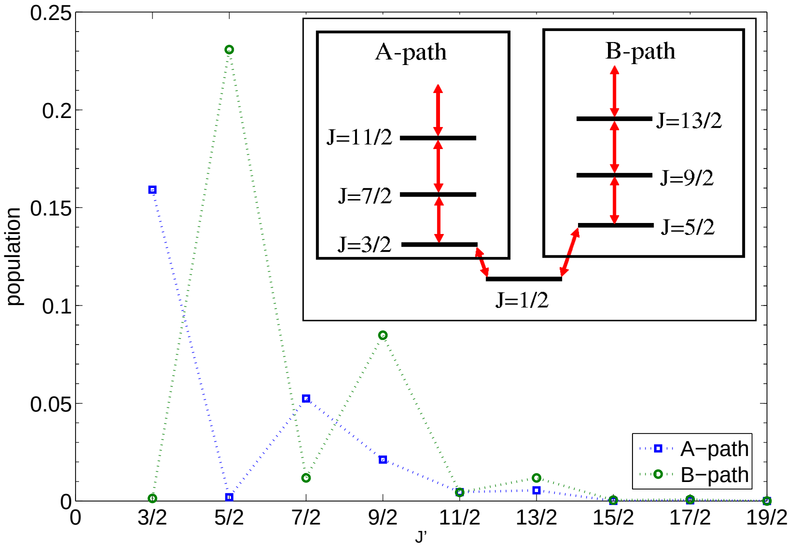

**Figure 3.7:** The redistributed population in the rotational states after a two pulse sequence excitation at a time delay of 6.31 ps (A-path) and 10.14 ps (B-path). At these particular time delays one can discriminate between two different excitation paths A($\nu_{1,3}$, $\nu_{3,7}$, $\nu_{7,11}$, ...) and B($\nu_{1,5}$, $\nu_{5,9}$, $\nu_{9,13}$, ...) with predominant ΔJ = 2 transitions towards higher rotational states. The inset depict the excitation paths from an initial state $J = 1/2$.

that $\Delta T = (n - 1/2)/\nu_{i,i+2}$ is obeyed for multiple values of $i$.

## 3.5 Conclusions and outlook

We demonstrated the ability to control the rotational state population of a sample of NO molecules by changing the time delay between two identical femtosecond laser pulses. Overall, good agreement is observed between the theoretical and experimental dependence of the population transfer on the delay between the pulses. The Femtosecond Stimulated Raman process is thus well understood and this opens possibilities to create molecular samples in specific rotational state distributions. In the current experiment however, with two delayed pulses, one cannot select any arbitrary rotational state distribution. Selectivity can be enhanced by the application of pulse shaping techniques. Even more selectivity can be realized when the Raman transitions are strongly saturated opening the possibility for population transfer by adiabatic processes.

Our results allow us to follow the rotational excitation process. Oscillations with frequencies that correspond to transition, sum and difference frequencies are observed in the delay-dependent population of each state. Fourier spectra of these traces reveal multiple Raman steps and the different quantum mechanical paths towards a final rotational state. The height of the peaks in the Fourier spectra indicates how strong rotational transitions are involved in populating and depopulating the concerned rotational state. A preference to climb the rotational ladder with $\Delta J = 2$ transitions - a strict selection rule for most other diatomic molecules - is observed towards high rotational states. Only one strong $\Delta J = 1$ transitions is observed ($J = 1/2 \leftrightarrow J = 3/2$)

and is resolved in the experimental Fourier spectra. It is this propensity for $\Delta J = 2$ transitions that allows selection of the two excitation paths: A($\nu_{1,3}$, $\nu_{3,7}$, $\nu_{7,11}$, ...) and B($\nu_{1,5}$, $\nu_{5,9}$, $\nu_{9,13}$, ...), where the initial step from $J = 1/2$ is either $\Delta J = 1$ or $\Delta J = 2$.

Perturbation theory, which uses the photon picture, provides an intuitive insight into the coherent effects of excitation by two time-delayed broadband femtosecond pulses. The spectral amplitude of the two pulses has fringes, which can maximize or minimize the Raman transition probability. The transition probability is maximized when the fringe-spacing corresponds to a transition frequency, which equals the energy difference between the rotational levels. Both photons needed in the stimulated Raman process are then present, one (pump) photon excites the molecule to a virtual state and it is stimulated back to a rotationally excited state by the other (Stokes) photon. As long as the bandwidth of the laser pulse encompasses the rotational transition frequencies one can selectively excite and align molecules. The corresponding 2.94 THz bandwidth of a 150 fs femtosecond pulse encompasses $\Delta$J = 2 rotational transition frequencies in NO up to J = 55/2. However, the maximum rotational excitation is limited by the intensity of the femtosecond pulses[95].

We may stress that in our experiments both a time-dependent[83,106–109] and a time-independent molecular alignment occurs. The time independent alignment is due to the conservation of $M$ and $\overline{\Omega}$ in the case of transitions by linearly polarized light. This alignment can be appreciated directly from our theoretical treatment and results in final states with $J$ up to 11/2, but always with $M = \pm 0.5$. The time dependent alignment is due to the formation of a rotational wavepacket, when using excitation pulses that are shorter than the rotational period of the molecules involved. In the present experiments we have limited ourselves to the effect of stimulated Raman transitions on the population of the rotational states, as we have no observable of the molecular alignment that is created in our molecular sample.

Future studies might involve searching for evidence of steady-state molecular alignment, as well as using pulse shaping to enhance the rotational state selectivity achieved in the current work. This technique of state selection via a femtosecond stimulated Raman process is versatile and allows one to control the rotational state distributions of dense samples of molecules. The excited and aligned molecular samples may find good use in experiments that study microscopic details of elementary processes using state selectivity and space quantization selectivity.

## Acknowledgments

The Netherlands Organization for Scientific Research (NWO) is gratefully acknowledged for financial support through CW and FOM. AG thanks Steven Stolte for useful discussions concerning the theoretical treatment described in this work. This work is part of the Stichting voor Fundamenteel Onderzoek der Materie (FOM) and was financially supported by the Nederlandse Organisatie voor Wetenschappelijk Onderzoek (NWO).

# CHAPTER 4

# The effects of narrow band pulse shaping on a resonant multi-level system

Phase- and amplitude modulation of small frequency ranges within broadband femtosecond pulses reshape these pulses providing transients before, before and after or only after the main femtosecond pulse. The absorbed or phase modulated frequencies appear as transients. We present experimental observations and calculations showing to what extent these transients can be used to drive population changes in the three-level 5s-5p-5d rubidium system in the perturbative limit. We also show computationally that these transients can assist to create nearly 97% population in the upper 5d state of rubidium at specific intensities.

Submitted to Physical Review A

## 4.1 Introduction

Coherent control of molecular and atomic processes is possible if the process being controlled is a multi-photon process. When using ultrafast pulses, one can change the amplitude, phase and/or polarization of individual frequency components that make up the femtosecond pulse. One immediate effect of tuning these parameters is a change in the pulse temporal profile, pulses get longer and obtain structure. It has now been demonstrated in many experiments that the outcome of the interaction of light can be influenced dramatically using coherent control[41,110,111]. A large body of research is devoted to steering interactions and reactions in specific directions using coherent control techniques.

Early experiments employed relative simple changes in the temporal profile of fast pulses. By applying a chirp, the pulse is lengthened while at the same time a frequency can be swept from red to blue or from blue to red. In simple three-level systems such as the one studied in this paper, it was shown that 100% population transfer to the final state is possible. The remarkable finding was that also a non-intuitive chirp is able to give 100% transfer[60].

In combination with pulse shapers and programmable spatial light modulators (SLM), arbitrary pulse shapes can be synthesized[112–116]. In simple systems one can predict a theoretical pulse shape that leads to the desired outcome. In complex molecular systems, genetic or evolutionary algorithms optimize desired outcomes of processes by looking for the ideal amplitude, phase and/or polarization distribution in order to achieve a preset goal[22,23,41,48,117]. The analysis of the optimized pulse structure should provide insight in the underlying processes. For example, a three-pulse sequence found when optimizing ionization rates in clusters revealed that two instants of time are favorable for energy absorption by the cluster[118]. These instances are related to enhanced ionization and resonant collective electron oscillations.

Upon propagation through an absorbing gas, semi-monochromatic transient electric fields appear behind the main pulse. Causality forbids a pre-transient. The resulting pulse is called a "$0\pi$" pulse. When these pulses interact with the same gas, no overall excitation takes place as has been shown theoretically[119] and experimentally[120–123]. However, excitation and de-excitation processes occur during these pulses as has shown experimentally by Dudovich *et al.*[124]. Beyond the perturbative regime pulses reshaped by absorption can give non-intuitive outcomes. For example, Gürtler and van der Zande[125] presented an observation of reshaped far-infrared terahertz pulses using selective absorption on water vapor. Although in the photon picture, the photons necessary to drive transitions in highly excited rubidium atoms were absent, it was found that the reshaped pulses enhanced the excitation rate.

In this paper, we show that coherent control through narrow band absorption modulation of ultra short pulses can be applied to selectively excite or deplete resonant states in a multi-level system (see Fig. 4.1(a)). We use a programmable spatial light modulator to simulate the linear combination of a frequency-dependent phase and amplitude, according to the Kramers-Kronig dispersion relation. This way, one can study separately the effects of power absorption and dispersion. We present calculations both in the perturbative regime and in the non-perturbative regime, showing the dependence of the coherent excitation on the semi-monochromatic transients. Near 100% population in the upper 5d state of rubidium can be achieved in a robust way.

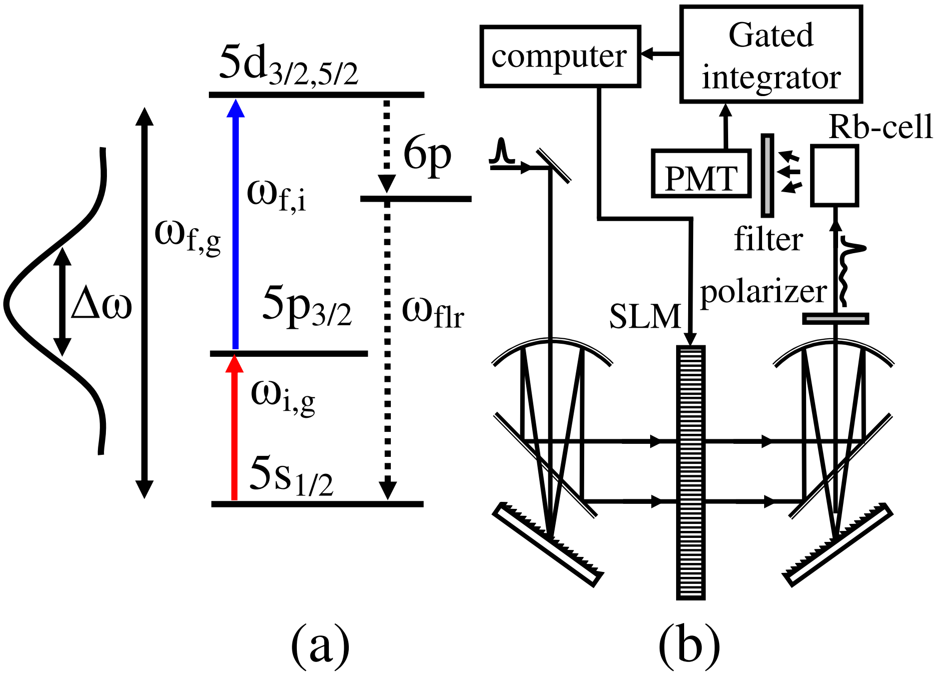

**Figure 4.1:** (a) Energy levels in atomic rubidium for the two-photon transitions $5s \rightarrow 5d$. The excited atoms spontaneously decay to the ground state, emitting ≈ 420 nm photons. (b) The experimental setup consists of a pulse shaper in 4f-geometry with a programmable SLM located in the Fourier plane. A polarizer is used, since amplitude modulation by the SLM is performed by a polarization retardation. The influence of the modulated femtosecond pulses is monitored with a PMT.

## 4.2 Experiment

The frequency-resolved influence of reshaped femtosecond pulses by absorption is studied in the three-level system of atomic rubidium, see Fig. 4.1(a). The resonant transitions from $5s \rightarrow 5p$ and $5p \rightarrow 5d$ correspond with transition wavelengths of $\lambda_{i,g} = 780.2$ nm and $\lambda_{f,i} = 776.2$ nm.

A Spectra Physics 1 kHz regeneratively amplified Ti:Sapphire femtosecond laser system provides 100 fs pulses of $600\mu J$. The central wavelength is tuned to $\lambda_c = 778.2$ nm ($\omega_c = \omega_{f,g}/2$) and the bandwidth encompasses the two transition wavelengths. After passing through a pulse shaper, the beam is sent into a 20 mm cell at room temperature containing atomic rubidium vapor.

The pulse shaper is constructed in a 4f-geometry, see Fig. 4.1(b), following Präkelt *et al*[126]. The gratings have 1200 grooves/mm and we use 300 mm cylindrical mirrors. The active elements are arranged in a combination of two 320-pixel spatial light modulators (LC-SLM, manufacturer), which are able to perform simultaneously and independently amplitude and phase modulation. The LC-SLM is located in the Fourier plane of the pulse shaper. The active area of the one-dimensional liquid crystals (LC) is 20x20 $mm^2$ and each pixel is 100 $\mu m$ wide. The resolution of the shaper is 126 GHz/pixel. Phase and amplitude profiles are programmed in the spatial light modulator (LC-SLM) with the position of the absorption line, $\omega_0$, linewidth $\gamma$, and strength $\alpha_0 l$ as parameters. The position of each modulation mask $\omega_0$, is scanned through the spectrum of the femtosecond pulse in step sizes of one pixel. Due to the finite pixel width in the LC-SLM the amplitude and phase profiles are discrete.

We will see transients appearing in front of the main pulse in case of applying an amplitude and phase modulation. These transients seem to appear at 'negative' times. However, a pulse shaper has a time window $\Delta t$, which is inversely proportional to the resolving power of the pulse shaper and is approximately 8 ps in our setup[112]. Centered around the arrival time of a transform limited pulse (TL) at $t_0$, the temporal intensity can be displaced within the time window and a transient can appear in front of the pulse at negative time. The pulse shaper is aligned for zero dispersion and a polarizer before the Rb-cell selects only the horizontal plane, since amplitude modulation by the LC-SLM is performed by a polarization retardation.

The 5d population in Rb is quantified by measuring the fluorescence at $\approx 422$ nm, due to spontaneous decay to the ground state via the 6p level. A photo multiplier tube (PMT) equipped with a narrow band filter is attached to a gated integrator and computer for recording and storage. The collected signal reflects the response over the entire beam profile.

## 4.3 Theory

### 4.3.1 Three-level system

Population transfer in the three-level system occurs whenever the sum of each photon pair within the pulse frequency distribution equals the energy difference between the ground and final state. The final state amplitude $a_f^{(2)}$, is given in a perturbative picture by[62]:

$$a_f^{(2)} \approx -\frac{1}{i\hbar^2}\mu_{f,i}\mu_{i,g}\Bigg[i\pi\tilde{E}(\omega_{i,g})\tilde{E}(\omega_{f,g}-\omega_{i,g}) + \wp\int_{-\infty}^{\infty}\frac{\tilde{E}(\omega)\tilde{E}(\omega_{f,g}-\omega)}{\omega-\omega_{i,g}}d\omega\Bigg], \tag{4.1}$$

where $g$, $i$, and $f$ label the ground, intermediate and final states. $\wp$ is de principle value of Cauchy. $\omega_{i,g}$ and $\omega_{f,i} = \omega_{f,g} - \omega_{i,g}$ are the resonant $5s \rightarrow 5p$ and $5p \rightarrow 5d$ transition frequencies. $\tilde{E}(\omega)$ is the Fourier transform of the electric field. It is expected that shaping of the pulses will have the most effect when amplitude and/or phase modulation occur around the two resonant transitions. The off-resonant contribution is inversely proportional to the detuning from resonance $\omega - \omega_{i,g}$, while the resonant contribution solely depends on $\tilde{E}(\omega_{i,g})$ and $\tilde{E}(\omega_{f,i})$[62].

From the above, an intuitive insight emerges from perturbation theory on the coherent excitation. Dudovich *et al.* realized that the off-resonant TPA amplitude can be enhanced significantly using a $\pi/2$ step phase mask at frequencies between the two resonances to ensure that the integrant is positive for all $\omega$. They showed that the two-photon absorption process (TPA) in the three-level rubidium atom could be enhanced by a factor of 7. The same mask, positioned elsewhere in the frequency spectrum of the pulses, could turn off the TPA process completely.

The dynamics of the three-level system excited by coherent radiation from a laser can be described as usual by the Schrödinger equation. The time-evolution of the state probabilities $P_n(t) = |C_n(t)|^2$ is described by the interaction Hamiltonian and reads:

$$i\hbar \begin{pmatrix} \dot{C}_g(t) \\ \dot{C}_i(t) \\ \dot{C}_f(t) \end{pmatrix} = \begin{pmatrix} 0 & \Omega_{i,g}(t) & 0 \\ \Omega_{g,i}(t) & \Delta_{i,g} & \Omega_{f,i}(t) \\ 0 & \Omega_{i,f}(t) & \Delta_{f,i} \end{pmatrix} \begin{pmatrix} C_g(t) \\ C_i(t) \\ C_f(t) \end{pmatrix}, \tag{4.2}$$

$\Delta_{i,g} = |\omega_{i,g} - \omega_c|$ is the difference between the carrier frequency and the first excitation energy. $\Delta_{f,i} = |\omega_{f,g} - 2\omega_c| = 0$, as the carrier frequency $\omega_c$ is resonant with the two-photon energy in our experiment. As usual, the rotating wave approximation (RWA) has been applied.

The interaction electric field $E(t)$ of a laser pulse is represented by

$$\varepsilon(t) = \varepsilon_0(t) cos(\omega_c t), \tag{4.3}$$

where $\varepsilon_0(t)$ is the temporal envelope of the femtosecond pulse. The strength of the light-matter interaction in Eq. (4.2) is given by the Rabi frequency $\Omega_{n,m}(t) = \varepsilon_0(t)\mu_{n,m}/2\hbar$, with $\mu_{n,m}$ the transition dipole moments.

We use in the calculations as well as in the experiment 100 fs Gaussian shaped pulses with a carrier frequency of $\omega_c = \omega_{f,g}/2$, corresponding to $\lambda_c = 778.2$ nm. The transition wavelengths are $\lambda_{i,g} = 780.2$ nm and $\lambda_{f,i} = 776.2$ nm with transition dipole moments $\mu_{i,g} = 5.87$ atomic units (a.u.) and $\mu_{f,i} = 1.77$ a.u.

The problem is solved numerically with time steps of 10 fs and the following initial conditions; $C_g(0) = 1, C_i(0) = 0$ and $C_f(0) = 0$. We are mostly interested in the excited $5d$ final state population $P \equiv |C_f(\infty)|^2$ long after the pulse. In the first part, time resolved solutions use the weak field limit taking $\Omega_{i,g} = 10^8$ rad/s, representing the weak field regime as $|\Omega_{i,g}| \ll |\Delta_{i,g}|$ (($\approx 10^{12}$ rad/s)). In the following, we present solutions both using the perturbative asymptotic solution of Eq. (4.1) as well as the asymptotic time-dependent solutions of Eq. (4.2).

### 4.3.2 Pulse propagation

Here we describe the effect of absorbing a narrow range of frequencies from a pulse distribution as in a gas or filter. Absorption is a linear combination of an amplitude and phase function and is given by the Kramers-Kronig dispersion relation through the complex susceptibility $\chi(\omega)$, which reads:

$$\chi(\omega) = (N_i - N_f)\frac{e^2}{2\varepsilon_0 m\omega_0} \times \frac{1}{\omega - \omega_0 - i\gamma}, \tag{4.4}$$

where $N_i$ and $N_f$ are the amount of atoms in the initial and final state before excitation. $\varepsilon_0$, m, $\omega_0$ and $\gamma$ are the permittivity of vacuum, the electron mass, the central absorption frequency and the half width half maximum (HWHM) of the Lorentzian absorption line, respectively.

From the complex susceptibility $\chi(\omega)$ follows the complex refractive index as

$$\eta(\omega) = \eta(\omega)' - i\kappa(\omega) \quad = \quad \sqrt{1 + \chi(\omega)}, \tag{4.5}$$

with $\eta(\omega)'$ being the refractive index and with $\kappa(\omega)$ related to the extinction coefficient $\alpha$ by

$$\alpha(\omega) = \frac{\omega}{c}\kappa(\omega). \tag{4.6}$$

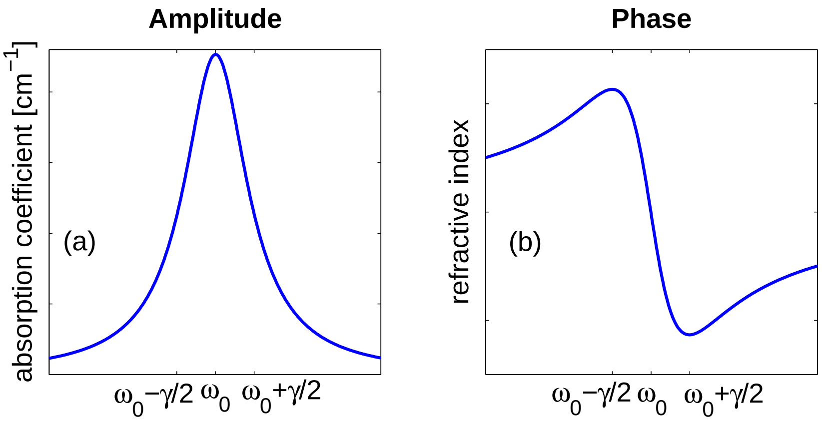

**Figure 4.2:** (a) The real and (b) imaginary part of the frequency-dependent complex refractive index $\eta(\omega)'$ (Eq. (4.4)).

Figure 4.2 depicts both components of the complex refractive index using Eq. (4.5). A propagating plane wave affected by absorption can thus be written as

$$\tilde{E}(\omega, l) = \tilde{E}(\omega) e^{-\alpha(\omega) l} e^{-i(\eta(\omega)'-1)\omega l/c}, \tag{4.7}$$

where $l$ is the propagation length through the absorbing medium and $c$ the speed of light. The absorption and dispersion profiles are parameterized by:

$$\alpha(\omega) = \alpha_0 \frac{\gamma^2}{\gamma^2 + (\omega_0 - \omega)^2}, \tag{4.8}$$

and

$$\eta(\omega)'\omega/c = \alpha_0 \frac{\gamma(\omega_0 - \omega)}{\gamma^2 + (\omega_0 - \omega)^2}, \tag{4.9}$$

where $\alpha_0$ determines the strength of the interaction.

In computational studies and in present day experiments, amplitude and phase functions can also be applied separately. The Fourier transform of $\tilde{E}(\omega, l)$ provides the time-dependent electric fields $\varepsilon(t)$, see Fig. 4.3. A first observation shows that semi-monochromatic transient electric fields arise around the main pulse. Reshaped pulses by absorption (Fig. 4.3c) have only a post-transient, due to causality, which is out-of-phase with the main pulse. Only power absorption or dispersion seems to lift causality, as pre-transients appear (Fig. 4.3(a) and (b)). Amplitude modulation results in a symmetric pulse profile with transient electric fields being out-of-phase with the main pulse, while phase modulation gives an asymmetric pulse profile with a phase-matched pre-transient and an out-of-phase post-transient. The transient electric fields have a duration $\tau$ inversely proportional to the FWHM of the line width $(1/e^2)$ with

$$\tau = \frac{1}{2}\gamma^{-1}. \tag{4.10}$$

We note that the transient carrier frequency is a difference frequency $|\omega_0 - \omega_c|$, while the rapid oscillating sum-frequency and the pulse carrier frequency $\omega_c$ is removed in the rotating wave approximation (RWA). In all cases, the main pulse structure remains nearly the same with a slightly reduced electric field strength.

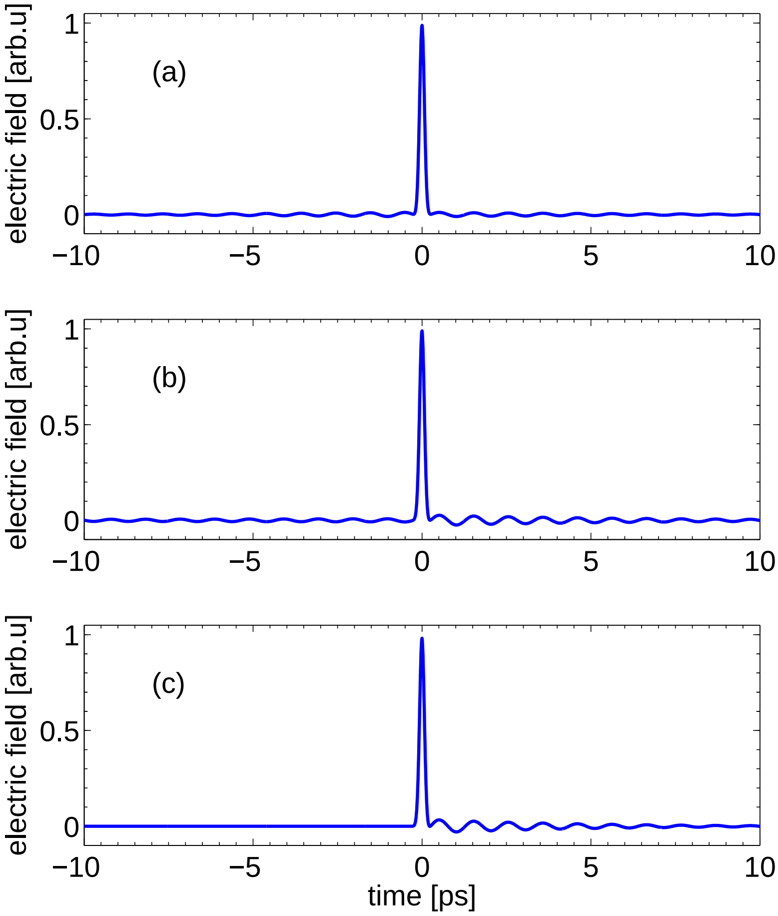

**Figure 4.3:** Electric fields $\varepsilon(t)$ of reshaped femtosecond pulses by the Kramers-Kronig dispersion functions (Eq. (4.5)), $\gamma = 100$ GHz, $\alpha_0 l = 2.3$. (a) amplitude, (b) phase and (c) absorption. Semi-monochromatic transients arise around the main pulse with $\approx 5$ ps decay time (Eq. (4.10)) and carrier frequencies equal to the difference frequency $|\omega_c - \omega_0|$.

One can appreciate that the sum of amplitude Fig. 4.3(a) and phase modulation 4.3(b) closely resembles the result of reshaping using absorption Fig. 4.3(c). The pre-transient is reduced significantly, while the post-transient is increased. In the remainder, we assume no decoherence effects due to collisions or Doppler broadening and the absorption profile is purely Lorentzian. The finite pixel width in the spatial light modulators force us to use line widths larger than atomic absorption lines in gases.

## 4.4 Results and discussion

We investigate the influence of shaped femtosecond pulses by narrow band amplitude (Fig. 4.3(a)), phase (Fig. 4.3(b)) and absorption (Fig. 4.3(c)) modulation on the two-photon excitation in the three-level atomic system of rubidium. The used absorption parameters are $\gamma = 100$ GHz and $\alpha_0 l = 2.3$, implying an extinction of 90% at the central frequency $\omega_0$.

We accompany measurements of the 5d-state population with calculations both time-dependent and time-independent. The time-independent calculations Eq. (4.1) resemble the experimental conditions and include the discretization of the modulation mask. In the remainder of this paper, we will focus on the final 5d-state population $|C_f(t)|^2$. We discuss the time-evolution during the pulse for the two central mask positions $\omega_0 = \omega_{i,g}$ and $\omega_0 = \omega_{f,i}$.

In Fig. 4.4 the experimental (solid) and calculated (dashed) TPA signal are shown as function of the central position of the amplitude function (Fig. 4.2). A transform limited (TL) pulse gives a TPA signal of 1. The experimental results reveal a significant enhancement around the two resonances and a significant reduction at the two transitions frequencies ($\lambda_{i,g} = 780.2$ nm and $\lambda_{f,i} = 776.2$ nm). The reduction reflects the intuitive picture that both resonant photons are needed in the TPA process. The calculations take into account the experimental discretization and resolution. The inset shows the result of both Eq. (4.1) and the asymptotic values of a time-dependent calculation without discretization. The discrete nature of the modulation does not have a large effect on the results of the simulations. Experimentally, we observe large enhancement around the two resonances. We will return to the discrepancies between our model calculations and the experimental result below. In Fig. 4.5 we present the time-evolution of the 5d-state population in the TPA process for an amplitude modulated femtosecond pulse for two positions of $\omega_0$. With the mask at $\omega_0 = \omega_{i,g}$ one observes a single step in the population due to the femtosecond pulse. The small oscillations reflect the non-resonant excitation at $\omega = \omega_{f,i}$ by the post-transient. The effect of the pre-transient can be appreciated from the intermediate 5p-state population (inset in Fig. 4.5). A quadratic increase is observed before the main pulse. In accord with the $\pi$-shift of the pre-transient, the main pulse initially depletes the 5p-state. This seemingly small reduction of the 5p-state population is the reason of the small TPA signal. With the mask at $\omega_0 = \omega_{f,i}$, one observes that the post-transient in spite of its small energy reduces the final state population by almost a factor of two. This resembles a pump-dump sequence. The important observation is that because of the coherent interactions, transients with very little energy have very large influence on the population transfer.

Figure 4.6 show the spectrally resolved TPA signal for a pulse modulated by the phase function (Fig. 4.2). Non-intuitively, we observe a sharp increase in the TPA signal with the mask at the 5s-5p resonance. The increase equals 115% at $\lambda_{i,g}$ and the decrease equals 45% at $\lambda_{f,i}$. This experimental result is well reproduced by the simulations, although also here, the coherent effects seem to be larger than calculated around $\lambda_{i,g}$ and $\lambda_{f,i}$. The inset shows that the discrete nature of our phase mask has a small influence.

The time-evolution of the final state population $|C_f|^2$ in Fig. 4.7 illustrate the cause of the enhanced population transfer in comparison with a TL pulse. The phase-matched pre-transient at $\omega_{i,g}$ (dashed) will transfer population to the intermediate 5p-state, which will be enhanced further by the main pulse. The out-of-phase post-transient can be largely ignored since it only connects the ground and intermediate states. A phase modulation of the femtosecond pulse at $\omega_{f,i}$ (dotted) creates a pre-transient, which can be neglected as no population is present in the intermediate state.

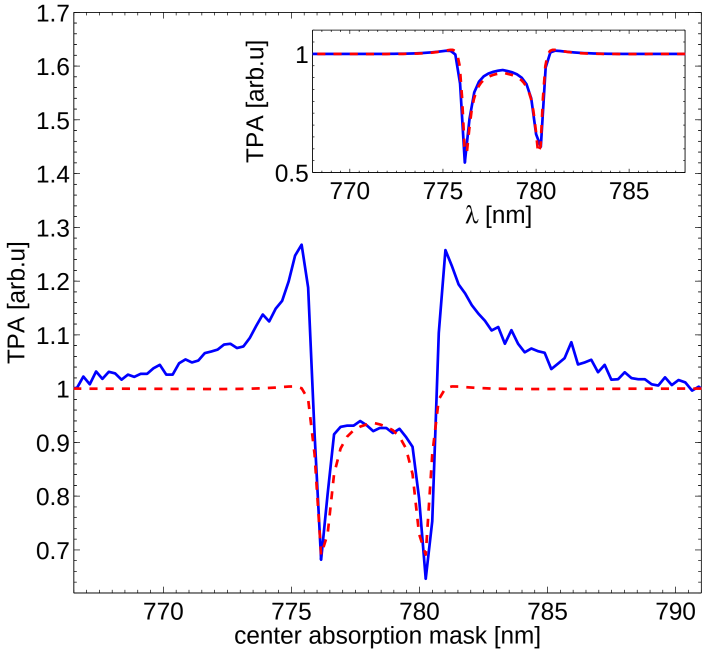

**Figure 4.4:** The experimental (solid) and the simulated (dashed) frequency-resolved TPA signal for amplitude modulated femtosecond pulses according to the Kramers-Kronig dispersion function ($\gamma = 100$ GHz, $\alpha_0 l = 2.3$). The inset shows the time-independent and the time-dependent calculations and mean to highlight the frequency-resolved TPA signal without discretization.

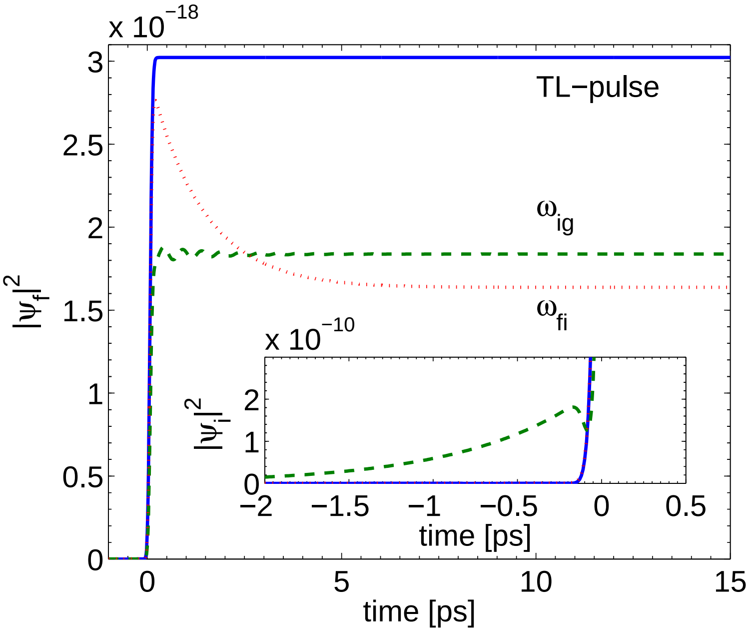

**Figure 4.5:** The time-evolution of the 5d-state population, $|\psi_f|^2$, for TL-pulses (solid) and amplitude modulated femtosecond pulses ($\gamma = 100$ GHz, $\alpha_0 l = 2.3$) with central mask positions $\omega_0 = \omega_{i,g}$ (dashed) and $\omega_0 = \omega_{f,i}$ (dotted). The inset shows the time-evolution of the 5p-state population $|\psi_i|^2$.

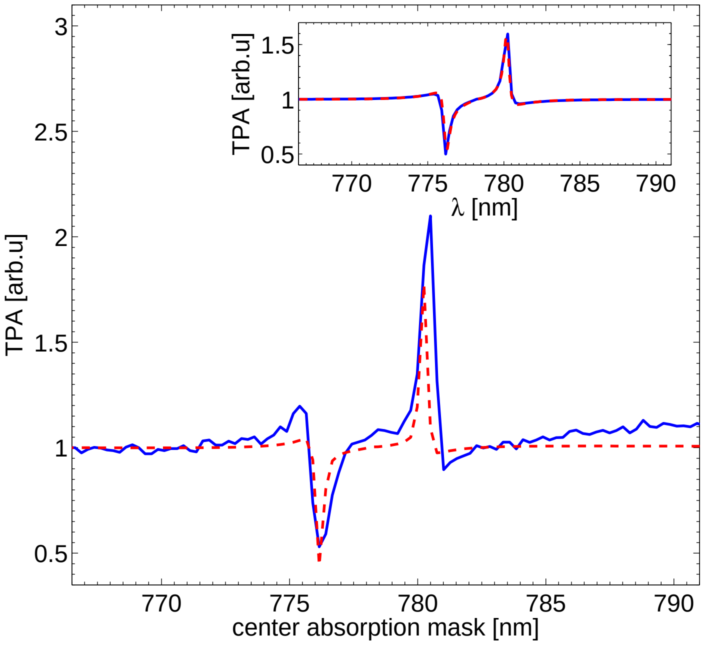

**Figure 4.6:** The experimental (solid) and the simulated (dashed) frequency-resolved TPA signal for phase modulated femtosecond pulses according to the Kramers-Kronig dispersion function ($\gamma = 100$ GHz, $\alpha_0 l = 2.3$). The inset shows the time-independent and the time-dependent calculations and mean to highlight the frequency-resolved TPA signal without discretization.

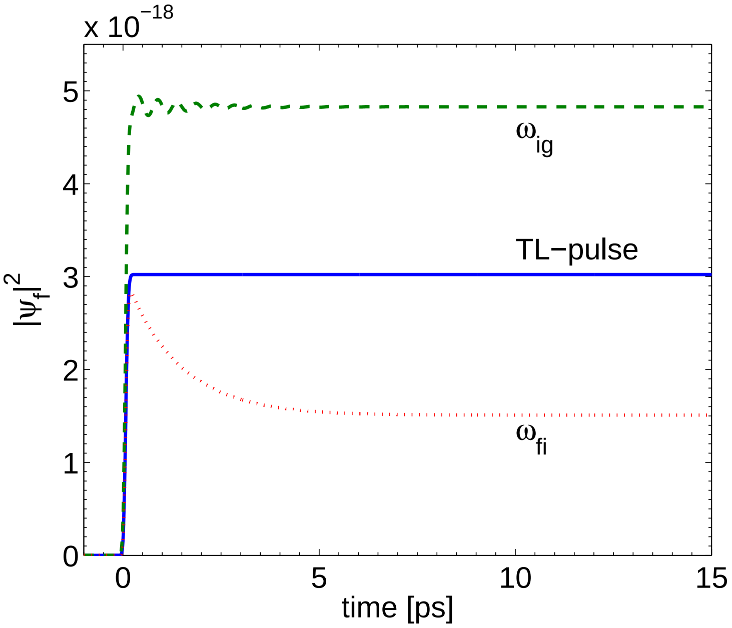

**Figure 4.7:** The time-evolution of the 5d-state population, $|\psi_f|^2$, for a TL-pulse (solid) and a phase modulated femtosecond pulse ($\gamma = 100$ GHz, $\alpha_0 = 2.3$) with central mask positions $\omega_0 = \omega_{i,g}$ (dashed) and $\omega_0 = \omega_{f,i}$ (dotted).

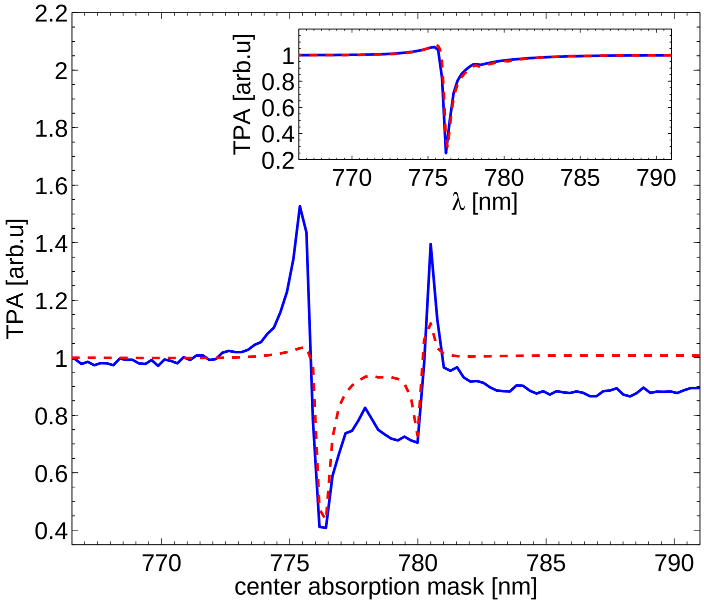

**Figure 4.8:** The experimental (solid) and the simulated (dashed) frequency-resolved TPA signal for absorption modulated femtosecond pulses according to the Kramers-Kronig dispersion functions ($\gamma = 100$ GHz, $\alpha_0 l = 2.3$). The inset shows the time-independent and the time-dependent calculations and mean to highlight the frequency-resolved TPA signal without discretization.

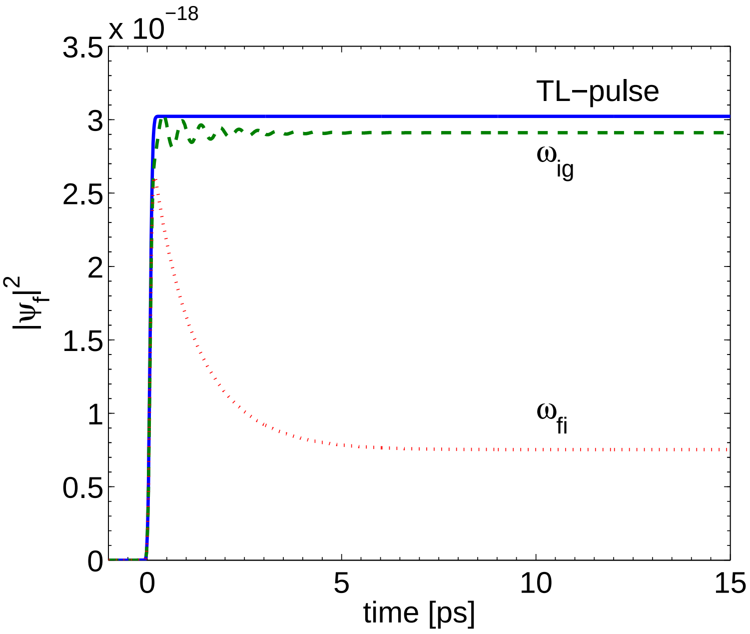

**Figure 4.9:** The time-evolution of the 5d-state population, $|\psi_f|^2$, for a TL-pulse and an absorption modulated femtosecond pulse ($\gamma = 100$ GHz, $\alpha_0 = 2.3$) with central mask positions $\omega_0 = \omega_{i,g}$ (dashed) and $\omega_0 = \omega_{f,i}$ (dotted).

The main pulse redistributes almost as much population to the final state as a TL pulse. However, the $\pi$-shifted post-transient de-excites the final state.

Finally, we will consider the situation in which amplitude and phase modulation are coupled obeying the Kramers-Kronig relations (Eq. (4.4)). Figure 4.8 shows the spectrally resolved influence of an absorption modulated femtosecond pulse on the final state population. Again, large effects are observed only around the transition frequencies $\omega_{f,i}$ and $\omega_{f,i}$.

In agreement with the previous results, around the resonances the TPA signal reacts more strongly on the pulse shaping than the calculations predict. Also in between the two resonances, the experiment is more sensitive to changes than the calculations. However, qualitatively, the simulation resembles our observations closely. In this case, the inset depicts that the discrete nature of the phase and amplitude function has a large effect. Also that the TPA is nearly unchanged when absorbing $\omega_{i,g}$. This can be better understood in the pump-dump picture.

The time-evolution of the 5d-state shows in Fig. 4.9 that in the absence of a pre-transient, the femtosecond pulse excites nearly the same amount of population to the 5d-state, whether or not absorption takes place. With the mask at $\omega_{f,i}$, the small energy out-of-phase post-transient depletes the 5d-state. When $\omega_0 = \omega_{i,g}$ the post-transition does not change the final state population and for an observer the fluorescence intensity remains unchanged.

As mentioned before, amplitude modulation and phase modulation are approximately additive when looking at the resulting time-dependent pulses in Fig. 4.3. In this research, we also found that the TPA signals in the three different situations are connected in a simple but highly non-intuitive manner. Comparing the insets in the Fig. 4.4, 4.6 and 4.8 one can appreciate that the following equality holds:

$$TPA(amplitude) \times TPA(phase) \approx TPA(absorption) \times TPA(TL). \qquad (4.11)$$

Fig. 4.10 shows the equality in the case of the calculations as well as the agreement in the experiments. We checked that this is not true on the level of amplitudes: $a_f^{amp} \times a_f^{ph} \neq a_f^{abs} \times a_f^{TL}$. Both sides of Eq. (4.11) display a remarkable agreement. Importantly, this comparison using the experimental results shows the consistency of our observations. We conclude that the two 320-pixel spatial light modulators have small extra affects which are not fully correctly modeled by taking step functions when going from pixel to pixel. Comparing our results with those by Dudovich *et al.*[124] reveals similarities. These authors showed that frequencies near the resonances could indeed enhance the TPA signal in Rb. We have also looked for other experimental reasons for a difference with the calculations. In ultrafast pulses the occurrence of chirp in the pulse can not always be prevented due to dispersion in many optical components. Numerically, we have looked at the effect of chirp on the TPA signal. Even up to a pulse elongation of a factor of 10, the effects on the form of the response on moving an amplitude profile through the spectrum are small. The absolute signal decreased significantly. Hence, we rule out (linear) chirp as an explanation of the difference between our calculations and observations. The above result shows that weak semi-monochromatic post-transients due to absorption, resonant with a transition in the Rb three-level system, significantly reduce the TPA signal. Beyond the perturbative limit when the main pulse is sufficiently strong, saturation can occur during the main pulse. Since saturation is accompanied with a phase change of the time-varying

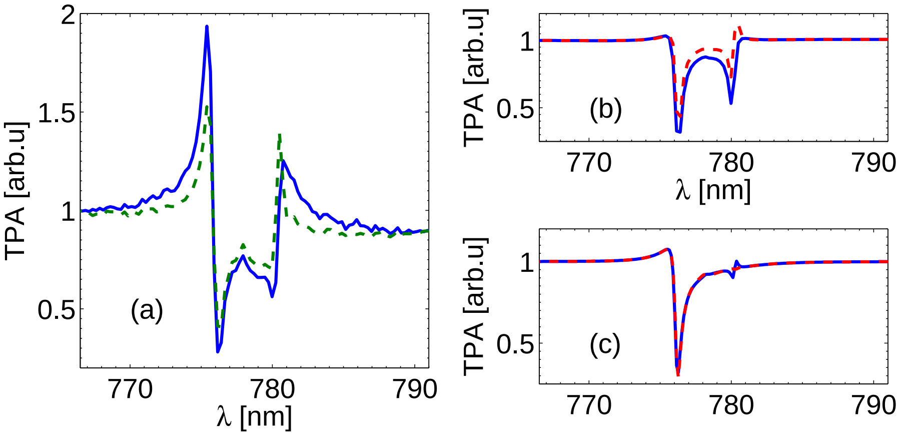

**Figure 4.10:** Comparison of the product of amplitude and phase modulated (solid) TPA signal with absorption modulated (dashed) TPA signal (Eq. (4.11)). (a) Experiment, (b) simulation with descretization, (c) simulation without discretization.

coefficients $C_n(t)$, an out-of phase post-transient can be suddenly phase-matched and can become an effective driving field for further coherent excitations.

We will present one computational example optimizing the excitation to the final 5d-state of rubidium using a single narrow band amplitude modulation with intensities that are in reach of present day amplified Ti-Sapphire laser. Figure 4.11 shows the time evolution of the 5d-state population $|C_f|^2$ for the reshaped femtosecond pulse (dashed) having an optimized absorption profile at $\omega_0 = \omega_{f,i}$. We adjust the linewidth and the absorption strength. As a result, the shaped femtosecond pulse enhance the TPA rate with a factor 8.8. In the end, approximately 97% of the population is transferred to the final state at a Rabi frequency of $\Omega_{i,g} = 4.1$ THz. The linewidth was taken to be 4.1 GHz, while the resonant absorption coefficient $\alpha_0 l$ is increased to 2.57. As the inset shows, within the time duration of the main pulse an oscillation, similar to half a Rabi-cycle, is covered and the post-transient is suddenly phase-match with the time-varying coefficient $C_f(t)$. Population is transferred to the final state in the presence of the transient electric field with nearly complete population inversion. We believe that this solution is certainly not the only one. The successful solutions not only have to increase the 5d population, but prevent population trapping at the ground and intermediate state. Also an optimized phase modulated femtosecond pulse at $\omega_0 = \omega_{f,i}$ holds the ability for nearly complete inversion and transfer approximately 98% to the final 5d-state.

Clearly semi-monochromatic transients can be used to populate and depopulate excited states in multi-level systems. The reshaped pulses by narrow band absorption have similarities with self-induced transparency i.e. lossless propagation in normally absorbing media. The uses of programmable spatial light modulators may result in multi-resonance self induced transparency. Future studies may involve searching for state specific excitation in multi-photon processes by combining complex structures with selective narrow band absorption. In the present research only amplitude and phase modulation was used. Polarization modulation enables manipulation of vectorial properties. For example, Dudovich *et al.*[127] has applied polarization masks in

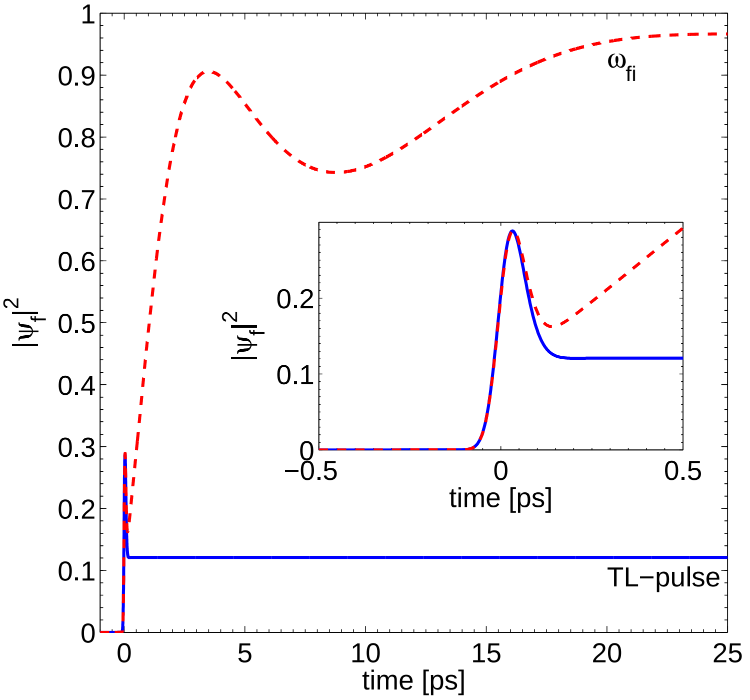

**Figure 4.11:** The time-evolution of the 5d-population for a TL-pulse (solid) and an optimized absorption modulated femtosecond (dahsed) ($\gamma$ = 4.1 GHz, $\alpha_0$ = 2.57) at a Rabi frequency of 4.1 THz. In the presence of the main pulse half a Rabi cycle is covered and suddenly the post-transient is phase-match with 5d-state population. The semi-monochromatic transient efficiently populates the final state with nearly complete population inversion.

the presently used rubidium system, obtaining angular momentum control. It has been also recently demonstrated that with help of circular polarized laser pulses one can excite and control spin precessions in magnetically ordered materials[128] and even reverse magnetization on a subpicosecond time scale[129]. Obviously, many opportunities exist to control the coherent aspects of light in the interaction with quantized multi-level systems.

## 4.5 Conclusions

We have demonstrated the ability to use absorption reshaped femtosecond pulses to manipulate the two-photon absorption in rubidium. The amplitude and phase profile accompanied with absorption are also applied separately. Overall, good agreement is observed between theoretical and the experimental dependency of the two-photon absorption signal on narrow band phase and amplitude modulation. Narrow band frequency modulation within the pulse distribution is thus well understood and the reshaped pulses have large effects in resonant multi-photon process.

Our results illustrate that the largest effects mainly occur near the transition frequencies $\omega_{i,g}$ and $\omega_{f,i}$. Removing one of the two frequencies confirms the intuitive picture that both resonant photons are needed in the TPA process. The asymmetric phase function of absorption has the ability to enhance as well as decrease the two-photon absorption. When absorbing $\omega_{i,g}$, remarkably the final state population is little influenced. An intuitive insight emerges from perturbation theory on the coherent excitation using the photon picture. Quantum mechanical interference between resonant and off-resonant contribution change the outcome. In case of complex pulse shaping by absorption, the excitation process is better understood by the time-dependent picture of continuous electric fields. As a consequence of modulating a narrow band of frequencies within the pulse distribution, semi-monochromatic transients arise around the main pulse with small intensities. Induced electronic wave packets by the main pulse either being in phase or out-of-phase with the transient electric fields, causing transferred state population to be coherently pumped back to a lower state or pump further to an higher lying state. These semi-monochromatic transients are ideal driving electric fields to enhance or deplete state population.

It follows from the Kramers-Kronig dispersion relation that in absorption, amplitude and phase are coupled. Comparison of the absorption reshaped time structure reveals that the amplitude-only and phase-only reshaped temporal pulses are approximately additive. Also the TPA behavior in the three different situations are connected, in a rather simple, but in a not obvious manner. The TPA of absorption is well approximated by the product of the TPA signal for amplitude-only and phase-only. The good experimental agreement illustrates the consistency throughout the measured TPA signals. Numerically an optimal pulse has been designed, which takes advantage of Rabi-cycling during the main pulse. 97% of the population is transferred to the final state and the two-photon absorption is enhanced with a factor 8.8. Without any genetic optimization algorithm we are able to find an absorption reshaped femtosecond pulse which holds the ability for complete inversion.

## Acknowledgments

The authors would like to thank Ing. A.F. van Etteger for his technical support, and Prof. M.J.J. Vrakking for his stimulating discussions and computational support. This work is supported by the "Stichting Technische Wetenschappen (STW)", which is financially supported by the "Nederlandse Organisatie voor Wetenschappelijk Onderzoek (NWO)".

# CHAPTER 5

# A THz spectrometer based on a CsI prism

A terahertz (THz) spectrometer is demonstrated that is based on a 25 K cryogenically cooled cesium iodide prism using a bolometer as detector. We present the THz spectrum of short pulses from a large biased semiconductor irradiated with femtosecond pulses from a Ti:sapphire laser and calibrate the spectrum with the transmission spectra of frequency selective surface filters centered at 300 GHz and 600 GHz. In addition, the optical properties (absorption and dispersion) in the THz frequency range are reported for CsI, and also KBr and KCl for temperatures between 10 and 300K. These were obtained using THz time domain transmission spectroscopy using electro-optic sampling. The CsI prism spectrometer is sufficiently transparent from 0.2 to 1.1 THz ensuring an overall energy throughput exceeding 10 percent. The resolution equals about 100 GHz at 0.6 THz and 170 GHz at 0.3 THz.

Submitted to Journal of Optics A

## 5.1 Introduction

Terahertz (THz) spectroscopy is a rapidly growing field as new efficient and flexible sources are developed. In the THz region, also named the far infrared (FIR) part of the electromagnetic spectrum, low energy modes can be found in polymers, and large organic molecules and biomolecules[130,131]. Also electron and exciton transport properties in semiconductors, semiconducting polymers, solar cells and quantum dots are studied with THz radiation[132–135] THz radiation can be generated in the form of ultrashort pulses allowing to perform spectroscopy with high time resolution. Such THz pulses can be produced using rectification of optical femtosecond pulses in an appropriate crystal[136–138] or by charge-carrier generation and acceleration in a biased semi-conductor[13–17] also using femtosecond pulses. These THz pulses are typically a single half or full cycle of electromagnetic radiation[15,139]. As a consequence, the bandwidth of these FIR pulses spans several octaves. In THz time domain spectroscopy (TDS), the spectrum of the broadband pulse is analyzed over its full spectrum by sampling the electric field using time-delayed femtosecond probe pulses. At present, asynchronous optical sampling (AOS) TDS[140], employing two femtosecond lasers with slightly different repetition frequencies, allows scanning the temporal profile of a THz pulse already in less then a second. Single-shot measurements become possible using chirped femtosecond probe pulses in combination with multichannel detection using a spectrometer[141,142].

These techniques require complex instrumentation in combination with very sensitive detection. A robust instrument with variable spectral resolution would offer attractive possibilities. However, with radiation spanning more than one octave, grating-based spectrometers cannot be used. Prism spectrometers at FIR wavelengths are difficult to build, because of two effects; the dispersion is generally small and most materials absorb THz radiation. Nevertheless, we will demonstrate a prism spectrometer for the analysis of broad-band THz pulses using cesium iodide (CsI) as prism material. Although at present a movable bolometer is used, this spectrometer can in principle be converted into a single-shot device with an appropriate position-sensitive detector. The instrument is simple and fast, and its frequency resolution can be changed by choosing other alkali halide crystals. The wavelength resolution of our spectrometer is lower than what is generally achieved with TDS. In the frequency range above 6 THz, alkali halide crystals are being used extensively[143] as prism material and also as beam splitters, windows and fibers in the near-, mid-, and far-infrared[144]. Already in 1912, Rubens and Hertz discovered that the (mid-)infrared optical properties of alkali halide crystals depend on temperature[145]. Alkali halide crystals become more transparent for electromagnetic radiation at low temperatures. The lowest phonon mode in these crystals is at a few THz. At room temperature this fundamental lattice mode is thermally populated and FIR absorption events involve annihilation and creation of more than one phonon[146–150]. FIR properties of ionic crystals, for example of $CaF_2$, $SrF_2$, $BaF_2$, and $CdF_2$ have been measured experimentally and described theoretically[151]. For wavelengths below 15 micron the optical properties of many alkali halides are described in a review paper by Li[152]. In the case of CsI, recently THz-TDS has been used in reflection to determine absorption and dispersion[153]. As mentioned, we present a CsI prism spectrometer, the resolution and throughput of which we characterize by measuring broadband coherent THz radiation from a large-aperture biased GaAs semiconductor. We also present the absorption and dispersion of CsI between 0.2 and 1.17 THz using transmission THz-TDS. Since also other ionic crystals have excellent FIR optical properties and low absorption, we also provide the dielectric properties for KBr and KCl.

## 5.2 Theory

### 5.2.1 Optical properties of alkali halide crystals

In order to properly design the prism spectrometer, the absorption and refractive index of the alkali halide crystals CsI, KBr, and KCl were determined for temperatures between 10 K and room temperature. We used THz-TDS in direct transmission on 5 mm thick samples. The complex dielectric function, i.e. the combination of absorption and refractive index, is determined in THz-TDS by quantifying the electric fields of a sample pulse, $E_{sam}(t)$ and of a reference pulse, $E_{ref}(t)$. Both pulses are Fourier transformed (using the convention $E(t) \propto \exp(-2\pi i\nu t)$) into the frequency domain and we obtain the transmittance:

$$\tilde{\Gamma}(\nu) = \frac{\tilde{E}_{\mathrm{sam}}(\nu)}{\tilde{E}_{\mathrm{ref}}(\nu)}. \tag{5.1}$$

Inserting a sample with thickness $d$ will lead to an amplitude transmittance[2]

$$\tilde{\Gamma}(\nu) = e^{-\alpha(\nu)d/2} e^{2\pi i(n(\nu)-1)\nu d/c} \left[\frac{4n(\nu)}{([1+n(\nu)]^2}\right], \tag{5.2}$$

where c, $n(\nu)$ and $\alpha(\nu)$ are the speed of light, the refractive index and the intensity absorption coefficient, respectively. The last factor on the right represents reflection losses. Hence, the frequency-dependent refractive index can be determined by

$$n(\nu) = 1 + \frac{c}{2\pi\nu d} \arg\left(\tilde{\Gamma}(\nu)\right) \quad (\mathrm{mod}\ c/\nu d). \tag{5.3}$$

and the frequency-dependent intensity absorption coefficient, taking into account reflection losses, follows from:

$$\alpha(\nu) = -\frac{2}{d} \ln\left\{|\tilde{\Gamma}(\nu)| \frac{[1+n(\nu)]^2}{4n(\nu)}\right\}. \tag{5.4}$$

The refractive index may be represented by the Sellmeier equation, an empirical relationship between refractive index and wavelength for a particular transparent medium. The Sellmeier equation reads

$$n(\lambda)^2 = 1 + \lambda^2 \sum_{j=1}^{k} \frac{A_j}{\lambda^2 - B_j^2}, \tag{5.5}$$

where $A_j$ and $B_j$ are the Sellmeier coefficients, $\lambda$ is the wavelength in micrometers. The parameters, $B_j$, can be associated with absorption features. The dispersion,

$$\frac{dn}{d\lambda} = -\frac{\lambda}{n(\lambda)} \sum_{j=1}^{k} \frac{A_j B_j^2}{(\lambda^2 - B_j^2)^2}, \tag{5.6}$$

is largest for wavelengths close to an absorption band. As mentioned, we fix one of the $B$ parameters to the fundamental lattice absorption bands at 1.84 THz for CsI, 3.42 THz for KBr, and 4.26 THz for KCl, respectively[153,154]. CsI is expected to have the largest dispersion in the 0.2–1.17 THz range of the three materials under consideration.

### 5.2.2 Spectrometer design

The layout of the spectrometer is as shown in Fig. 5.1 and the inset depicts the geometry and dimensions of the prism. These dimensions of the prism determine the resolution of the spectrometer. The exit angle $\delta$ of the radiation from the prism surface is wavelength-dependent and is given by[2]

$$\delta(\lambda) = \sin^{-1}\left(\sin\gamma\sqrt{n(\lambda)^2 - \sin^2\alpha} - \sin\alpha\cos\gamma\right), \tag{5.7}$$

where $n(\lambda)$ is the refractive index of the prism material. In our spectrometer setup, the angle of incidence $\alpha$ at the prism surface and the prism apex angle $\gamma$ were optimized. To avoid reflection losses, both $\alpha$ and $\delta$ are chosen close to the Brewster angle for the intended frequency range. We chose $\gamma = 39.5$ deg and $\alpha = 70$ deg, which corresponds to Brewster angles at both prism surfaces for $n = 2.74$ (at 1.2 THz). Across the frequency range from 0.2 to 1.2 THz, the exit angle varies over the range from approximately 44.5 to 66 deg. The resolution of the prism based-spectrometer is wavelength-dependent mainly because of the nonlinear dispersion across the frequency range. Obviously, wavelengths that are separated by less than the focus size cannot be resolved. A beam with a $1/e^2$-intensity radius $W$ is focused by a lens with focal length $f$ onto a diffraction-limited spot with a $1/e^2$-focus radius is $w = f\lambda/\pi W$. Using this $w$ as the minimum separation, we derive the wavelength resolving power

$$\frac{\lambda}{\Delta\lambda} = \pi W\left(\frac{d\delta}{d\lambda}\right). \tag{5.8}$$

The wavelength resolution improves when the beam diameter after the prism is large. On the other hand, a large prism gives extra absorption losses. The transmittance can be estimated using the absorption coefficient of the prism material. Assuming that the whole prism surface is illuminated, the transmittance is given by

$$T(\lambda) = \frac{1}{L\alpha(\lambda)}\left[1 - e^{-L\alpha(\lambda)}\right], \tag{5.9}$$

where $L$ is the length of the base of the prism (see Fig. 5.1). Apart from decreasing signal, absorption also affects the resolution. Because the radiation passing through the prism close to its base is attenuated more than the light passing through the apex, the prism effectively acts as a slit that reduces the beam diameter $W$ in Eq. (5.8). Thereby the resolution degrades. The relation between the transmittance $T(\lambda)$ and the decrease in resolution is non-trivial. If the beam is Gaussian in shape and significantly smaller than the prism, then the beam size is not affected by this absorption process. The beam is only shifted and attenuated.

In the case of a homogeneous illumination of the whole prism, the reduction of the width of the beam can not easily be quantified. The results show that the reduction

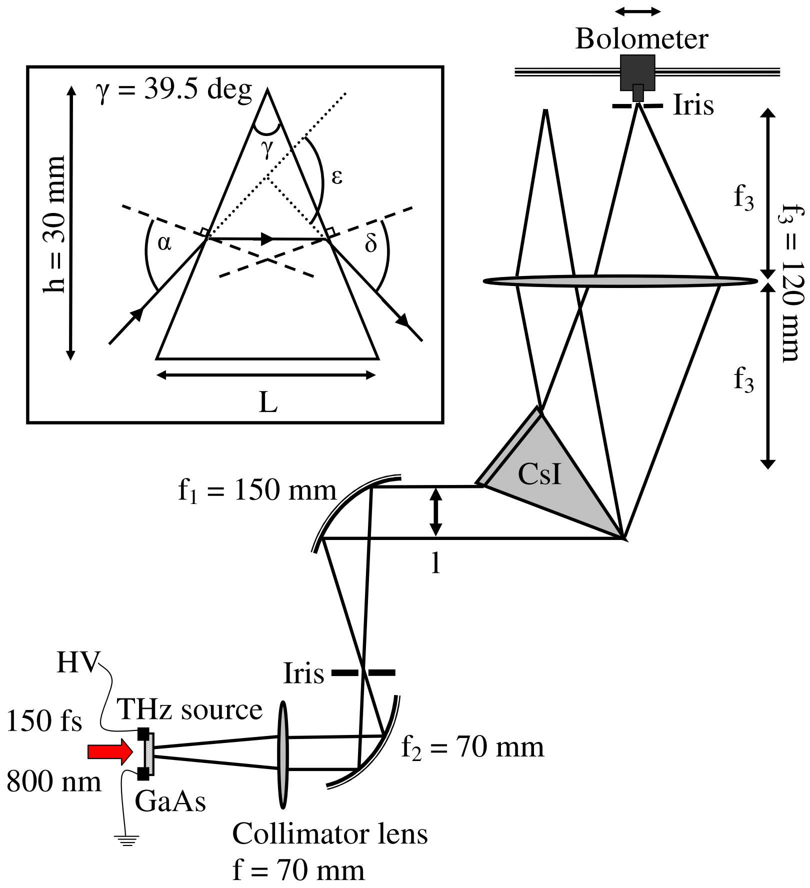

**Figure 5.1:** Emitted THz radiation from a large biased semi-conductor is collimated into a parallel beam and is spatially filtered with an iris in between the two off-axis parabolic mirrors (OPM). A dispersive cryogenic cooled CsI prism separate the different frequencies and are imaged by a lens. A moveable Bolometer records the spectral distribution of the THz source. The inset shows the prism arrangement. The inset shows the geometry and dimension of the prism.

in beam size is small. If the incoming beam diameter equals $l$, ignoring the effect of absorption, we find:

$$\frac{\lambda}{\Delta\lambda} = \frac{\pi l \cos\delta}{2\cos\alpha}\left(\frac{d\delta}{d\lambda}\right). \tag{5.10}$$

We can also express the resolution in the geometry of the prism: the height $h$, and the apex angle $\gamma$, the angle of incidence $\alpha$, and the observed wavelength dependent refractive index $n(\lambda)$ (see inset 5.1). The resolving power then becomes:

$$\frac{\lambda}{\Delta\lambda} = \frac{\pi h n(\lambda)\sin(\gamma/2)}{\sqrt{(n(\lambda)^2 - \sin^2(\alpha))}}\left(\frac{dn(\lambda)}{d\lambda}\right). \tag{5.11}$$

It is found that Eq. (5.11) is well approximated by using the following expression in which $n_{Br}$ is refractive index at Brewsters angle at our minimum deviation geometry.

$$\frac{\lambda}{\Delta\lambda} \approx \frac{\pi h}{n_{Br}}\left(\frac{dn(\lambda)}{d\lambda}\right). \tag{5.12}$$

## 5.3 Experiment

### 5.3.1 Optical properties of alkali halide crystals

The optical properties of the alkali halide crystals were analyzed with a conventional THz-TDS instrument[155]. The THz radiation is generated with optical rectification in a zinc telluride (ZnTe) crystal[15]. We use 150 fs pulses from a 1 kHz regeneratively amplified Ti-Sapphire laser centered around 800 nm. The resulting THz pulses are collimated and focused onto a sample using a pair of off-axis parabolic mirrors. Our alkali halide samples are housed in a closed-cycle helium cryostat (Air Products) for temperature control (10–300 K). The THz pulses are re-collimated and focused onto a ZnTe detection crystal using a second pair of paraboloidal mirrors. The electric field strength of the THz field is measured with electro-optical sampling[137] again using 150 fs probe pules from the regenerative amplifier. The delay $t$ between the THz and the probe pulse is mechanically scanned with a time resolution of 50 fs and the temporal profile of the detected THz field, $E_{\mathrm{THz}}(t)$, is obtained. The THz-TDS temporal profiles were obtained in a nitrogen atmosphere to prevent absorption by water and $CO_2$.

### 5.3.2 Spectrometer

Our THz prism spectrometer consists of a collimator with two parabolic mirrors of 70 mm and 150 mm as depicted in Fig. 5.1, resulting in a magnification factor of approximately 2. A 10 mm wide, biased, GaAs semiconductor is illuminated with 300 $\mu$J 150 fs pulses at 800 nm from a 1 kHz regeneratively amplified Ti:sapphire laser and is the source of pulsed THz radiation. An iris with an aperture of 3 mm is used for spatial filtering to obtain a single spot image for the second parabolic mirror. The expanded collimated THz beam propagates 150 mm and is then dispersed by the CsI prism. The refracted frequency components emerging from the prism are focused by a 120 mm TPX lens. The CsI prism was obtained from GB Group Inc., New York and the inset in Fig. 5.1 shows the geometry and dimension of the prism.

The temperature of the CsI prism is controlled with an Oxford Instruments liquid-helium cryostat equipped with TPX windows. The performance of our spectrometer is determined using a cryogenically cooled bolometer in the focal plane of the spectrometer. The aperture of the bolometer is 3 mm. The whole bolometer is mounted on a translation stage. The output signals are recorded with a lock-in amplifier. The CsI prism is cooled down to approximately 25 K. The spectrometer is calibrated with two frequency-selective surface (FSS) filters[156]. These bandpass filters are centered at 300 and 600 GHz with FWHM bandwidths of roughly 120 GHz at 300 GHz and 200 GHz at 600 GHz, respectively. Note that the FSS filters have a characteristic damping around the central frequency.

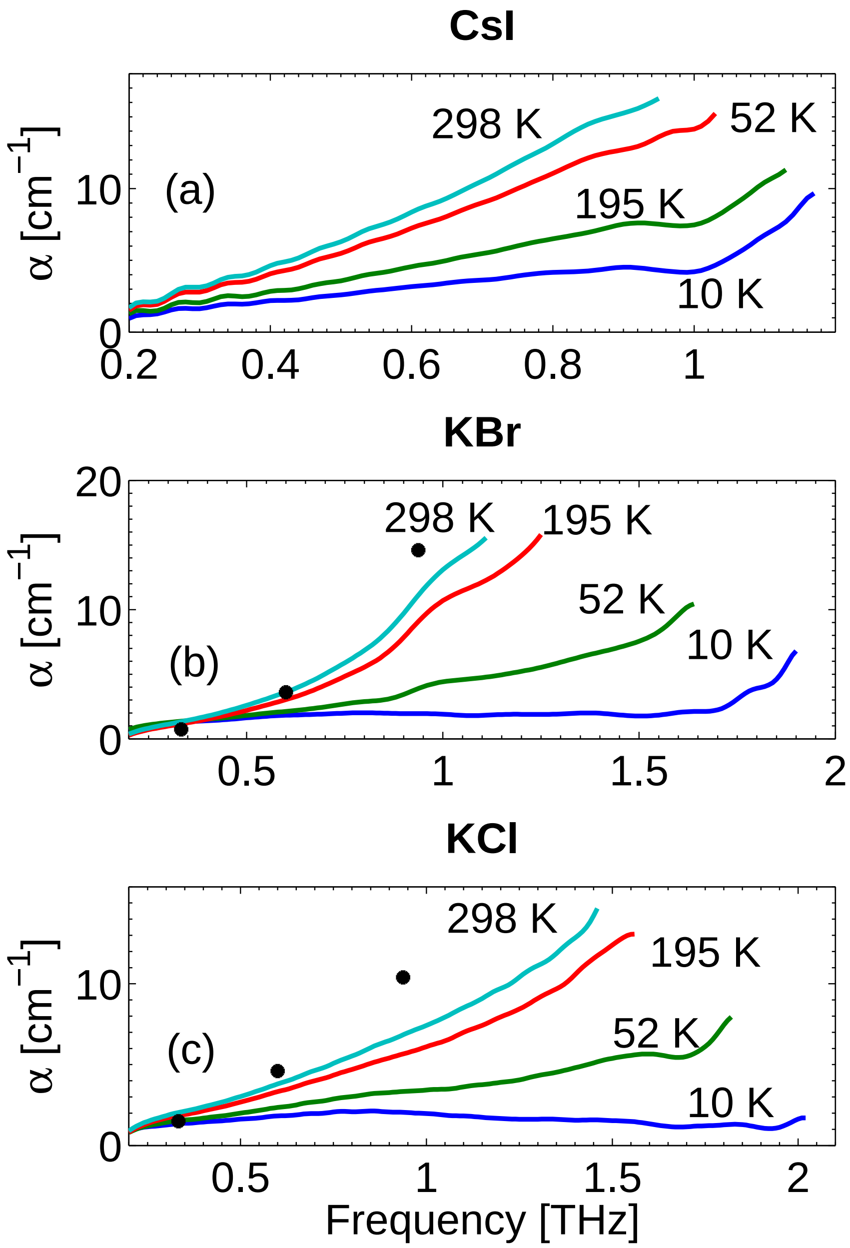

**Figure 5.2:** Absorption spectra for (a) CsI, (b) KBr, and (c) KCl at various temperatures. The markers (•) in (b) and (c) are reference data at 300 K from Stolen and Dransfeld[146]. Note the different frequency axes for the different materials. The absorption coefficients are defined as ln($T$).

## 5.4 Results and discussion

### 5.4.1 Optical properties of alkali halide crystals

Figure 5.2 contains the measured absorption spectra for temperatures between 10 K and room temperature in the frequency range from 0.2 THz (1.5 mm) to 2.0 THz (150 $\mu$m). The absorption of FIR radiation increases strongly with increasing temperature. The fundamental lattice mode becomes thermally populated and more phonons are available that couple with the incident radiation. The absorbance is seen to increase roughly proportional with temperature, also at low temperatures. Near 0.2 THz the absorbance seems to be independent of temperature.

Jepsen and Fischer[153] have measured the optical properties of CsI using THz-TDS in a reflection geometry. These authors concentrated on the strong absorption close to the fundamental lattice band. The much smaller absorption of interest for our prism spectrometer was not quantified. In the literature data can be found on the absorption by alkali halide materials. For example, absorption coefficients for KBr and KCl were reported by Stolen and Dransfeld[146] for wavelengths of 320, 500 and 900 $\mu m$ (10.7, 16.7 and 30 $cm^{-1}$) at 300 K using radiation from a mercury arc. In Fig. 5.2(b) and (c), these reference data are added. The agreement is reasonably good.

Differences among reported values can be found and may be attributed to differences in the purity of the used materials. In particular water as impurity and the adsorption of water on the crystal surface may affect observations in our frequency range[157–159]. We observe an increase in the absorbance towards higher frequencies, exceptions occur around 1.0 THz for CsI with a local minimum for temperatures below 100 K and for KBr and KCl above 1.0 THz. In the case of KBr, reports exist that show at low temperatures a smaller absorption than we find in our experiments around 500 GHz. Using a cryostat it is unlikely that adsorbed water contribute to our observations. Although a large amount of data exists below 50 $\mu$ from the 1960s and before, to the best of our knowledge, these are the first THz-TDS transmission measurements of alkali halide crystals on which is not easy to find reference data. The positions of the fundamental lattice bands are at 1.84 THz, 3.42 and 4.26 THz for CsI, KBr and KCl, respectively[153,154]. The proximity of the fundamental lattice bands to the THz regime is accompanied by significant absorption in the frequency range from 0.2 to 2.0 THz. The useful spectral window is smallest for the case of CsI (see Fig. 5.2). However, as we will explain below, CsI has the largest dispersion and is therefore the most useful material for a THz prism spectrometer around 1.0 THz.

Figure 5.3 shows the measured refractive indices as a function of frequency for the same temperatures as the absorption data. The data was fitted to the Sellmeier equation (Eq. (5.5)) with two terms, where we fixed one of the $B$ coefficients to the known phonon resonance frequency for each material. The Sellmeier equation accurately describes the experimental data within $\pm 10^{-3}$. The coefficients for all three materials are given in the Tables I, II, and III, respectively. The resolution of a prism spectrometer is dominated by the dispersion, $dn/d\lambda$, of the material. Below 100 K, the refractive index increases with 0.29 across the frequency range from 0.2 to 1.17 THz for CsI, while this increase is only 0.14 for KBr and 0.11 for KCl (see Fig. 5.3). In spite of the significantly higher absorption in CsI than in KCl and in KBr, CsI is the best choice as prism material owing to its large dispersion.

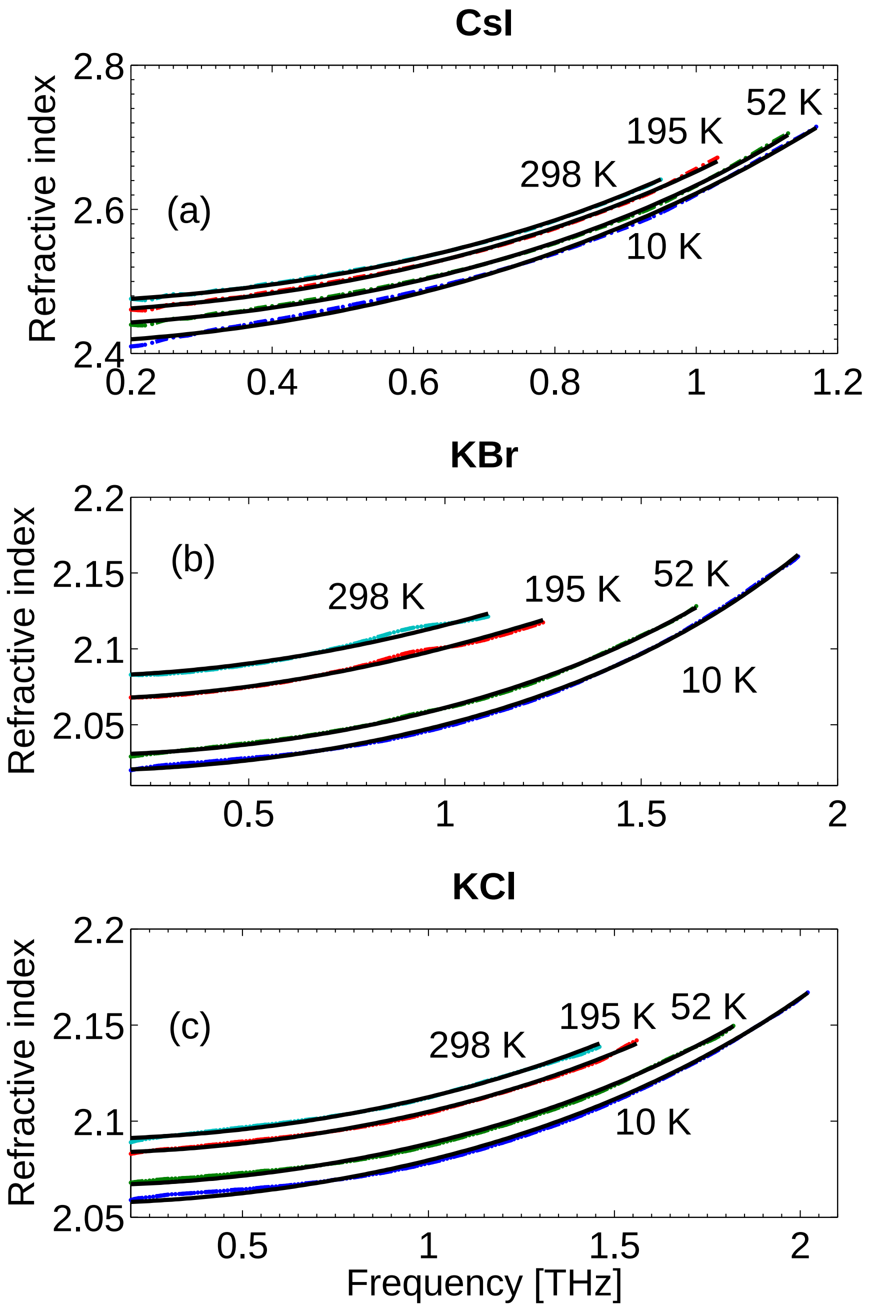

**Figure 5.3:** The experimental frequency-dependent refractive index $n(\nu)$ (dotted) for (a) CsI, (b) KBr, and (c) KCl at temperatures of 10, 52, 195 and 298 K. Each refractive index is fitted using a two-term Sellmeier representation (solid), Eq. (5.5) and is tabulated in table 5.1, 5.2 and 5.3. Due to phonon resonances of 1.84 THz (CsI), 3.42 THz (KBr), and 4.26 THz (KCl), the index of refraction increases steeply towards higher frequencies. Note the different frequency domains with the different materials.

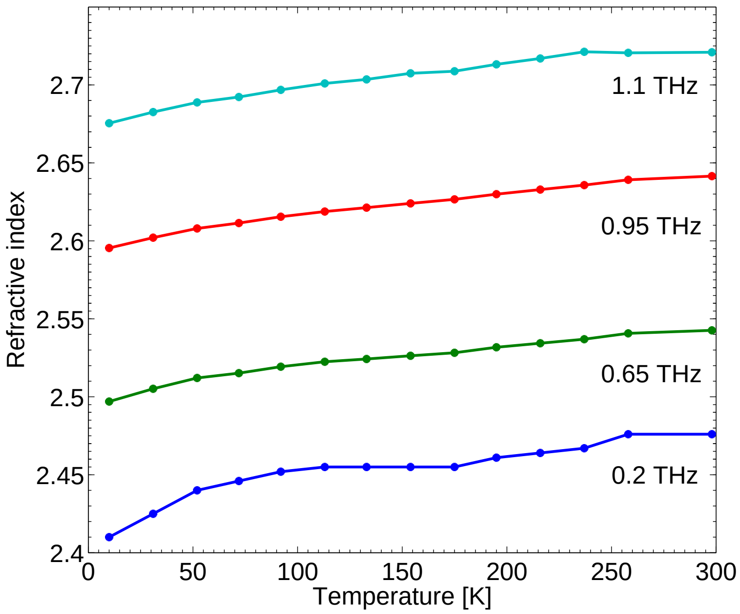

**Figure 5.4:** The temperature-dependent index of refraction for CsI at selected frequencies.

The temperature dependence of the refractive index of CsI is shown in Fig. 5.4(b) at selected frequencies. At 0.2 THz and at temperatures below 75 K, the refractive index changes significantly with temperature. The observed temperature sensitivity of the CsI crystal does not cause problems for the prism based spectrometer within a temperature stability of about 1 K.

### 5.4.2 Spectrometer

From the observed dispersion in Fig. 5.3(a) it follows that the THz radiation from 0.3 THz to 0.6 THz would be dispersed over a distance of 9.5 mm. Figure 5.5(a) shows the measured bolometer signal versus position for the THz beam from the GaAs wafer, as well as the observations when using the 300 GHz or the 600 GHz frequency selective surface (FSS) filter in combination with the GaAs THz source. The bolometer positions are given relative to the signal maximum.

The low intensities at negative bolometer positions are due to two effects. Firstly, the larger dispersion $dn/d\lambda$ at higher frequencies (Fig. 5.3) separates the high-frequency components over a large area in the plane. As a consequence, half of the position range is covered by the frequencies between 0.95 and 1.1 THz. Secondly, the absorption losses in CsI increase at higher frequencies (Fig. 5.2). From Eq. (5.9), we estimate that the transmittance ranges from 36 percent at 0.2 THz to 7 percent at 1 THz. Additionally, there are some reflection losses at lower frequencies where the angles of incidence onto the prism surfaces differ from the Brewster angle. Comparing bolometer signals when recording the non-dispersed THz radiation with the signals of the same THz radiation after the prism, we estimate an overall transmission of roughly 10%. This overall transmission agrees qualitatively with calculations

**Table 5.1:** Two-term Sellmeier coefficients for Cesium Iodine.

| T [K] | A$_1$ | $10^2 A_2$ | $B_1$ [$\mu m$] | $B_2$[a][$\mu$m] | $10^4$Err[b] |
|---|---|---|---|---|---|
| 10 | 4.82 | 0.89 | 126.25 | 163 | 21 |
| 31 | 4.85 | 2.61 | 124.91 | 163 | 12 |
| 52 | 4.10 | 84.45 | 110.71 | 163 | 6 |
| 72 | 3.91 | 104.78 | 105.90 | 163 | 5 |
| 92 | 3.81 | 116.88 | 102.07 | 163 | 5 |
| 113 | 3.76 | 123.86 | 100.35 | 163 | 5 |
| 133 | 3.83 | 117.25 | 103.16 | 163 | 5 |
| 154 | 4.02 | 98.65 | 108.49 | 163 | 7 |
| 175 | 3.96 | 104.98 | 107.80 | 163 | 7 |
| 195 | 3.96 | 107.16 | 106.62 | 163 | 7 |
| 216 | 3.75 | 129.44 | 101.02 | 163 | 6 |
| 237 | 4.37 | 69.11 | 112.77 | 163 | 4 |
| 258 | 3.50 | 159.85 | 87.096 | 163 | 2 |
| 298 | 3.77 | 132.93 | 97.58 | 163 | 2 |

[a] Fundamental phonon absorption frequency [cm$^{-1}$].
[b] Only valid for the region shown in Fig. 5.3

**Table 5.2:** Two-term Sellmeier coefficients for Kalium Bromide.

| T [K] | A$_1$ | $A_2$ | $B_1$ [$\mu m$] | $B_2$[a][$\mu$m] | $10^4$Err[b] |
|---|---|---|---|---|---|
| 10 | 2.20 | 0.88 | 44.38 | 87.72 | 9 |
| 31 | 1.78 | 1.33 | 7.12 | 87.72 | 2 |
| 52 | 2.00 | 1.12 | 34.21 | 87.72 | 2 |
| 72 | 1.82 | 1.33 | 7.63 | 87.72 | 2 |
| 92 | 1.94 | 1.23 | 24.42 | 87.72 | 2 |
| 113 | 2.01 | 1.18 | 28.90 | 87.72 | 4 |
| 133 | 3.08 | 0.13 | 59.30 | 87.72 | 2 |
| 154 | 2.46 | 0.78 | 47.50 | 87.72 | 5 |
| 175 | 1.85 | 1.40 | 20.93 | 87.72 | 6 |
| 195 | 2.05 | 1.23 | 31.53 | 87.72 | 6 |
| 216 | 2.08 | 1.21 | 33.20 | 87.72 | 5 |
| 237 | 1.77 | 1.53 | 53.12 | 87.72 | 8 |
| 258 | 2.41 | 0.901 | 46.23 | 87.72 | 13 |
| 278 | 1.74 | 1.58 | 30.18 | 87.72 | 1 |
| 298 | 1.57 | 1.76 | 8.61 | 87.72 | 1 |

[a] Fundamental phonon absorption frequency [cm$^{-1}$].
[b] Only valid for the region shown in Fig. 5.3

**Table 5.3:** Two-term Sellmeier coefficients for Kalium Chloride.

| T [K] | $A_1$ | $A_2$ | $10^6 B_1$ [$\mu m$] | $B_2$[a][$\mu$m] | $10^4$Err[b] |
|---|---|---|---|---|---|
| 10 | 1.65 | 1.59 | 19.49 | 70.42 | 3 |
| 21 | 1.64 | 1.59 | 44.70 | 70.42 | 3 |
| 32 | 1.66 | 1.59 | 47.61 | 70.42 | 3 |
| 42 | 1.67 | 1.58 | 21.03 | 70.42 | 3 |
| 52 | 1.71 | 1.55 | 54.30 | 70.42 | 2 |
| 72 | 1.69 | 1.59 | 28.33 | 70.42 | 2 |
| 93 | 1.75 | 1.55 | 77.64 | 70.42 | 1 |
| 113 | 1.73 | 1.57 | 30.22 | 70.42 | 1 |
| 133 | 1.75 | 1.56 | 27.74 | 70.42 | 1 |
| 154 | 1.77 | 1.56 | 5.96 | 70.42 | 1 |
| 175 | 1.79 | 1.54 | 44.60 | 70.42 | 1 |
| 195 | 1.77 | 1.57 | 46.44 | 70.42 | 1 |
| 217 | 1.77 | 1.58 | 40.11 | 70.42 | 1 |
| 237 | 1.79 | 1.57 | 44.05 | 70.42 | 1 |
| 258 | 1.75 | 1.60 | 9.85 | 70.42 | 1 |
| 278 | 1.79 | 1.57 | 3.93 | 70.42 | 1 |
| 299 | 1.77 | 1.60 | 15.73 | 70.42 | 1 |

[a] Fundamental phonon absorption frequency [$\mathrm{cm}^{-1}$].

[b] Only valid for the region shown in Fig. 5.3

using the measured absorption coefficients of CsI and further reflection losses on the surfaces.

A relative wavelength scale is reconstructed and a frequency spectrum follows as shown in Fig. 5.5(b). We have used the 300 GHz and 600 GHz FSS filters[156], one to fix the frequency scale with position and the second one to validate the calculated frequency axis. The measured spectra are corrected for absorption losses in CsI (Eq. (5.9)). The CsI prism spectrometer is sufficiently transparent from 0.2 to 1.1 THz. The estimated resolution (Eq. (5.11)) of the CsI prism based-spectrometer is shown in Fig. 5.6. The steep decrease of the resolution towards higher frequencies reflects the behavior of the dispersion in CsI, see Fig. 5.3.

The FSS filter characteristics were determined by Biber et al.[156] with THz-TDS and show oscillations as can be seen in Fig. 5.7. The transmission measurements of the FSS filters with the CsI prism spectrometer are simulated by integrating the characteristic FSS filter spectra $I(\lambda')$ using a gaussian profile. The width of the gauss is a wavelength-dependent kernel and equals the $1/e^2$-resolution $\Delta\lambda(\lambda')$ of the CsI prism spectrometer (Fig. 5.6). The integration is performed over the whole spectrum and the convolutions $I'(\lambda)$ of the FFS filters are given by

$$I'(\lambda) = \int d\lambda' I(\lambda') \exp\left[-2\left(\frac{\lambda - \lambda'}{\Delta\lambda(\lambda')}\right)^2\right]. \tag{5.13}$$

The markers at 0.3 THz and 0.6 THz in Fig. 5.6 depict the deduced resolution of 170 GHz and 95 GHz. We expect a resolution near 1.0 THz of 32 GHz. The resolution seems to be unaffected by the finite transmission of the prism and the reduction of

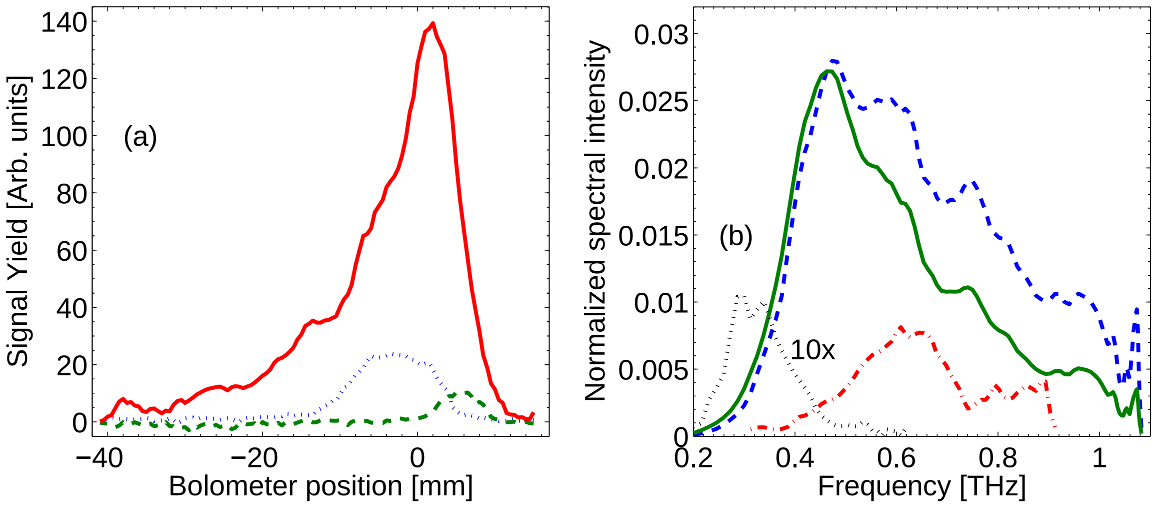

**Figure 5.5:** (a) The power distributions observed with a moveable Bolometer. (solid) radiation from the GaAs wafer, (dashed) 300 GHz FSS filter, (dotted) 600 GHz FSS filter. (b) Reconstructed THz frequency distributions (the correction equals the transmission $T$ of CsI, Eq. (5.9)), (solid) radiation from the GaAs wafer (uncorrected), (dashed) THz spectrum (corrected), (dotted) 300 GHz FSS filter (corrected), (dash-dotted) 600 GHz FSS filter (corrected). The spectrum of the 300 GHz filter is enlarged by a factor 10 for visibility.

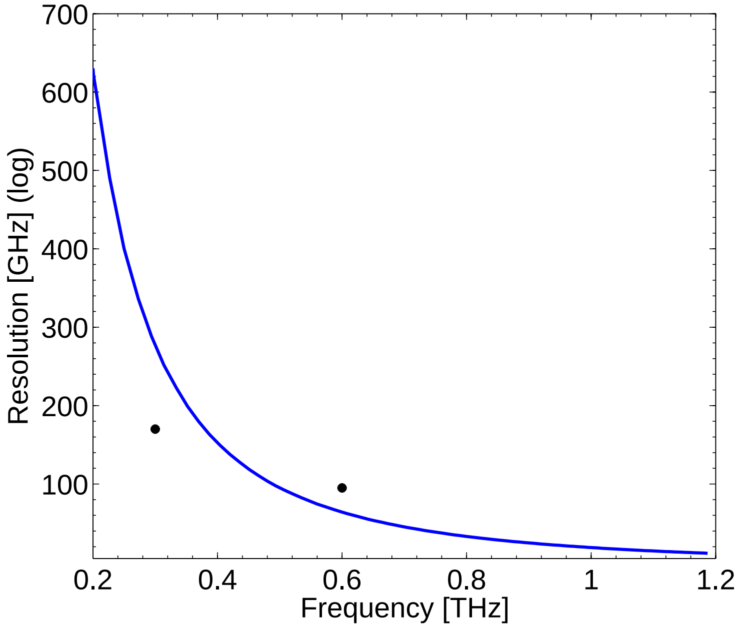

**Figure 5.6:** The estimated resolution of the CsI prism spectrometer using Eq. (5.11). The markers (●) indicate the resolution found using the FSS filters.

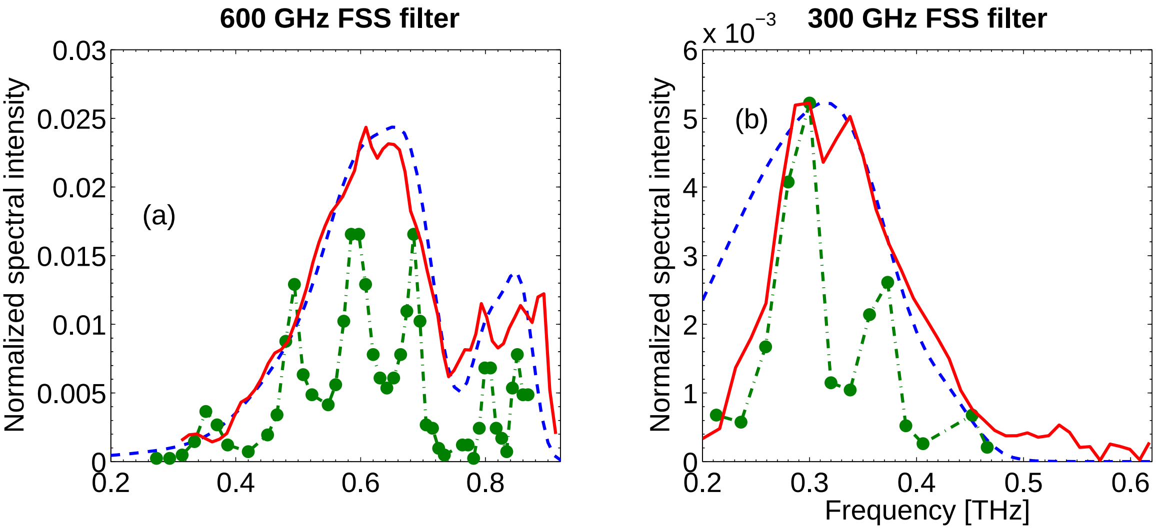

**Figure 5.7:** Comparison of the observed and expected frequency distribution using the FSS filters. (a) 600 GHz filter and (b) 300 GHz filter, dashed-dotted lines: filter characteristics[156], solid lines: measurements, dashed lines: convolutions using a Gaussian distribution with a FWHM equal to 95 GHz at 0.6 THz and 170 GHz at 0.3 THz.

the beam width. To our surprise, the resolution at 0.3 THz is found to be a factor 3 better than predicted by Eq. (5.11).

## 5.5 Conclusions

Transmission THz-TDS measurements have been used to obtain the refractive index and absorption coefficient for CsI, KBr and KCl as a function of temperature and frequency between 0.2 and 2 THz. The wavelength dependence of the refractive index can be described very well with a two-term Sellmeier representation. We have constructed a cryogenic, 25 K cooled CsI-prism spectrometer with a 120 mm TPX lens, which was tested with a pulsed THz source and bandpass filters. The CsI prism spectrometer is sufficiently transparent from 0.2 to 1.1 THz. The CsI prism spectrometer has a resolution of 32 GHz near 1.0 THz, about 95 GHz at 0.6 THz, and 170 GHz at 0.3 THz. The prism spectrometer opens the ability to perform two-dimensional spectroscopy in which time (delay) and frequency response may be studied.

## Acknowledgment

We acknowledge financial support from the Foundation for Technical Sciences (Stichting Technische Wetenschappen (STW)). This work is part of the research program of the Foundation for Fundamental Research on Matter (Stichting FOM) and made possible by financial support from the Netherlands Organization for Scientific Research (Nederlandse Organisatie voor Wetenschappelijk Onderzoek (NWO)).

# CHAPTER 6

# Far-infrared camera based on a gas-phase photocathode of Rydberg atoms

A prototype far-infrared camera is developed based on ionization of gas-phase Rydberg atoms. The photocathode of highly excited rubidium atoms as photo-detectors operates from 1 - 1000 $\mu m$ and has an exposure time of 10 ns, which removes the need for cryogenic cooling. We provide the theoretical background describing of the imaging properties the ion-optics, the Rydberg atoms in the photocathode, and the sensitivity of the camera for infrared photoionization. We demonstrate the Rydberg camera by showing measurements of a contact print image of test-target as a mask and a wired grid using 1.064 nm radiation from a YAG laser.

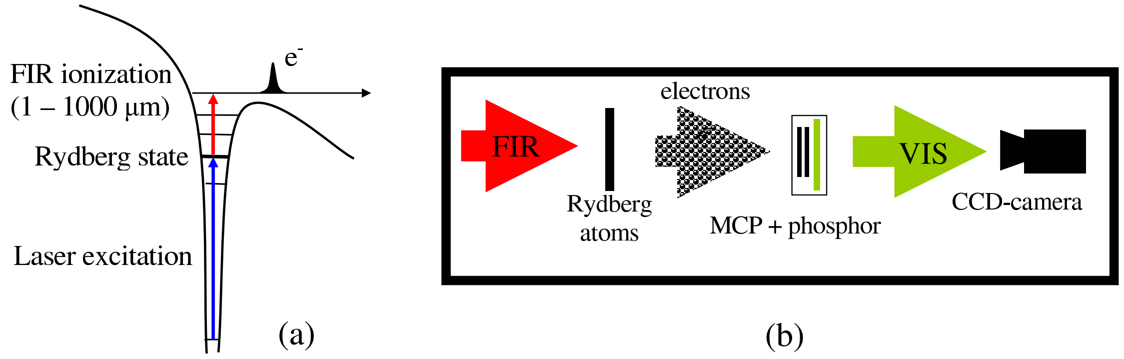

**Figure 6.1:** (a) Laser excitation creates Rydberg atoms, which are ionized by FIR radiation with energy exceeding the electron binding energy. The ionization barrier is continuously tunable by choosing the Rydberg state and the external electric field strength. (b) As FIR radiation interacts with Rydberg atoms, photoionization produces electrons that are amplified by the MCP. The electron distribution is visualized with a phosphor screen, which lights up, and a CCD-camera records the images.

## 6.1 Introduction

Infrared (IR) cameras are widely used to monitor temperature differences between objects and record infrared sources, such as stars. In the near IR from 0.6 – 20 $\mu m$, pyroelectric and ferroelectric based cameras operate at room temperature, as like Golay cells[160], which are pneumatic detectors designed for operation in the spectral range 20 - 1000 $\mu m$. Bolometers with arrays of silicon detectors are cooled to liquid nitrogen or helium temperatures to reduce the dark current and extent to the far-infrared (FIR) regime from 20 - 1000 $\mu m$[161]. Recently, room temperature microbolometer technology has imaged a human hand at the frequencies of 0.2 THz and 0.3 THz[162]. The drawback of the conventional long-wavelength cameras is their slow response times ($10^{-3}$ s).

Much faster imaging cameras exist within the visible domain. High-speed cameras possess ultrashort exposure times of $10^{-8}$ s, much faster then photo- and CCD cameras. To take advantage of these cameras, image intensifiers with high response times are used to convert UV or near-infrared radiation into visible light. As photons are impinging upon a metallic or alkaline photocathode plate, the photo-electric effect produces electrons that are amplified and visualized with a phosphor screen. The high electron amplification factor of a micro channel plate (MCP) makes it possible to visualize also low intensity radiation. This technology enables night vision devices for surveillance under moonlight or starlight. For most photocathode materials, the sensitivity is limited to wavelengths shorter than 1.6 $\mu m$[163]. Unfortunately, beyond this wavelength the quantum efficiency of photocathodes becomes negligible.

In this chapter, we investigate an alternative photocathode for two-dimensional imaging of IR radiation based on gas-phase rubidium atoms in a highly excited Rydberg state[164–168]. The so-called "Rydberg" atoms created after laser excitation have a weakly bound outer electron with binding energy given by the Rydberg formula $E_b = -13.6/n^2$ eV, see Fig. 6.1(a), where $n$ is the principal quantum number with typical binding energies of 0.001 - 1.24 eV (1 - 1000 $\mu m$). Although the density of

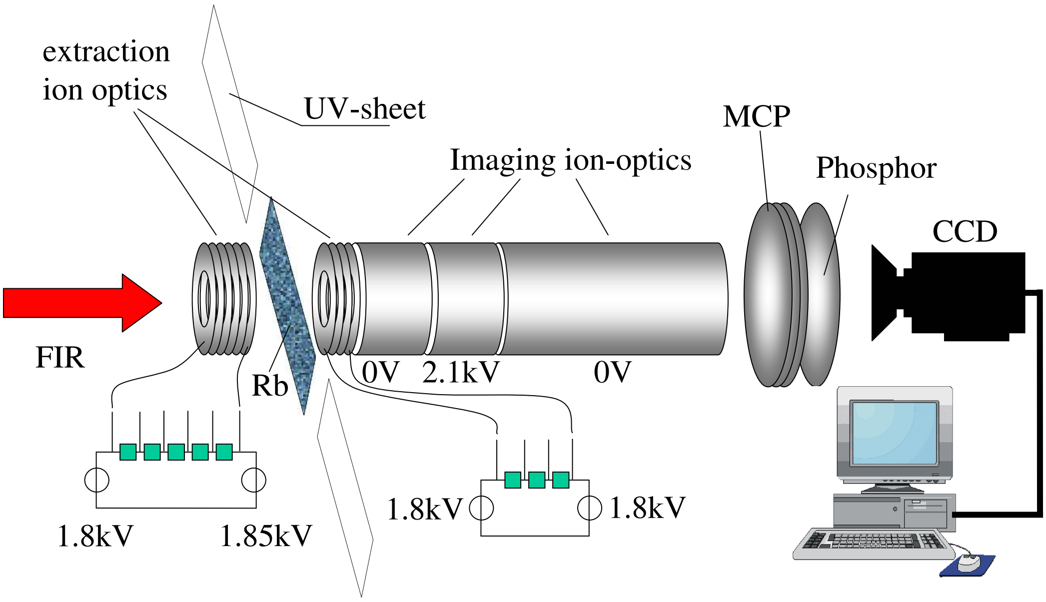

**Figure 6.2:** Experimental setup. The extraction ion-optics creates a homogenous field in the plane of the UV laser sheet which excites Rb atoms to a Rydberg state. The profile of a FIR source is imprinted on the Rydberg sheet by ionization. The resulting ion distribution is imaged on a MCP detector by electrostatic optics.

gas-phase atoms ($\approx 10^6\ cm^{-3}$) is very low compared with solid-state detectors, the combination of a low ionization threshold with the high photoionization cross section makes a Rydberg atom a very suitable detector for FIR radiation[164]. The energy barrier is continuously tuneable by choosing the principle quantum number $n$ of the Rydberg state and the strength of the external electric field.

Photoionization of the Rydberg atoms by FIR radiation creates both electrons and positive ions. Imaging means simply guiding these charged particles by electrostatic optics towards a MCP. The spatial distribution is transferred to a phosphor screen, see Fig. 6.1(b). Gating of our camera provides exposure times between 10 ns and a few $\mu s$, which removes the need for cryogenic cooling. A far-infrared lens system for imaging objects on the photosensitive layer enables the FIR camera to work as a conventional camera.

## 6.2 Experimental setup

Our prototype FIR camera is shown in Fig. 6.2. The photosensitive cathode is created in a cloud of evaporated rubidium (Rb) atoms from a $70°C$ oven in a vacuum chamber ($10^{-7}mbar$). In the interaction plane, a thin film of rubidium atoms is photo-excited by an optical sheet of ultraviolet light (UV) from a tunable dye laser. As entrance windows, we use fused silica for the UV laser sheet and quartz glass for the FIR radiation.

In a static electric field created by the extraction ion-optics, UV light excites a Stark-state. The excited Rb-atoms in the Rydberg photocathode are photo-ionized

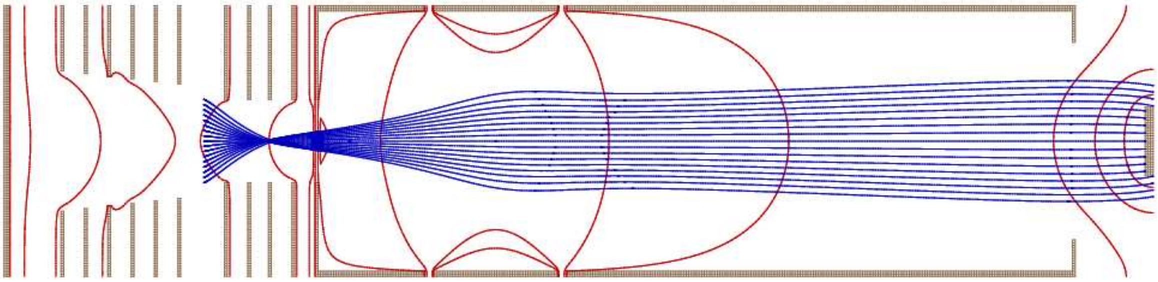

**Figure 6.3:** The cylindrical electrostatic optics consists of two parts: first, the electrostatic extraction optics, composed of six plates before and four plate after the photocathode. Secondly, a three-element Einzel lens. In analogy with light optics, a telescope is formed with an ocular at the entrance of the Einzel lens and an objective in the second cylinder of the Einzel lens. The curved vertical isopotential lines illustrate the focusing action of the electrostatic optics. The horizontal lines depict the flight trajectories of the charged particles.

by FIR radiation. In most experiments, detecting ions is preferred over detecting electrons, as electrons are more susceptible to stray fields. Also, the photo-electric effect creates background electrons. The resulting Rb$^+$-ion distribution is extracted from the interaction region. While conserving their former positions, the ion optics accelerates and guides the charged particles towards a MCP and the spatial distribution is transferred to a phosphor screen. We gate the detection by switching the microchannel plate (MCP) voltage from 800 to 1800V. The obtained images on the phosphor screen are recorded with a CCD-camera (Lavision). In all cases of obtaining images with the Rydberg camera, we take two subsequent data sets: an image with THz radiation illuminating the optical elements and a background image with the THz beam blocked. An image is built up in 10 s by averaging over 100 laser shots. In the following, we only present background corrected images.

To allow the entrance of FIR radiation perpendicular to the Rydberg atom sheet, open electrostatic optics were designed and simulated with Simion$^{(TM)}$[169]. Figure 6.3 shows the cylindrical electrostatic optics. The isopotential lines are depicted as vertical curved lines and the charged particle trajectories as solid horizontal lines.

The ion optics consists of two parts: extraction optics and a three-element Einzel lens. Important to imaging ion-optics design is the conserved relative position of the charged particles created in the Rydberg photocathode. Design criteria are a constant electric field strength across the interaction region and minimal distortion in the image plane. In this way, it is possible to generate a real image of FIR radiation with the Rydberg camera.

### 6.2.1 Extraction optics

The electrostatic extraction optics is composed of two sets of 6 and 4 metal rings of 50 mm in diameter and spaced by 8 mm, as shown in Fig. 6.3. The two sets are spaced by 16 mm and the region between the sets forms the extraction region, in which the Rydberg photocathode is created. To minimize distortion of the FIR wavefront by diffraction on the metal rings, the first lens set has decreasing ring apertures from

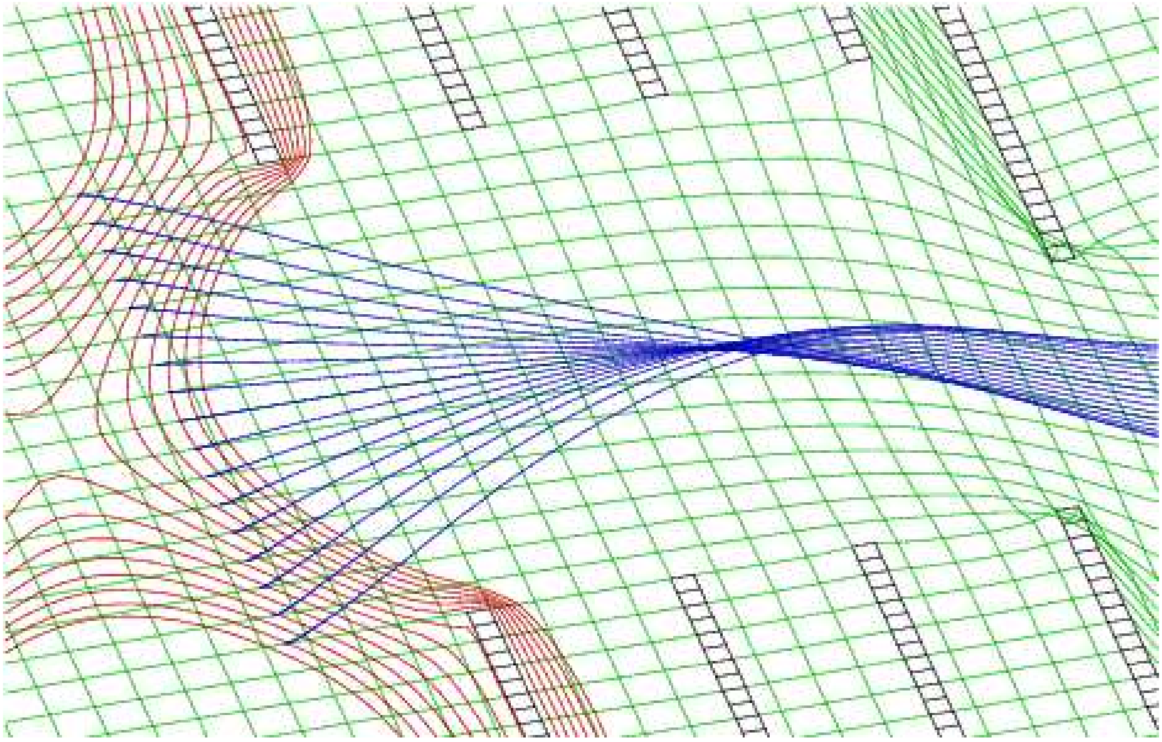

**Figure 6.4:** The potential energy surface (chequered pattern) at the interaction region. An homogeneous electric field is created by the extraction optics (visible as a flat surface), where the Rydberg photocathode is situated. Towards the opening of the three-element Einzel lens, the surface becomes curved, which causes the charged particles to be focused.

left to right from 35 mm to 30 mm, see Fig. 6.3. The rings are interconnected with resistances of 1 $M\Omega$ and biased with a positive voltage, such that a linear voltage rise (or voltage drop) is created. This arrangement leaves a free entrance for the IR radiation to the Rydberg atoms and minimizes the penetration of the surrounding electric field (earth potential of 0V) through the open electrodes.

In the experiment and in the simulation, as depicted in Fig. 6.3, from left to right, we have chosen to bias the first set with 1.8 kV. The voltage is raised with 10 V on each ring until 1.85 kV on the last ring, while the whole second set is biased with 1.8 kV and can be tuned to reduce the distortion in the image. In this way, as shown in Fig. 6.4, a homogeneous potential energy surface (chequered pattern) is created in the plane of the Rydberg photocathode. Towards the opening of the three-element Einzel lens, the potential surface becomes curved, which reflects the acceleration of the charged particles. Although the isopotential lines are curved (solid curved lines, spaced by 1 V/cm) in the interaction region, meaning that the potential and field orientation varies across the interaction region, the magnitude of the field is constant. Thus, each charged particle is created and accelerated in the same electric field.

We have chosen the electric field strength to be small, $\approx 13 \pm 1$ V/cm, because the Coulomb potential of weakly bound Rydberg electrons is highly susceptible to electric fields. In the presence of an external electric field, the so-called "Stark-effect" changes the energy eigenvalues of the electron (see Section 6.3.3). The variation in the electric field orientation has influence on the photoexcitation selection rule of the magnetic quantum number $m$ (see Section 6.3.5). We have chosen both the quantization axis of the atoms and the UV light polarization to be along the symmetry axis of the cylindrical optics. The small variation in the electric field orientation lifts the conservation of $m$ and transitions are allowed where $m$ changes $\pm 1$.

### 6.2.2 Three-element Einzel Lens

The two-dimensional ion distribution resulting from the interaction of FIR radiation with the Rydberg atom photocathode is projected on the MCP by the three-element Einzel lens[170,171], as shown in Fig. 6.3. In analogy with light optics, a telescope is formed with an objective lens at the entrance and an ocular in the second cylinder of the Einzel lens. At the entrance of the three-element Einzel lens, 40 mm from the Rydberg photocathode, a grid with a wire thickness of 100 $\mu m$ spaced by 1 mm is used to increase the homogenicity of the extraction electric field. The Einzel lens has an optimal setting of 2.1 kV and helps to compensate for a barrel or pillow distortion that is created in the extraction ion optics. The discussed settings of the electrostatic optics projects the ion-distribution onto the MCP with a magnification of approximately 1.4×.

## 6.3 Theory

### 6.3.1 Rydberg atoms

The Rydberg states of an atom are electronically excited states with low binding energies. Such Rydberg atoms have a number of peculiar properties, including an exaggerated response to electric and magnetic fields, long radiative lifetimes and electron wave functions that approximate the classical planetary picture of an electron in an orbit around the core. As it turns out, many aspects of Rydberg atoms can be calculated using a classical hydrogen model. The finite size of the rubidium core gives rise to a form of electron scattering, which is treated with the Quantum Defect Theory[172]. The outer electron in a stationary orbit around the core is bound with an energy of (note that atomic units are used unless stated otherwise)

$$E(n,l) = -\frac{1}{2(n-\delta_{n,l})^2}, \tag{6.1}$$

where $n$, $l$ and $\delta_{n,l}$ are the principal and angular momentum quantum number and the quantum defect of the angular momentum state $l$. The quantum defect $\delta_{n,l}$ describes the energy shift of the Rydberg electron with respect to hydrogen for $Z \neq 1$, where $Z$ is the atomic number. The quantum defect lifts the degeneracy for low angular momentum states. Highly excited Rydberg electrons are weakly bound to the core and each photonexcitation exceeding the binding energy can ionize the atom, see Fig. 6.1 (a). For instance, an $np = 38$ rubidium Rydberg electron has an binding energy of $4.12 \cdot 10^{-4}$ a.u. ($\delta_{n,l} = 3.132$ a.u.), corresponding to a photoionization frequency of 2.64 THz.

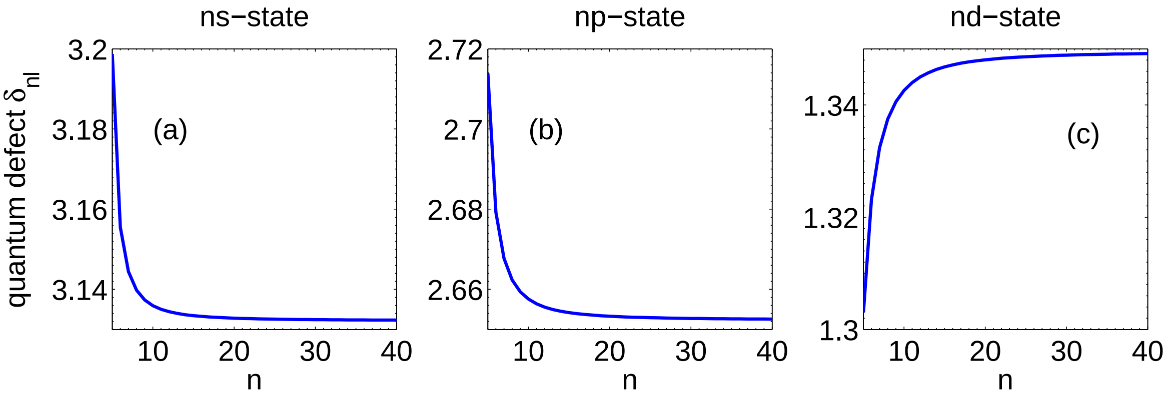

**Figure 6.5:** The quantum defects for the *ns*- (a), *np*- (b) and *nd*-states (c) in rubidium as a function of the principle quantum number $n$. Note that the quantum defect decrease towards larger $n$, except for $l$=2.

### 6.3.2 Intermezzo: Quantum defect for hydrogen-like atoms

We use the energy shift of the Rydberg electron in rubidium to calculate accurately in Section 6.3.5 the electron wave functions, and the photo-excitation, and ionization cross sections. The experimentally obtained quantum defects with high-resolution spectroscopy from W. Li *et al.*[173] are used. Figure 6.5 shows the values for the $s$, $p$, and $d$ states ($l=$ 1,2 and 3) as a function of the principal quantum numbers $n$.

The quantum defect $\delta_{n,l}$ is large for low $l$-states, because the outer electrons have elliptically shaped orbits around the core and pass through a cloud of tightly bound core electrons, which shield the nucleus. Temporally, the Rydberg electron is exposed to a larger core potential, which binds the electron more tightly with respect to hydrogen.

Rydberg electrons in a high $l$-state have almost circular orbits and most of their trajectory takes place in a $-\frac{1}{r}$ Coulomb potential. The quantum defect decreases rapidly towards higher l-states, see Fig. 6.5. Also outer electrons in high $n$-states have large orbits around the nucleus and their inner turning point is located further away from the nucleus. Therefore, the quantum defect $\delta_{n,l}$ decreases towards higher n-states and will reach an asymptotic value, see Fig. 6.5(a) and (b). This classical picture of an electron orbiting the core is very useful, but fails to explain the increase in the quantum defect of the nd-state in Fig. 6.5(c).

### 6.3.3 Static external electric field

The small binding energy of the excited electrons makes Rydberg atoms highly susceptible to external electric fields, thereby changing the dynamics of the Rydberg electron. On one hand, a saddle point is created that lowers the Coulomb potential of the outer electron, as seen in Fig. 6.6(a) and its energy is given by

$$E_{saddle} = -2\sqrt{F}, \tag{6.2}$$

where $F$ is the electric field strength. Rydberg states are field ionized whenever their binding energy $E_{n,l}$ exceeds this threshold. The field needed, ignoring the quantum

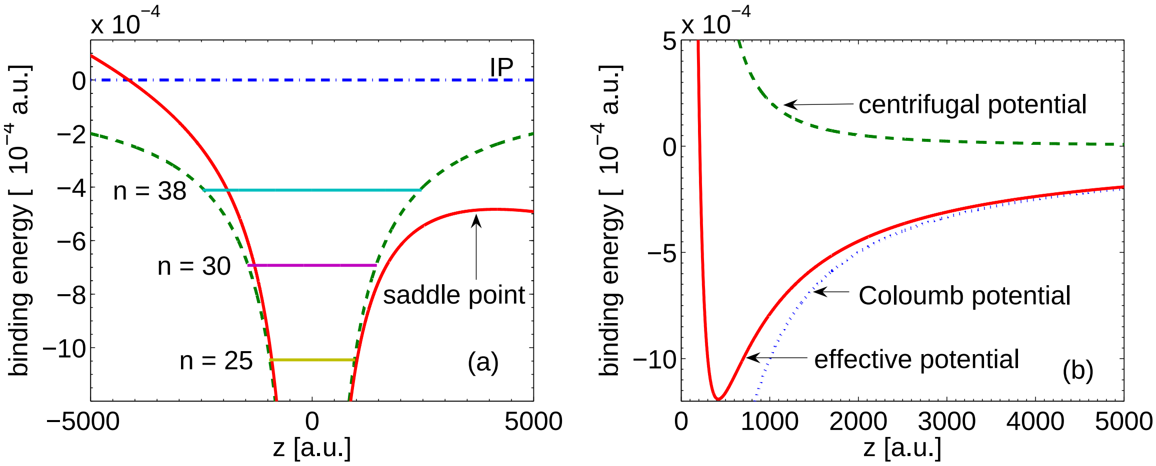

**Figure 6.6:** (a) Field-free Coulomb potential (dashed) for the Rydberg electron along the z-axis for V = -1/r. The energy positions of the three bound Rydberg states $n$ = 20, 30 and 38 and the ionization threshold (dashed-dotted) are depicted as horizonal solid lines. The electron potential is modified by an external electric field (solid) of 200 V/cm, V = -1/r + Fz, and a saddle point arises, which field ionizes $n$ = 38. (b) Coulomb (dotted) and centrifugal potentials (dashed), which are summed to give the effective radial potential (solid), in which an electron of angular momentum $l$ moves.

defect, is given by

$$F = \frac{1}{16n^4}. \tag{6.3}$$

On the other hand, Rydberg energy levels are perturbed, which lifts the degeneracy of $l$-states, also know as the Stark-effect. The degenerate $l$-states become Stark-states and fan out with increasing field strength, as seen Fig. 6.7. Stark-states are labelled with a new quantum number $k$, since $l$ is no longer a good quantum number in the presence of an electric field. In the absence of a quantum defect, the energy of the Stark-states in first order reads

$$E(n,k) = -\frac{1}{2n^2} + \frac{3}{2}nkF, \tag{6.4}$$

where $k$ ranges from $-n+1+|m|, ...n-1-|m|$ with $m$ as the magnetic quantum number. The Stark-states increasing in energy as a function of the electric field ($k > 0$), called 'blue'-states, start to mix with states decreasing in energy ($k < 0$), called 'red'-states, at a field strength given by

$$F = \frac{1}{3n^5}. \tag{6.5}$$

This field strength defines the beginning the $n$-mixing regime. For instance, at a field strength of 31.7 V/cm, the $n$ = 35 manifold meets the $n$ = 36 manifold.

### 6.3.4 Selective field ionization

The gas-phase photocathode is based on ionization of Rydberg atoms by electromagnetic radiation. We suggest an alternative method, more suited for narrow-band

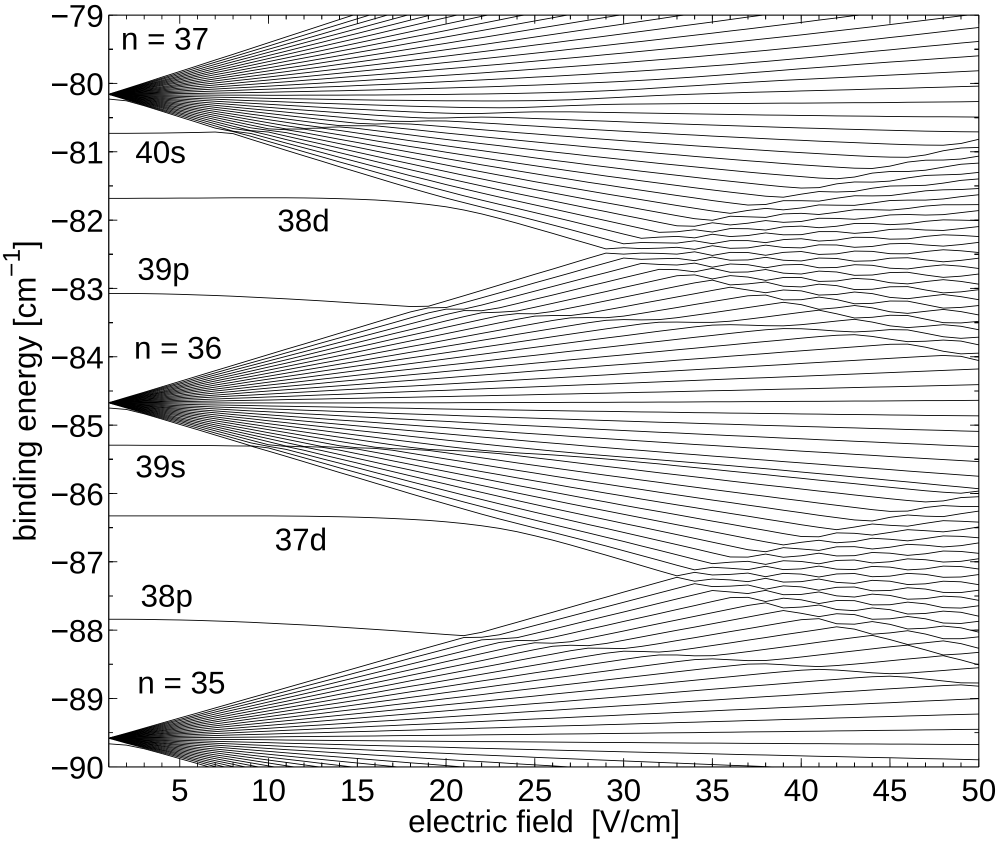

**Figure 6.7:** Stark map of rubidium. The degenerate *l*-states become Stark-states, which fan out with increasing field strength. The Stark-states increasing in energy as a function of the electric field are called 'blue'-states and states decreasing in energy are called 'red'-states.

radiation based on bound-bound transitions and subsequently a slow time-varying ionizing external electric field.

In this scheme, the incoming IR radiation excites in a field-free condition Rydberg atoms from an initially *n,l*-state to a high-lying *n',l'*-state. The spatial distribution of the IR source is imprinted in the *n',l'* Rydberg atoms and can be probed by applying a slow time-varying electric field on the extraction optics. The *n',l'* Rydberg states are selectively field ionized (SFI) and accelerated towards the imaging ion optics. The time-dependent arrival of the field ionized products from different *n',l'* Rydberg states on the particle detector provides frequency-selective imaging.

The SFI-imaging scheme has a number of advantages: (i) The cross sections of $\Delta n = 1$ bound-bound transitions are three orders of magnitude larger than for bound-free transitions (see Section 6.4), which greatly increases the sensitivity of the Rydberg camera for narrow-band radiation. (ii) The frequency-selectivity of the Rydberg photocathode is continuously tuneable by adjusting the Rydberg-Rydberg transition with a static electric field to a desired FIR wavelength (Stark-tuning)[125,167]. Gürtler *et al.*[125] used this technique to detect water vapor in air with broad band THz radiation using Rydberg atoms as detectors.

### 6.3.5 Dipole approximation

The sensitivity of the Rydberg atoms in the photocathode for IR radiation is governed by the dipole matrix element between high-lying states. We have set out to calculate the dipole matrix elements for bound-bound and bound-free transitions of Rydberg states from $n = 5$ to 70 in rubidium. In the low-intensity limit, a cross section can be assigned to a process involving interaction with single photons. For bound-bound transitions the cross section reads[174] (atomic units are used unless stated otherwise)

$$\sigma_\nu^{b,b} \equiv \frac{\pi}{2}|\vec{D}|^2\nu(n)\Delta\omega^{-1}, \tag{6.6}$$

and for bound-free transitions

$$\sigma_\nu^{b,f} \equiv \frac{\pi}{2}|\vec{D}|^2\nu(n), \tag{6.7}$$

with $\nu(n)$ the transitions frequency, $\Delta\omega$ the transition line width, $\hat{z}$ the polarization direction of the electromagnetic field, $\psi_i$ and $\psi_i$ the unperturbed initial and final wave function, and $\vec{D} = \langle\psi_f|\hat{z}|\psi_i\rangle$ is the dipole matrix element.

The wave function $\psi$ describes the relative motion of the electron in an orbit around the core and can be obtained using the one-body Schrödinger equation[4], which reads

$$\left(-\frac{\nabla^2}{2} + V(r)\right)\cdot\psi = E\cdot\psi, \tag{6.8}$$

where $V(r)$ and $E$ are the effective electron potential and the energy eigenvalue. The potential of any single-electron atom is spherically symmetric. Therefore, the wave function $\psi$ can be separated into a radial part $R_{E,l}(r)$ and an angular part $Y_{l,m}(\theta,\phi)$.

$$\begin{aligned}\psi &= R_{E,l}(r)\cdot Y_{l,m}(\theta,\phi)\\ Y_{l,m}(\theta,\phi) &= \sqrt{\frac{(l-m)!}{(l+m)!}\cdot\frac{2l+1}{4\pi}}\cdot P_l^m(\cos\theta)e^{im\phi}.\end{aligned}$$

The calculation of $\langle\psi_f|\hat{z}|\psi_i\rangle$ can also be separated into a radial and an angular part. The latter is calculated analytically, independent of the shape of the potential V(r). Using the radial wave function $R_{E,l}(r)$, the radial part of the dipole matrix element is expressed as

$$M_{f,i} = \langle R_f(r)|r|R_i(r)\rangle = \int R_f(r)\cdot r\cdot R_i(r)dr. \tag{6.9}$$

The angular part of the dipole matrix element $\vec{D}$ for linearly polarized light gives rise to the well known selection rules $\Delta l = l_2 - l_1 = \pm 1$. The selection rule of the magnetic quantum number $m$ depends on the polarization angle of the light and on the quantization axis of the atom, which is in an external electric field orientated along the electric field $\vec{F}$. If both axis coincide, $m$ is conserved, while in other cases transitions occur in which $m$ changes $\pm 1$. The angular part of the dipole matrix element for $\Delta l = \pm 1$ and $\Delta m = 0$ transitions can be expressed as

$$L_{f,i} = \langle Y_f(r)|\cos(\theta)|Y_i(r)\rangle = \sqrt{\frac{(l+1)^2 - m^2}{(2l+1)(2l+3)}}, \tag{6.10}$$

and the dipole matrix element reads $\vec{D} = M_{f,i} \cdot L_{f,i}$.

In most experiments, a single photoexcitation from the ground state is a first step and the cross section $\sigma(n)$ for exciting a resolved Rydberg state can also be estimated by[172]

$$\sigma(n) = \frac{\sigma_{IP}}{\Delta W n^3}, \tag{6.11}$$

where $\sigma_{IP}$ and $\Delta W$ are the ground state photoionization cross section (For Rb $\sigma_{IP} = 10^{-19}\ cm^2$) and the energy resolution (bandwidth) of the excitation laser. The cross section $\sigma(n)$ for exciting a Rydberg state is proportional to the energy spacing $n^{-3}$ between states.

### 6.3.6 Effective potential for hydrogen-like atoms

The radial part of the dipole matrix element is obtained by solving $R_{E,l}$ in Eq. (6.8). The effective V(r) potential is unique for every atomic system. However, the exact shape can not be directly measured, but the potential becomes apparent through the energy eigenvalues $E_{n,l}$. These values are experimentally obtained by high resolution spectroscopy[173] with an incredible accuracy. For hydrogen, the effective potential reads

$$V(r) = -\frac{1}{r} + \frac{l(l+1)}{2r^2}. \tag{6.12}$$

The first and second term represent the Coulomb potential and repulsive centrifugal force, see Fig. 6.6(b). Alkali atoms, like rubidium, are hydrogen-like with a large core and tightly bound electrons causing the Coulomb potential to deviate from $-\frac{1}{r}$. As a consequence, the degeneracy of low $l$-states is lifted, as depicted in Section 6.3.1. In the following, we present a highly accurate method to determine the Rydberg series in hydrogen-like atoms by adapting the Coulomb potential V(r) at short range. Using a number of experimental highly accurate energy eigenvalues, a consistent prediction of all energy eigenvalues $E_{n,l}$ is achieved. To obtain real rubidium radial wave functions $R_{E,l}$, the first term of Eq. (6.12) is rewritten as an Yukawa potential and reads[175]

$$V(r)_{ykw} = -\frac{K(r)}{r}. \tag{6.13}$$

Hideki Yukawa invented this potential to account for the strong force between protons and neutrons in the nucleus. He accurately calculated the existence of the pion, for which he received the Nobel prize in 1949. It turns out that the Yukawa potential also describes the screening of the nucleus by tightly bound electrons. At large distances, the Yukawa potential reduces to $-\frac{1}{r}$.

As $V(r)$ tends to zero for large $r$, the solution of $R_{E,l}(r)$ for $E > 0$ will have an oscillatory behavior at infinity and is an acceptable eigenfunction for any positive value of $E$. Therefore, we find a continuous spectrum for $E > 0$ corresponding to an unbound ionized electron. For $E < 0$, the boundary conditions state that $R_{E,l}(r) = 0$ for $r \to \infty$ corresponds to an infinite number of discrete bound state in the Coulomb potential. The energy eigenvalues $E_{n,l}$ depend for $Z > 1$ on both the principal, $n$, and angular, $l$, quantum number and are degenerated with respect to the magnetic quantum number $m$.

### 6.3.7 Algorithm

The second-order differential equation in Eq. (6.8) is solved using the efficient Numerov algorithm. Accurate radial wave functions $R_{E,l}(r)$ are obtained for each energy eigenvalue $E_{n,l}$ in a minimization routine adjusting the effective potential $V(r)$ through the Yukawa parameters. We developed an iterative fit procedure that uses the energy eigenvalues $E_{n,l}$ of several Rydberg states with their quantum defects $\delta_{n,l}$ (Eq. (6.1)). We use an expansion in the Yukawa potential of Eq. (6.13), which reads

$$K(r) = \sum_{k=1}^{l} A_k e^{-B_k r} + \frac{Cr}{1+r^4} + 1, \tag{6.14}$$

where C is a constant. Using only five values for $A_{1,2}$, $B_{1,2}$ and C, the Yukawa representation reproduces the energy eigenvalues $E_{n,l}$ and the quantum defect $\delta_{n,l}$ in rubidium with a least square residual better then $5 \cdot 10^{-3}$ ($A_1 = 5.267$, $A_2 = 30.733$, $B_1 = 1.040$, $B_2 = 4.275$ and $C = 1.209$). The accurate reproduction of the energy eigenvalues forms a good starting point for determining the transition dipole moments and hence the sensitivity of the photocathode.

## 6.4 Cross sections

From the radial wave functions, $R_{E,l}(r)$, the dipole matrix elements $\vec{D}$ are calculated using Eq. (6.9) and Eq. (6.10). The corresponding bound-free cross sections $\sigma_{f,i}^{b,f}$ in rubidium are shown in Fig. 6.8 for a final state energy of $E_f = 10^{-18}$ a.u. (close to threshold) as a function of the photoionization frequency. The initial Rydberg state ranges from n = 5 to 70 with $l = 0$, 1 and 2 (s, p, d) ($\Delta l = 1$). A first observation is that with increasing Rydberg state the excited rubidium atom becomes more sensitive for far-infrared radiation. The dynamic range in frequency of our photocathode is large, spanning from 0.7 - 1000 THz (430 $\mu$m - 296.8 nm). Due to small quantum defects of high l-states, the cross section of d-f transitions in rubidium is nearly hydrogen-like. In hydrogen, the s-p, p-d, and d-f transitions have similar behaviors. However, in rubidium, the s-p, and p-d transitions are suppressed. This has to be related to the large quantum defects of these states (Section 6.3.2). When photo-ionizing a specific Rydberg state, the cross section is in general not strongly frequency-dependent, as long as the photon energy exceeds the binding energy. Therefore, the photoionization cross section is constant over the bandwidth of the IR source.

In Fig. 6.9, the bound-bound cross sections $\sigma_{fi}^{bf}$ for $\Delta n = 1$ transitions are shown as a function of the photoexcitation frequency. The initial Rydberg states range from n = 5 to 70 with $l = 0$, 1 and 2 (s, p, d) ($\Delta l = 1$). Note that the cross sections pertain to IR sources with a bandwidth that matches the transition line width ($\frac{\Delta\omega}{\Delta W} = 1$). From scaling laws, we can deduce that the transition line width is proportional to $n^{-3}$ and is typical 121 kHz for a n = 32 Rydberg state[173]. Hence, a 10 ns IR laser with a Fourier transform limited bandwidth of 44 MHz has already a ratio of $\frac{\Delta\omega}{\Delta W} = 0.003$. Therefore, the effective cross section does not always increase towards high n-states. Fig. 6.9 shows that the frequency range extends to lower values than in Fig. 6.8 and encompasses 0.03 to 800 THz (9 mm - 375 nm). The Rydberg atoms have become 4

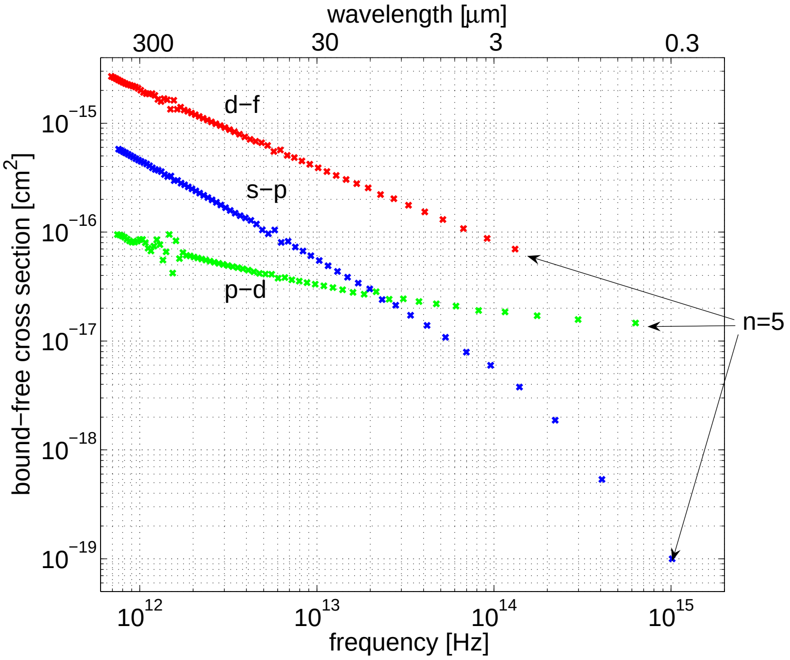

**Figure 6.8:** The cross sections $\sigma_{fi}^{bf}$ in rubidium for bound-free at threshold (final state energy $E_f = 10^{-18}$ a.u.) as a function of the photoionization frequency. The initial Rydberg state ranges from n = 5 to 70 with $l$ = 0, 1 and 2 (s, p, d) ($\Delta l = 1$).

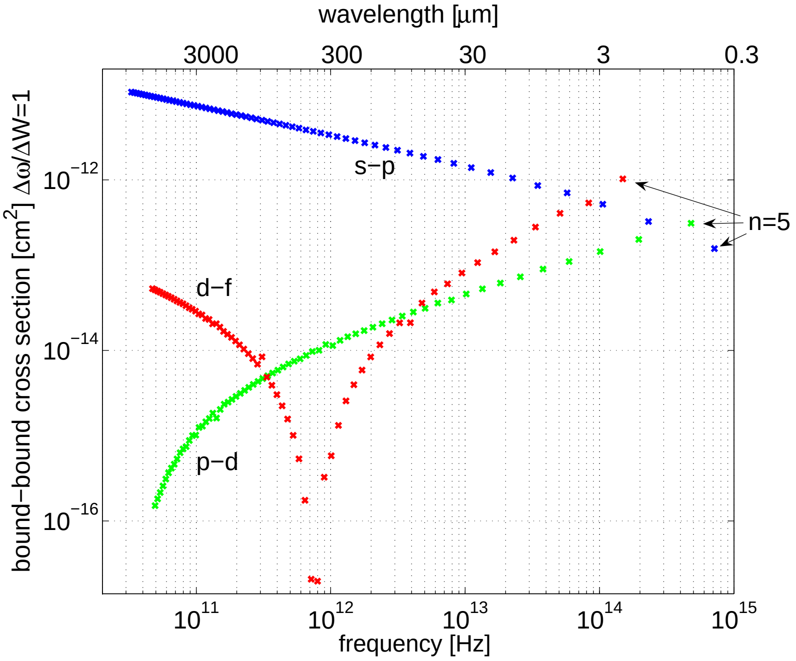

**Figure 6.9:** The cross sections $\sigma_{fi}^{bf}$ for $\Delta n = 1$ bound-bound transition transitions in rubidium as a function of the photoexcitation frequency. The initial Rydberg state ranges from n=5 to 70 with $l = 0$, 1 and 2 (s, p, d) ($\Delta l = 1$).

orders more sensitive for s-p transitions in comparison to bound-free transitions for the same transition frequencies. The increasing cross section towards lower frequencies is not only due to matching of the IR source with the bandwidth of the line width, but also due to overlapping wave functions $R_{n,l}(r)$ and $R_{n+1,l+1}(r)$ (Eq. (6.9)). Therefore, the radial dipole matrix element $M_{f,i}$ for s-p transitions increases towards higher n-values. However, a quantum defect $\delta_{n,l}$ is related to phase shifts of the radial wave functions and can strongly affect the value of overlap integrals. This, we observe in Fig. 6.9. For p-d transitions, a Cooper minimum is found at the ionization threshold and for d-f transitions a Cooper minimum is found at n = 27 (0.8 THz)[174]. The s-p, p-d and d-f cross sections differ by several orders of magnitude. In comparison with hydrogen, the s-p cross section is four orders of magnitude larger. Also, Cooper minima do not exist in hydrogen. The observed structure in the cross sections of rubidium are intrinsic properties of the atom and the bound-bound cross sections with their Cooper minima have so far not yet been measured. The high sensitivity and frequency selectivity of the Rydberg atoms for bound-bound transitions may be employed using selective field ionization as discussed in Section 6.3.4.

## 6.5 Sensitivity

A photosensitive 'film' of gas-phase rubidium is the key element of our Rydberg camera that converts FIR photons into a detectable charge of electrons or ions, see Fig. 6.1(b). We determine the theoretical sensitivity $S$ $[A/W]$ of the Rydberg photocathode for single photon ionization. The probability of FIR photons in a beam, expressed as an intensity $I_{fir}$ $[W/cm^2]$, to create an electron flux (current) $\Phi_{el}$ $[A/cm^2]$ in the photocathode is given by

$$S = \frac{\Phi_{el}}{I_{fir}} = \frac{N_{Ryd} \cdot \sigma_{fi}^{bf} \cdot e}{h\nu(n)}, \tag{6.15}$$

where $N_{Ryd}$ and $e$ is the surface density of Rydberg atoms and the electron charge (note that $I = dQ/dt$). The surface density of Rydberg atoms $N_{Ryd}$ can be approximated by

$$N_{Ryd} = \frac{E_{uv}}{h\nu_{uv}} N_{atm}\sigma(n), \tag{6.16}$$

where $\frac{E_{uv}}{h\nu_{uv}}$ represents the number of UV-photons per area and $N_{atom}$ is the number of rubidium atoms in the photocathode.

Furthermore, similar to image intensifiers[163], it is possible to calculate a gain factor $G$ [W/W] for the complete Rydberg camera. We account for the MCP gain $G_{MCP}$, the efficiency of the phosphor screen $\eta_{phos}$ and the gain of the Rydberg camera reads

$$G_{fir} = S \cdot G_{MCP} \cdot \eta_{phos}. \tag{6.17}$$

As an example, the number of rubidium atoms evaporated from the oven in the photocathode of $30 \times 30 \times 1$ $mm^2$ is estimated to be $10^9$. A $60 \times 1$ mm UV laser sheet of a 100 $\mu J$ pulse at 297.59 nm with a bandwidth of 0.1 $cm^{-1}$ produces a photon flux $\Phi_{uv}$ of $2.5 \cdot 10^{14}$ $cm^{-2}$. The photoexcitation cross section $\sigma(n)$ for an n = 38 Rydberg state is $4 \cdot 10^{-18}$ $cm^2$ (Eq. (6.11)). About $\approx 10^6$ Rydberg atoms are produced (Eq. (6.16)), meaning an excitation efficiency of $\approx 0.1\%$.

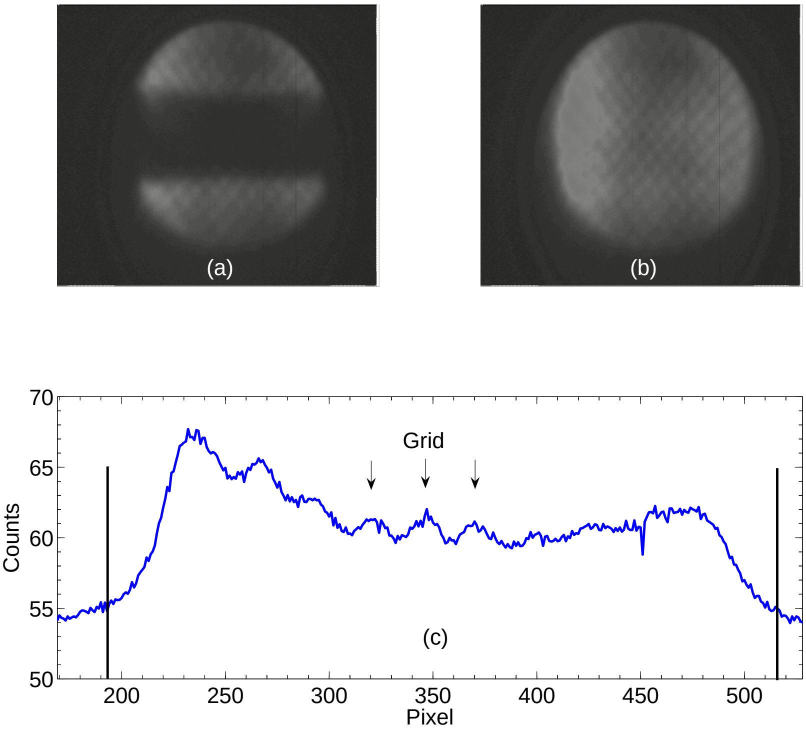

**Figure 6.10:** (a) Image of rectangular pattern created in the Rydberg photocathode by obstructing a part of the UV laser sheet. (b) Image of the Rydberg photocathode where the grid and contour of the phosphor screen is visible and is used to calibrate the magnification the THz camera. (c) Intensity line profile from the image in (b). Note that the grid is rotated by 45 degrees.

Figure 6.8 depicts the photoionization cross section $\sigma_{fi}^{bf}$ for the initial Rydberg states $l$ = 0, 1 and 2 (s,p,d) as function of the Rydberg photoionization frequency $\nu(n)$ (Section 6.3.5). As one can see, with increasing principle quantum number $n$ the photocathode becomes more sensitive and FIR radiation can be detected more efficiently. The sensitivity $S$ of an n = 9p Rydberg state for near-infrared photoionization at 81.85 THz is $S = 5.6 \cdot 10^{-8}$ mA/W ($\sigma_{fi}^{bf}$ of $1.91 \cdot 10^{-17}$ $cm^2$). Photo-ionizing a n = 38p Rydberg state with far-infrared 2.63 THz radiation gives rise to a sensitivity $S$ of $4.9 \cdot 10^{-6}$ mA/W ($2.5 \cdot 10^{-16}$ $cm^2$). The MCP gain in our FIR Rydberg camera has an amplification of $G_{MCP} \approx 10^6$ el/el and a phosphor screen efficiency of $\eta_{phos} \approx 0.5$ W/mA[163]. The estimated gain $G_{fir}$ of the far-infrared camera for 81.85 THz (n = 9p) is ≈ 0.03 and for 2.63 THz (n = 38p) ≈ 2.5.

The factor 83 increase of the sensitivity towards FIR is due to the larger photoionization cross section in Fig. 6.8 and the larger number of photons in a FIR beam($\frac{E}{h\nu}$) as Rydberg atoms are single photon detectors in the linear photo-ionization regime. Already in 1979, Kleppner and his coworkers quantified the efficiency of Rydberg atoms for FIR photon detection[164]. A sensitive CCD camera (Lavision) that records the images on the phosphor screen requires only $1\mu W$ per image. This means that a FIR light source at 2.63 THz with a repetition time of 10 Hz only needs tens of nanoJoule of FIR radiation per pulse to create an image on the computer screen.

Our camera is severely limited by the obtainable density of Rydberg atoms in

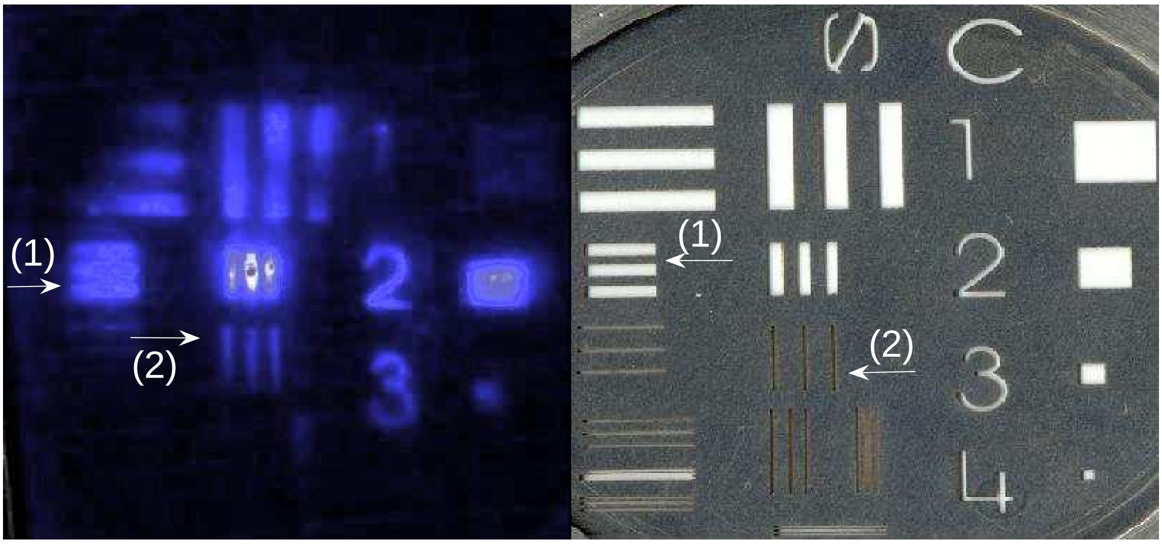

**Figure 6.11:** (A) THz contact image of a cross-shaped mask placed in front of the extraction region. (b) Optical image of the test-target mask.

the gas phase photocathode. However, this is compensated to a large extent by the enormous ionization efficiency of an individual Rydberg atom especially at long wavelengths. The limitation in density is partially practical in nature. A stronger laser and an oven at higher temperature means more Rydberg atoms. Apart from the sensitivity issue, other advantages are the imaging possibilities and the fast nanosecond detection.

## 6.6 Results

In this section, we study the capability of the Rydberg camera with open ion optics to image patterns created in the Rydberg photocathode. We use 1064 nm YAG laser radiation to test the spatial resolution and distortion of the imaging ion-optics.

### 6.6.1 Imaging properties

Figure 6.10(a) shows an image of a rectangular pattern created in the Rydberg photocathode by obstructing a part of the UV laser sheet. $Rb^+$-ions from the Rydberg photocathode are produced by collision induced ionization, which occurs $\approx 40$ ns after excitation by the UV laser. Clearly, one sees that the $Rb^+$-ion distribution is guided and projected onto the MCP with nearly no distortion.

In order to establish the linear magnification, we tuned the extraction optics so that the wires of a grid becomes visible. The grid is located 40 mm after of the Rydberg photocathode at the entrance of the three-element Einzel lens. The wire thickness is 100 $\mu m$ and the spacing 1 mm. In Fig. 6.10(b), the grid and the contour of the phosphor screen can be distiquished. Also here, the $Rb^+$-ions are produced by collisions. The phosphor screen has a diameter of 25.4 mm. The inhomogeneous intensity distribution is due to ageing of the MCP, which causes dark spots on the surface of the MCP and on the phosphor screen.

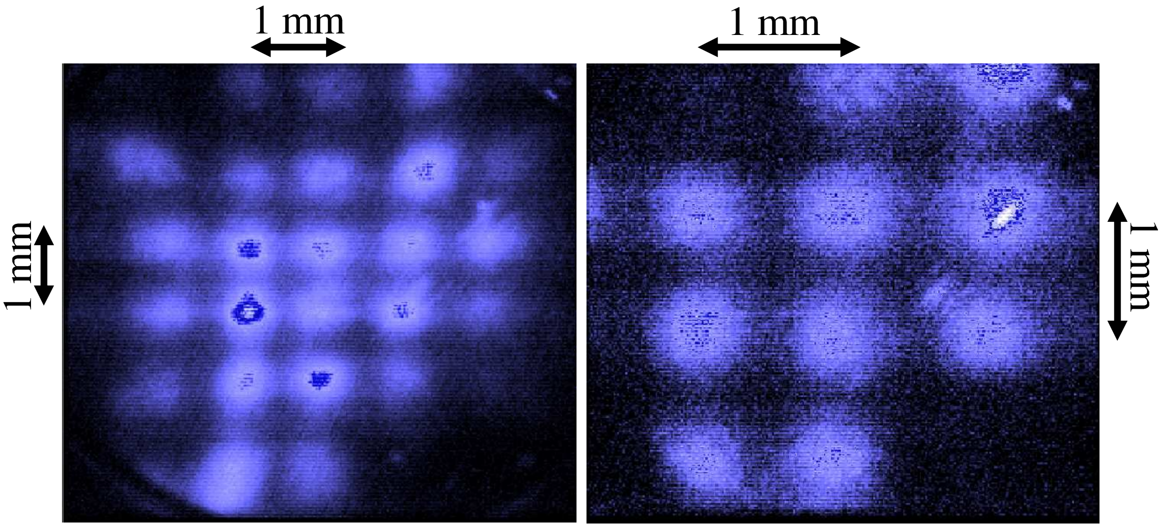

**Figure 6.12:** Images of a 1x1 mm grid placed 200 mm in front of the photocathode and illuminated with 1.064 nm IR radiation. (a) without compensation for pillow distortion, observable at the edges. (b) Minimizing distortion using the three-element Einzel lens.

Figure 6.10(c) shows a single line profile from the image in Fig. 6.10(b) and the grid is distinguishable (vertical arrows). Note that the grid is rotated by 45 degrees. The contour of the phosphor screen can be found (vertical lines) and an image distance of 72 $\mu m/pixel$ is determined. This gives rise to a magnification of $\approx 1.4\times$, which is in excellent agreement with the simulated ion trajectory in Fig. 6.3 in Section 6.2 for the same settings of the electrostatic optics.

### 6.6.2 Spatial resolution

We investigated the spatial resolution, which is the ability to distinguish two closely spaced objects in an image. Figure 6.11(a) shows a contact print image of a test-target as mask obtained with IR radiation at 1.064 $\mu m$ from a YAG laser. In Fig. 6.11(b), an optical contact image of the test-target is shown. The mask is placed as field plate No. 6 in the extraction ion optics, 8 mm in front of the photocathode.

The smallest resolved line spacing is 0.5 mm marked as (1) in Fig. 6.11(a). The smallest detectable line marked as (2) is 0.1 mm. The test-target illustrates that the spatial resolving power at 1.064 $\mu m$ is of the order of 200 $\mu m$.

### 6.6.3 Distortion

In Fig. 6.12 images are shown of a grid (1x1 mm) placed 200 mm in front of the photocathode and illuminated with 1.064 nm IR radiation from a YAG laser. We created photosensitive Rydberg atoms in a n = 19p Rydberg state. Fig. 6.12(a) is taken without compensating the distortion and (b) with distortion minimization by the three-element Einzel lens. While compensating the distortion with the Einzel lens, we observe that the magnification of the electrostatic optics changes. As distortion free imaging is more important, the magnification can not be chosen and is solely determined by the extraction field strength and the associated voltage on the Einzel lens. The pictures shown in Fig. 6.12 illustrate that the gas-phase FIR camera is capable of capturing two-dimensional images. In the following Chapter, we will extend our research to the far-infrared and show images produced with coherent terahertz pulses with a spectrum from a few gigahertz to $\sim 3$ THz (0.1 - 100 $\mu m$).

## 6.7 Conclusions

The Rydberg camera is sensitive for far-infrared from 1 - 1000 $\mu m$ (0.3 - 300 THz) with an ultra short exposure time, which removes the need for cryogenically cooling. Although the density is low, approximately $10^6$ Rydberg atoms in the photocathode, this density is sufficient to obtain IR images. The sensitivity of the Rydberg camera increases towards longer wavelengths. Employing bound-bound transitions in combination with selective field ionization creates the ability to be frequency-selective with an increase in sensitivity of 3 orders of magnitude. Based on numerical estimates, our Rydberg camera complements existing terahertz imaging techniques, in the far-infrared regime from a few gigahertz to $\approx 3$ THz. Open electrostatic ion-optics allows for perpendicular detection of infrared radiation. Images show the capability to compensate for distortion in extraction optics by tuning the voltage of the three-element Einzel lens. The total gain factor of the Rydberg camera is $\approx 0.03$ at 81.85 THz and increases to $\approx 2.5$ at 2.63 THz. This increase in gain factor is due to a larger photoionization cross section towards longer wavelengths and to the increase of the amount of photons in a FIR beam ($\frac{E}{h\nu}$). We estimate that only tens of nanoJoules of far-infrared radiation are needed to create an image.

Future studies might involve the implementation of selective field ionization to make the far-infrared camera frequency selective and the experimental verification of the Cooper minima in the bound-bound $\Delta n = 1$ transitions. Synthesis of THz pulses is possible by tailoring the femtosecond pulse and coherent tunable narrowband THz radiation can be produced in the range of 0.3 - 2 THz[176–181]. In the following chapter, the response of the Rydberg camera is tested in combination with coherent FIR radiation form a biased semi-conductor with a spectrum of 0.3 - 3 THz.

## Acknowledgments

The authors would like to thank H.G. Muller for stimulating discussions and the concept of calculating all dipole moments. This work is supported by the "Stichting Technische Wetenschappen (STW)", which is financially supported by the "Nederlandse Organisatie voor Wetenschappelijk Onderzoek (NWO)".

# CHAPTER 7

# Far-infrared Rydberg camera as a nonlinear detector for coherent THz pulses

We present measurements of far-infrared terahertz (THz) pulses with the Rydberg camera based on ionization of gas-phase Rydberg atoms. The function of the photocathode is demonstrated by showing a contact print image of a spatial mask. We investigate the ability of the Rydberg camera to distinguish the shadow cast by simple objects placed midway between the photocathode and a THz emitter. The response of the Rydberg camera is compared with that of a linear bolometer detector and with results from diffraction theory, which provides the THz radiative pattern in time, space and frequency. We simulate that diffraction reconstructs THz pulses with a nearly half-cycle pulse structures at positions with an experimentally high ionization probability. At positions with an experimental low ionization probability, the simulations show multiple wavefronts behind the main THz pulse. We find a strong correlation between the presence of multiple oscillations in the simulations and suppression of Rydberg ionization in the photocathode of the Rydberg camera. The diffraction calculations are in good agreement with the bolometer measurements and the Rydberg camera measurements are highly reproducible.

This chapter is partially based on **APL** 83, 222 (2003)[182]

## 7.1 Introduction

Imaging techniques for far-infrared (FIR) radiation in the terahertz (THz) frequency regime have obtained considerable attention in the last few years. Advances in generation[183–185] and detection of ultrashort THz pulses with a spectrum from a few gigahertz to $\approx 3$ THz have triggered a fast development of imaging techniques. The non-ionizing radiation is an excellent source for studies of materials[134,186–188], security[189,190] and medical applications[130,191]. Most reported THz imaging experiments use coherent detection techniques, recording the electric field electro-optically in a nonlinear ZnTe crystal. Either a single-spot detector was scanned through the beam or the two-dimensional (2D) electric field was recorded using a charge coupled device (CCD) camera[192]. Images of moving objects have been demonstrated in real time[193] and three-dimensional tomograms have been obtained using the temporal profile of a reflected THz pulse,[194].

An alternative method for 2D imaging of IR radiation is based on a photocathode of gas-phase rubidium atoms in a highly excited Rydberg state[164,168]. Such a Rydberg camera has imaged 1064 nm from a YAG, 55 $\mu m$ from a free electron laser (FEL)[168] and recently also far-infrared THz pulses from a large biased semi-conductor[182]. In Chapter 6, we provide a detailed description of a prototype Rydberg camera. Although the density of gas-phase atoms is very low ($\approx 10^6$) compared with solid-state detectors, the combination of a low ionization threshold with a high photoionization cross section makes a Rydberg atom a very suitable detector for low-amplitude THz radiation. Only tens of nanoJoules in THz pulses are needed to form an image. The short THz pulses are easily generated by illuminating the biased semi-conductor with femtosecond pulses. The pulsed nature of THz radiation matches the Rydberg camera exposure time.

In this Chapter, we will be concerned with the performance of the Rydberg camera using optical elements like lenses and obstacles in combination with THz pulses. The basics of a camera is to distinguish the shadow cast by an object whenever an obstacle is placed midway between a screen and a point source. The use of optical elements changes not only the spatial intensity profile of a broadband THz beam, but also the spectral distribution[54–57] and thus the temporal characteristics of the THz pulse. For instance, in the focal point of a lens, the THz beam will evolve from a half-cycle pulse (HCP) into a single full-cycle pulse (FCP), where the wavefront also may experience a $\pi$-shift, due to a Gouy phase shift[55,195]. Spatiotemporal reshaping is mainly associated with absorption in optical components, propagation[17,196,197], refraction, scattering and diffraction on obstacles and apertures[198,199]. The exact pulse shape has a profound influence on the ionization process of highly excited atoms in the Rydberg camera. The emitted THz pulses from a biased semi-conductor are half-cycle in nature with a duration much shorter than the Kepler orbit time $\tau_K$ ($\approx 9$ ps for n=38) and transfer momentum to the Rydberg atom. The strong nonlinear momentum "kick" of the unipolar THz pulse[50–53] can easily photo-ionize highly excited Rydberg states and it has been shown that a 100% ionization efficiency can be reached at moderate THz field strengths. Whenever the THz pulse loses its half-cycle character, due to spatiotemporal reshaping, the ionization probability of Rydberg atoms will be greatly affected.

We study images of the Rydberg camera using freely propagating THz beams in

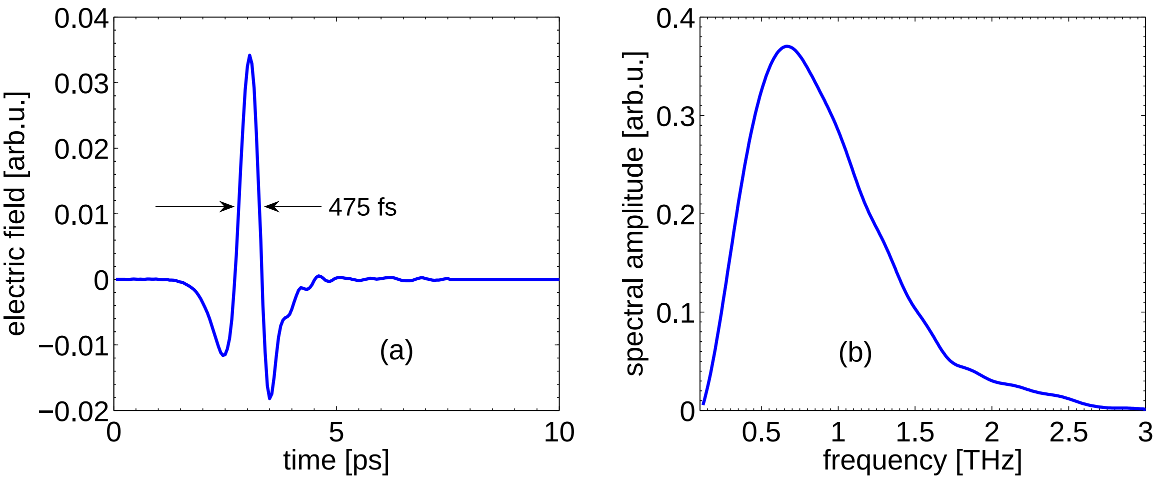

**Figure 7.1:** (a) Temporal profile of the THz pulse from a ZnTe crystal, measured with a time domain spectrometer (THz-TDS). (b) The spectral frequency distribution of the THz pulse after Fourier transformation.

the far field of the emitter in combination with optical elements, like a contact mask, a high density polyethylene (HDPE) lens, a small aluminum obstacle and a thin HDPE plate. Images obtained with the Rydberg camera show the spatial ionization behavior of the THz radiation pattern. To our surprise, many counterintuitive images are recorded. We used a linear bolometer detector to verify the measurements and imitate the situation inside the Rydberg camera. Model calculations solving the broadband version of the Rayleigh-Sommerfeld diffraction integrals provide the electric field distribution in space, time and frequency. The simulations are in good agreement with the bolometer intensity measurements and stress the importance of the pulse shape on the ionization probability in the photocathode of the Rydberg camera.

## 7.2 Experimental setup

The experimental setup of the far-infrared Rydberg camera is described in detail in Section 6.2. The THz radiation is generated in a standard biased large-aperture GaAs THz emitter with gold electrodes (Applied Solid State department, Radboud University Nijmegen), which is illuminated by 800 nm, 100 fs pulses from an Quantronix regeneratively amplified Ti:sapphire laser system. Photogenerated carriers are accelerated and as a result electromagnetic radiation is emitted[183]. The emitted electric field is proportional to the applied electric field strength across the emitter, $\varepsilon_{THz}(t) \propto E_{bias}$[197]. Figure 7.1(a) shows the temporal profile of a THz pulse from a ZnTe crystal, measured with a THz time domain spectrometer (THz-TDS)[17,136] and resembles a THz pulse from a GaAs wafer. Linearly polarized radiation from the emitter surface is confined in an ultrashort half cycle of $\tau_{THz} \approx 475$ fs, followed by a long tail of approximately 5 ps. The so-called 'half-cycle pulse' has a broad spectral distribution from 100 GHz - 3 THz (3 mm - $300\mu m$), as shown in Fig. 7.1(b). The spectral distribution peaks at 600 GHz and spans several octaves. The emitter is placed outside the vacuum chamber at variable distance from the photocathode.

We use a one-dimensional linear FIR bolometer detector (Far infrared Labs[200], aperture 3 mm) to measure the intensity distribution of the THz beam in the plane of our photocathode. For these experiments, we place the extraction ion optics (see Fig. 6.2 in Section 6.2) on an optical table to imitate the geometry inside the Rydberg camera. After the first lens set, the cryogenically cooled bolometer is mounted on a translation stage. A lock-in amplifier records the spatial intensity distribution.

## 7.3 Theoretical background

In this section, we first discuss the ionization behavior of terahertz (THz) half-cycle pulses (HCP) and full-cycle pulses (FCP) on Rydberg atoms. In Section 7.3.2, we present the broadband version of the Rayleigh-Sommerfeld diffraction integrals to verify the experimentally observed spatial intensity distribution of freely propagation THz pulses.

### 7.3.1 Impulsive approximation

The interaction of a THz-HCP with highly excited Rydberg atoms can be be understood in the classical picture of an electron in an orbit around a core. The ultrashort half-cycle field of the THz pulse has a duration of typically $\tau_{HCP} \approx 0.5$ ps (see Fig. 7.1(a)) and is much shorter than the Kepler orbit time, $\tau_K = 2\pi n^3$, of high Rydberg states ($\tau_K = 8.34$ ps for a n = 38 Rydberg state). In the limit $\tau_{HCP} \ll \tau_K$ (impulsive approximation), the THz pulse transfers momentum to the Rydberg electron given by (atomic units are used unless stated otherwise)[50]

$$\vec{\Delta p} = -\int_{-\infty}^{\infty} \vec{\varepsilon}_{THz}(t)dt, \tag{7.1}$$

where $\vec{\varepsilon}_{HCP}$ is the time-varying electric field of the HCP. The total change in energy after the Rydberg electron is subjected to a HCP is given by

$$\Delta E_{HCP} = \vec{p}_0 \cdot \Delta\vec{p} + \frac{1}{2}\Delta p^2, \tag{7.2}$$

with $\vec{p}_0$ as the initial momentum of the Rydberg electron. Note that the initial position and momentum of the electron is critical in evaluating Eq. (7.2). The THz-HCP ionization process is highly nonlinear[50–53] and therefore completely different from ionization in longer pulse fields ($\tau_{pulse} \gg \tau_K$). We solve the classical equation of motion for an electron in a Coulomb potential and obtain the binding energy of the electron in its orbits around the core after the THz pulse excitation. A detailed description is provided in Section 2.1. Figure 7.2 shows the final binding energy $E$ of a Rydberg electron in a 38p state for different arrival times $t_{THz}$ of the single full-cycle pulse (FCP) (a) and HCP (b). Both pulses are polarized in the z-direction and have the same duration. At t=0, the electron starts its trajectory at the inner point parallel to the direction of the THz and changes direction at the outer turning point (0.5 $\tau_K$). Depending on the arrival time $t_{THz}$ of the THz pulse and thus on the sign of $\Delta\vec{p}$, the

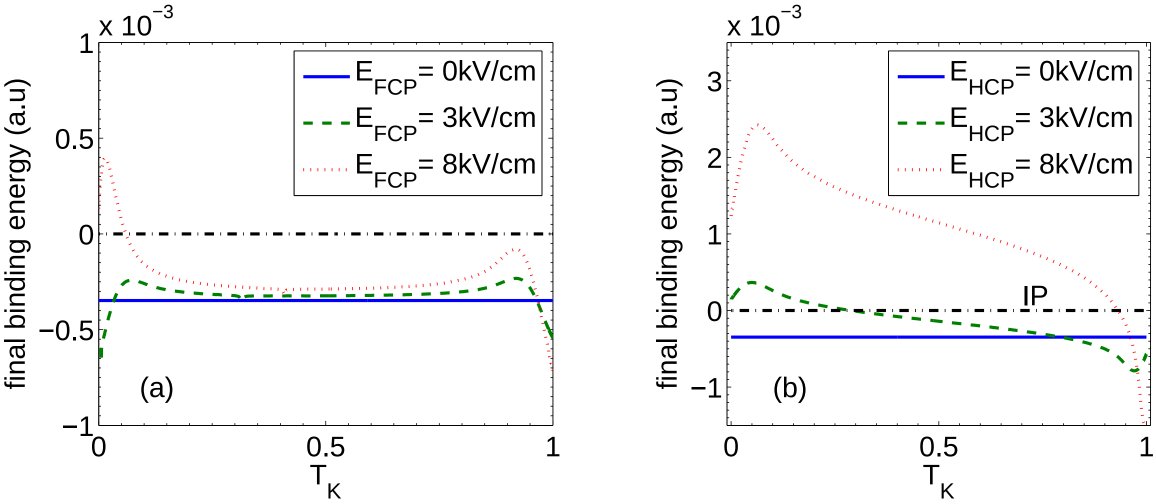

**Figure 7.2:** The final binding energy of the Rydberg electron after excitation for different arrival times $t_{THz}$ of a (a) FCP and (b) HCP. $\tau_K = 0$ is at the inner turning point. Both pulses are able to interact with the Rydberg electron at any point in its orbit around the core. The HCP transfers momentum more efficiently than a FCP. Note the different scales of the final binding energy.

Rydberg electron gains energy or loses energy, equivalent to stimulated emission and absorption. Note that the de- and excitation to other Rydberg states is not quantized in this classical model. In an ionization continuum, the final energy of the electrons can increase continuously with increasing THz field strength. A positive total energy means the atom was ionized during the excitation process.

Figure 7.2(a) depicts that FCPs mainly interact with the atom when the electron is near the nucleus and has large velocities (see Fig. 2.2(b)). Close to the inner turning point the electron loses energy, while elsewhere in its orbit, the electron gains energy. Far from the core, the FCP transfers nearly zero momentum to the Rydberg electron as $\Delta p \approx 0$ (Eq. (7.2)). The FCP does redistribute electrons to higher or lower Rydberg states by displacement $\Delta z = \int_{-\infty}^{\infty} dt' \int_{-\infty}^{t'} \varepsilon_{THz}(t)dt$. Below 4 kV/cm, the FCP interaction is symmetric around the nucleus, due to the full-cycle nature of the pulse. The symmetry is broken with increasing THz-FCP field strength and ionization comes from fast electrons near the core. Figure 7.3(a) depicts the ionization probability of a FCP. Only a small fraction of $< 10\%$ of an ensemble of Rydberg atoms is ionized at moderate bias fields. As we will show below, in comparison with a HCP, a FCP ionizes inefficiently.

In Fig. 7.2(b) is shown that the HCP is able to ionize the atom at any point of the electron in its orbit around the nucleus. As the strength of the HCP increases, first the fast Rydberg electrons near the core will ionize ($\Delta E_{HCP} = \vec{p}_0 \Delta\vec{p}$) with momentum parallel to the 'kick' direction. Subsequently, the second term of Eq. (7.2) dominates ($\Delta E_{HCP} = \frac{1}{2}\Delta\vec{p}^2$) the ionization process, such that electrons near the outer turning point with low velocities ($\vec{p}_0 \approx 0$) will ionize and eventually also electrons that move opposite to the THz-HCP momentum. Because the electron density is highest near the outer turning point, the ionization probability curve has

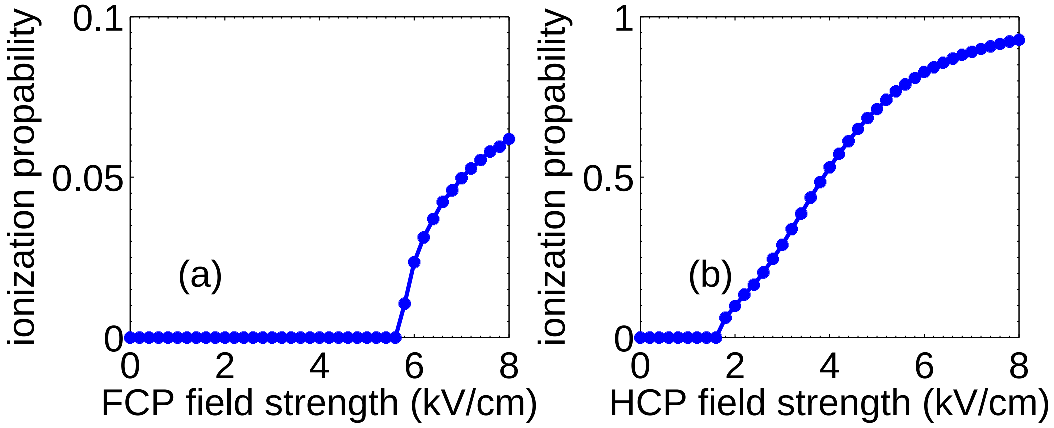

**Figure 7.3:** The ionization probability of (a) a FCP and (b) a HCP as function of the THz electric field strength.

an 's-shape'. This ionization probability 's-curve' is observed both experimentally[50,53] and predicted theoretically[58,59], as depicted in Fig. 7.3(b). Clearly, the 's-curve' shape is visible and at moderate biased field strengths a nearly 100% ionization efficiency can be reached.

Jones et al. and Reinhold et al.[50,53] have investigated the required field strengths for 100%, 50% and 10% ionization. Theoretically and experimentally, they deduced that close to saturation, the minimum field strength of HCPs scales as $\varepsilon_{HCP} \sim n^{-1}$. For 50% ionization, they found an $n^{-3/2}$ dependence, while at 10% ionization $\varepsilon_{HCP} \sim n^{-2}$.

In reality, the ultrashort half-cycle is followed by a slow low-amplitude negative tail ($\approx$ 5 ps, see Fig. 7.1), since Maxwell's equations demand that the time integral of the electric field is zero in free space for a propagating electromagnetic wave. The slow negative tail has little effect on the ionization probability for moderate n-states , but this tail can suppress the ionization significantly for n-states $\gg 70$[201,202].

In comparison with a FCP, a HCP ionizes very efficiently. As the ionization probability is highly depending on the unipolar shape of the THz pulse, a HCP that evolves into a FCP, due to spatiotemporal reshaping is expected to decrease the ionization rate significantly.

### 7.3.2 Scalar diffraction theory

The basic idea of a camera is to distinguish the shadow cast by an object whenever an obstacle is placed midway between a screen and a point source. However, absorption, refraction, scattering and diffraction on obstacles and apertures reshape the spatial frequency distribution of light and therefore also the spatiotemporal profile[197,199] of pulses. Ionization of Rydberg atoms strongly depends on the temporal pulse structure rather than on the intensity. Gürtler et al.[197] found that the THz beam from large emitters essentially behaves like a Gaussian beam and can be described in the far field by normal Gaussian propagation theory. The Finite Difference Time Domain (FDTD) method solves directly the Maxwell's equations of electromagnetic radiation and is able to simulate the propagation of a THz pulse[199,203]. However, the distance from emitter to photocathode of 300 mm, in combination with the size of the photosensitive layer, requires a grid that is too large for a normal PC (time steps of 20 fs gives a grid of $2.5\times10^8$ points). Central computer unit (CPU) time can be saved by using the broadband version of the standard diffraction integrals to describe the radiation pattern of a THz pulse in the far field[197]. The radiation pattern of the broadband THz beam can be solved using Huygens principle of superposition of spherical wavelets. If a monochromatic wave is emitted from a plane surface A (the THz emitter surface), the scalar representation of the complex spectral amplitude in the space in front of the emitter can be written as[2,197]:

$$\tilde{U}(\vec{x},\nu) = \frac{\nu}{ic}\int \tilde{U}(\vec{x'},\nu)\frac{exp(i\vec{k}_1(\nu)r)}{r}\left[\frac{cos(\vec{n},\vec{r})+1}{2}\right]\cdot d\vec{x'}, \tag{7.3}$$

where $\vec{x}$, $\vec{n}$, $\vec{x'}$ and $\nu$ are the observation point, the inward normal of the emitter surface, an integration point on the emitter surface and the frequency, respectively. $\vec{r}$ $= \vec{x'} - \vec{x}$ and r $= |\vec{r}|$ are the vector and distance from observation point to integration point. The term $\frac{1}{2}[cos(\vec{n},\vec{r'})+1]$ is known as the obliquity factor $K(\theta)$ and $\vec{k}_1(\nu) = 2\pi\nu[n(\nu) - 1 - i\alpha(\nu)]/c$ is the propagation vector with $n(\nu)$, $\alpha(\nu)$ as the refractive index and absorption coefficient representing the dielectric properties of the medium.

Equation (7.3) is also known as the Rayleigh-Sommerfeld diffraction integral. The general principle of the integration is that an ensemble of spherical wavelets $[\exp(i\vec{k}_1(\nu)r)/r]$ with spectral amplitudes $\tilde{U}(\vec{x'},\nu)$ are emitted from the antenna surface A and adds up in amplitude and phase to form the electric field $\varepsilon(\vec{x},t)$ at the position $\vec{x}$. The integral represents a scalar approximation of the full electric field vector, where the radiation pattern $\tilde{U}(\vec{x})$ of the THz pulse is obtained after integration over all frequency components. The spatial intensity distribution is $|\tilde{U}(\vec{x})|^2$. The spatiotemporal profile of the THz beam is obtained by inverse Fourier transformation of all spectral components $\tilde{U}(\vec{x},\nu)$:

$$\varepsilon(\vec{x},t) = \frac{1}{2\pi}\int_{\infty}^{\infty}\tilde{U}(\vec{x},\nu)exp(-i2\pi\nu t)d\nu. \tag{7.4}$$

The integral in Eq. (7.3) is valid for $r \gg \lambda$, which is for 0.1 THz $\gg$ 3 mm. All numerical simulations and experiments are performed for z $>$ 100 mm, where the theory is expected to be valid. The radiation pattern of a THz beam obstructed by an opaque or dielectric obstacle placed midway between the Rydberg photocathode and THz emitter is treated by defining the obstacle plane $r_1$ as new source of spherical wavelets $\tilde{U}_{r_2}(\vec{x},\nu)$. The new spherical wavelets $\tilde{U}_{r_2}(\vec{x},\nu) = \tilde{U}_{r_1}(\vec{x},\nu)\cdot\exp(i\vec{k}_2(\nu)r)$ are obtained by numerically integrating the diffraction integral Eq. (7.3) a second time. Note that when propagating a radiative pattern from source to obstacle and from obstacle to image plane, a $\pi/2$ phase shift must be included in accord with the Kirchhoff diffraction formula[2]. The phase shift appears in the obliquity factor, which becomes $\frac{1}{2}[cos((\vec{n},\vec{r'}) - \pi/2) + 1]$. However, we found that this phase shift does not change the spatiotemporal profile of the radiative pattern.

### Numerical simulations

All numerically calculated THz wavefronts (Eq. (7.3)) in Section 7.5.1 and Section 7.5.2 provide the spatiotemporal distribution of the THz beam for the non-vanishing

($\vec{x}$) component (parallel to the emitter plane) after propagating 300 mm from the $10 \times 10$ mm emitter. The model calculations provide the frequency distribution for all positions in the THz wavefront. After applying a Fourier transform Eq. (7.4), the temporal profiles are obtained. The integration step sizes at the emitter, $dx'$, obstacle plane, $dx_{r1}$, and observation screen, $dx_{r2}$, are 0.5 mm. The THz frequency distribution depicted in Fig. 7.1(b) is used to simulate the THz pulse. An effective step size of 100 fs is achieved by extending the frequency distribution to 10 THz in steps sizes of 0.01 THz.

The 9 mm wide rectangular aluminium obstacle used in Section 7.5.1 is simulated by modeling the spatial removal of the electric field in the propagation vector $\vec{k}_2(\nu)$ at the position of the obstacle.

The properties of the transparent high density polyethylene (HDPE) plate of 4 mm used in Section 7.5.2 are introduced by using the known refractive index as an increasing linear function, starting from 1.408 at 0.1 THz until 1.43 at 3 THz. Its absorption is introduced as an exponential function $(10^{-12} \cdot \omega)^3$ $cm^{-1}$ in the propagation vector $\vec{k}_2(\nu)$.

The simulations show the THz beam after propagation. By analyzing the reshaped spatiotemporal profiles, we should be able to rationalize the images obtained with the Rydberg camera.

## 7.4 Analysis of the Rydberg camera performance using THz pulses

First, we investigate experimentally the performance of the Rydberg camera using terahertz (THz) half-cycle pulses (HCP) and we determine the intensity dependence, the resolving power and imaging properties using lenses.

### 7.4.1 Intensity

The Rydberg camera with atoms in a highly excited state becomes a nonlinear detector in combination with THz pulses, due to the half-cycle pulse character (Section 7.3.1). Two-dimensional images obtained with the Rydberg camera depend more on the THz pulse shapes than on the THz intensity, as would be the case with linear cameras.

The observed response of the Rydberg camera on the THz-HCP field strength is depicted in Fig. 7.4(a). The UV laser excites with 300.59 nm UV radiation the n = 38 manifold in a static electric field of 13 V/cm and the Einzel lens is biased with 2.1 kV. Figure 7.4(a) depicts the spatial integrated ionization probability of Rydberg atoms in the photocathode, hence averaging over a range of THz intensities. With the THz emitter placed 150 mm from the photocathode (dashed), an ionization probability of 60% is reached at a bias voltage of 12 kV. THz pulses from the emitter placed at 300 mm from the photocathode only reach an ionization rate of 15% at 12 kV (solid). Clearly, the THz pulse energy has decreased significantly, due to propagation and diffraction. In both cases, an off-set in the bias voltage is observed before ionization starts, in agreement with the nonlinear behavior of THz pulses (see Fig. 7.3). The typical 's-curve' behavior of the ionization probability is not visible, due to the spatial averaging, which implies a large range of different THz intensities.

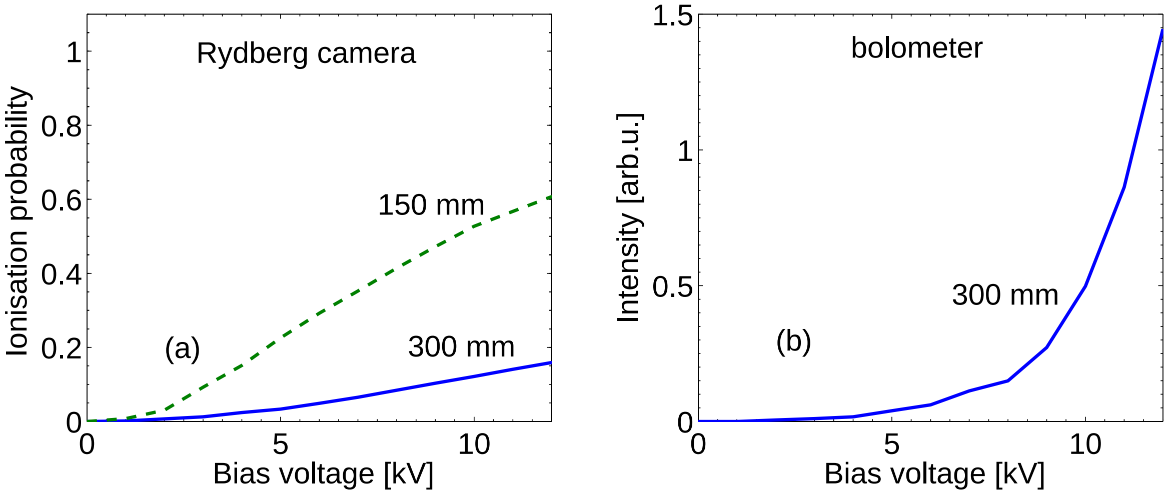

**Figure 7.4:** The characteristic dependency of the Rydberg camera and the linear bolometer for THz radiation are shown in Fig. 7.4(a) and (b) as function of the biased voltage. Note that the THz electric field is proportional with the biased electric field ($E_{bias} \propto \varepsilon_{THz}$)[197].

The bolometer measurements in Fig. 7.4(b) show that the fluence of the THz pulses scales nearly quadratic as $I_{THz} = |\varepsilon_{THz}(t)|^2$. This dependence confirms that the THz electric field strength is proportional to the applied biased electric field across the GaAs emitter $\varepsilon_{THz}(t) \propto E_{bias}$[197].

## 7.4.2 Resolving power

We investigate the resolving power of the Rydberg camera using THz radiation. Figure 7.5(a) shows a contact print image of a cross-shaped mask and Fig. 7.5(b) shows an optical image of the mask. The mask is placed as field plate No.6 in the extraction ion optics, 8 mm in front of the photocathode (see Fig. 6.2). In this experiment, 297.80 nm radiation excites the n = 34 manifold in a static electric field of 188 V/cm and the Einzel lens is biased with 1.9 kV. The widths of the branches of the cross are 1, 2, 3, and 4 mm in Fig. 7.5(c), starting at the upper right branch and counting counterclockwise. Clearly, the cross can be seen with the different branches. The upper right branch with a width of 1 mm is not visible, due to diffraction. The spectrum of the THz pulses peaks at ≈ 600 GHz, which corresponds to a wavelength of 0.5 mm being in the same order as the width of smallest branch. We can conclude from these observations that at longer wavelengths the spatial resolution is limited by diffraction.

## 7.4.3 Focusing

We demonstrate in this paragraph the effect of focusing the THz beam by a high density polyethylene (HDPE) lens. The use of a far-infrared lens system for imaging objects on the photocathode enables the Rydberg camera to work as a conventional camera. In Fig. 7.6 images are shown of a focused THz beam by a 70 mm HDPE bi-concave lens. We use the same settings as in Fig. 7.4. The THz emitter is fixed at 330 mm from the Rydberg photocathode and the lens is moved in step size of

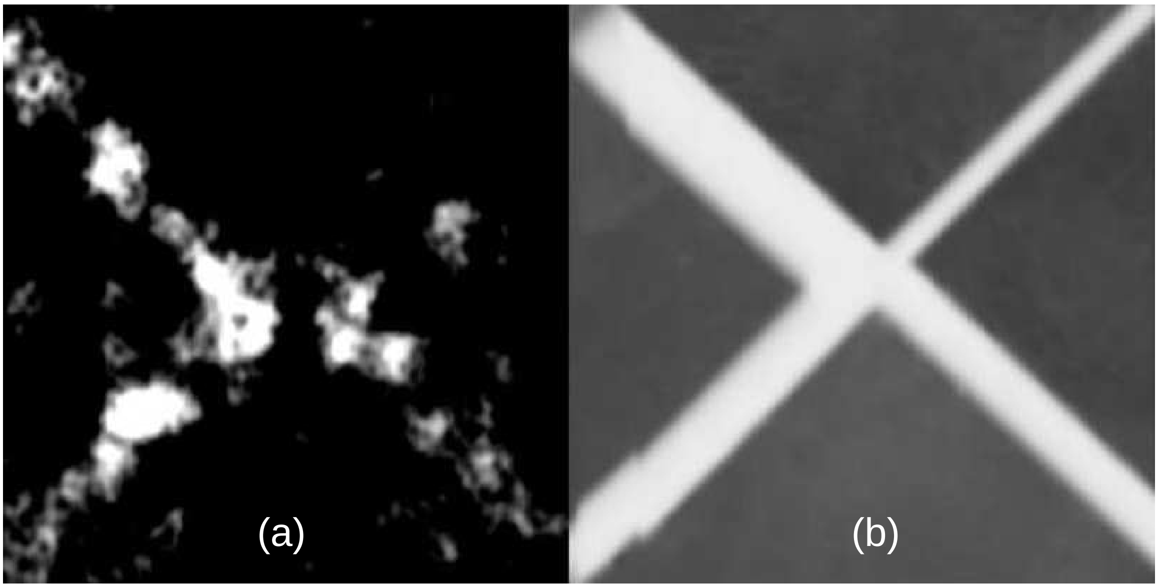

**Figure 7.5:** (A) THz contact image of a cross-shaped mask placed in front of the extraction region. The thinnest branch of 1 mm can not be resolved, due to diffraction. (b) Optical image of the test-target mask.

10 mm. One can immediately see a maximum ionization for a lens position of 100 mm from the THz emitter. Figure 7.7 shows the integrated ionization yields per image. The position of the maximum agrees with the lens-formula ($1/f = 1/s_0 + 1/s_1$ where $s_0$ and $s_1$ are the object and image distances). The magnification ($N = s_1/s_0$) of the lens at 100 mm is ≈ 2.3×. The size of our emitter is 10 mm. With this magnification, the image of the THz beam approximates the size of the phosphor screen. The integrated ionization yield is asymmetric, due to a more rapidly increasing spot size whenever the object distance is decreased, than when the object distance is increased. Figures 7.6 and 7.7 illustrate that lenses can be used to image and focus THz radiation onto the Rydberg photocathode. Hence, Gaussian propagation theory is applicable. In spite of this apparent success, we should note that half-cycle THz pulses change into a single full-cycle pulse in a focus. This phenomenon of pulse shaping has been predicted theoretically[54] and confirmed experimentally[56]. Propagation effects cause low frequency components to be diffracted from the beam center, while high-frequency components are mainly locate on-axis. This differential frequency loss from diffraction for the high and low frequency components is magnified, due to focusing. The chromatic abberations of lenses will also contribute to the differential frequency loss and the appearance of full-cycle pulses in the focus of a lens. As full-cycle pulses come with a low ionization efficiency (Fig. 7.3), the large ionization probability when focussing is surprising.

## 7.5 Propagation and imaging

In this section, we investigate the basic performance of the Rydberg camera: the ability to image shadows casted by simple objects placed midway between the THz

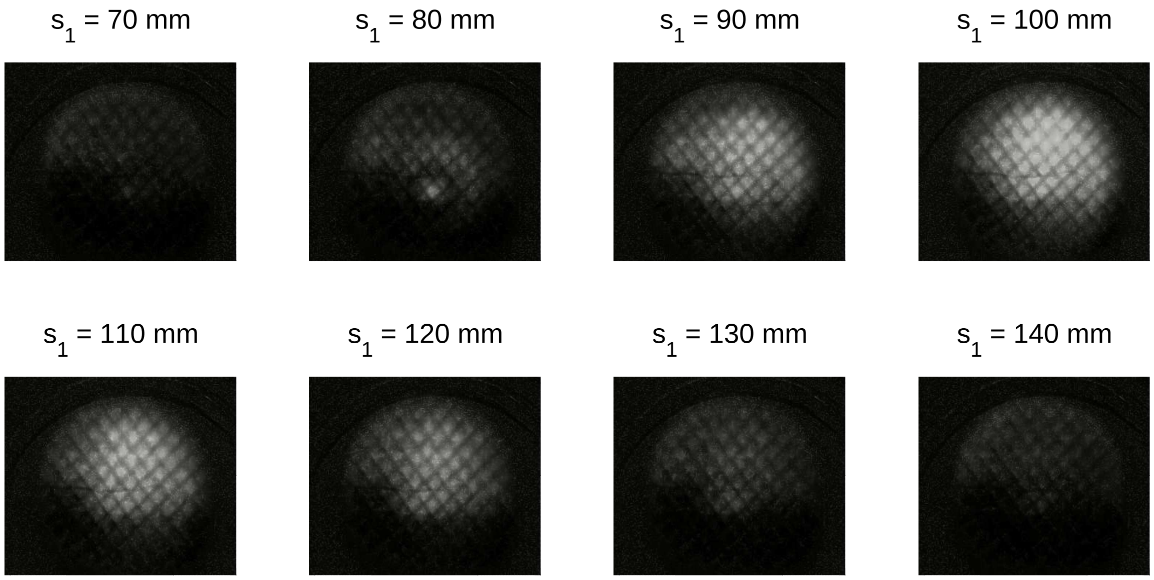

**Figure 7.6:** Images of the Rydberg camera for different positions of the 70 mm HDPE bi-concave lens with a fixed THz emitter position at 330 mm from the Rydberg photocathode. The grid at the entrance of the Einzel lens (see Chapter 6) is visible, due to the low extraction field in the ion-optics.

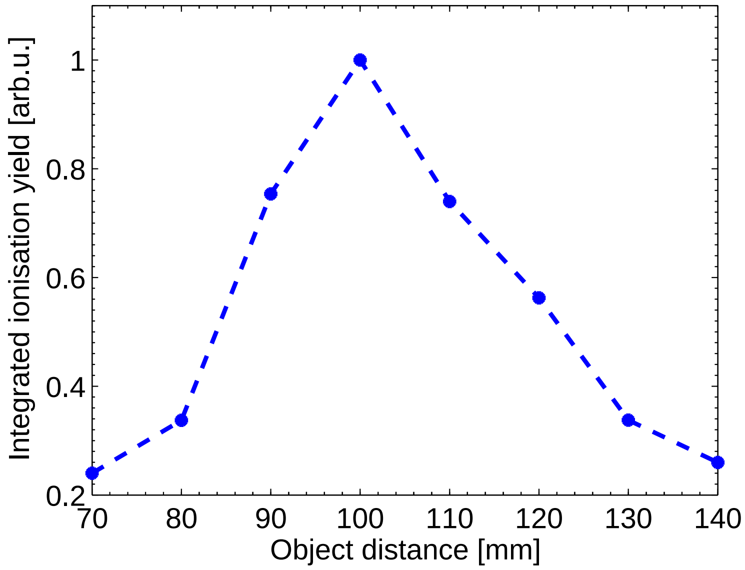

**Figure 7.7:** Integrated ionization yield for different positions of the 70 mm HDPE bi-concave lens with a fixed THz emitter position at 330 mm from the Ryberg photocathode. A maximum is found at 100 mm, which is in perfect agreement with the classical lens formula.

emitter and the photocathode.

As a test, the THz emitter is placed 300 mm from the photocathode. We obstruct the freely propagating THz beam at 100 and 200 mm from the photocathode with a 9 mm wide aluminum plate. Also a transparent HDPE plate of 4 mm thick is used to cover different portions of the THz beam. Images obtained with the Rydberg camera show the spatial ionization behavior of the THz radiation pattern. Because of the many counterintuitive images obtained, we verified each Rydberg camera measurement with a linear bolometer. The situation inside the Rydberg camera was imitated by placing the extraction ion optics (Fig. 6.2) on the optical table and by positioning the bolometer in the plane of the photocathode. Model calculations solving numerically the diffraction integrals (Eq. (7.3)) provide the spatial field distribution both in time and frequency domain. Although the measurements with the Rydberg camera are not easily explained, we found the measurements to be highly reproducible.

### 7.5.1 Opaque obstacle

In Fig. 7.8(a) single line profiles are shown from the center of a freely propagating THz beam measured 300 mm from the emitter with the Rydberg camera (solid), bolometer (●), and from simulations (dotted). Figure 7.8(b) depicts the simulated spatiotemporal profile of the THz pulse. Figure 7.8(c) shows three temporal profiles taken at 0, 5 and 10 mm in Fig. 7.8(b). Finally, Fig. 7.8(d) depicts the associated frequency distributions with in the inset the phase distributions. The THz ionization probability in Fig. 7.8(a) has a much more narrow spatial distribution than is observed with the bolometer or simulation. Propagation of the THz beam has large effects on the pulse shape. High-frequency components are mainly located in the center of the THz beam, while low-frequency components have a strong divergence and diffract from the beam center[197]. As a result, the simulated spatiotemporal profile seems to consist off-center of two wavefronts. Our simulations agree well with experimental results of Reiten et al.[57]. He used time-resolved measurements of a freely propagating THz beam. Off-center, large losses of high- and low-frequency components are observed in our simulations leading to multiple oscillations after the main pulse in Fig. 7.8(c) and to modified frequency distributions in Fig. 7.8(d). In the center of the beam, the spectrum resembles an unaffected THz pulse as has been presented in Fig. 7.1(b). We conclude that appearance of the second wavefront suppresses ionization. We note that the whole pulse still is shorter than the electron round trip time; the second pulse apparently de-excites the electron. In a similar way, the long slow tail of an HCP was found to suppress the ionization rate for very high Rydberg states $\gg 70$[201,202].

Figure 7.9(a) depicts the center line profile of an obstructed THz beam by a 9 mm wide aluminum plate at 100 mm from the Rydberg photocathode. Again, the bolometer measurements differ from the Rydberg camera images, but agree with the diffraction calculations. Remarkable is the relatively high ionization probability of the THz beam right behind the obstacle. Figure 7.9(c) shows that diffraction reconstructs behind the obstacle (at 0 mm) a pulse with a nearly half-cycle temporal structure and a frequency distribution quite similar to an unipolar THz pulse (Fig. 7.9(d)). Off-center at 5 and 10 mm, due to propagation effects, a second wavefront is observed, 7.9(b) and multiple low-amplitude oscillations arise after the main pulse, Fig. 7.9(c). The frequency distributions in Fig. 7.9(d) have lost high- as well as low-frequency

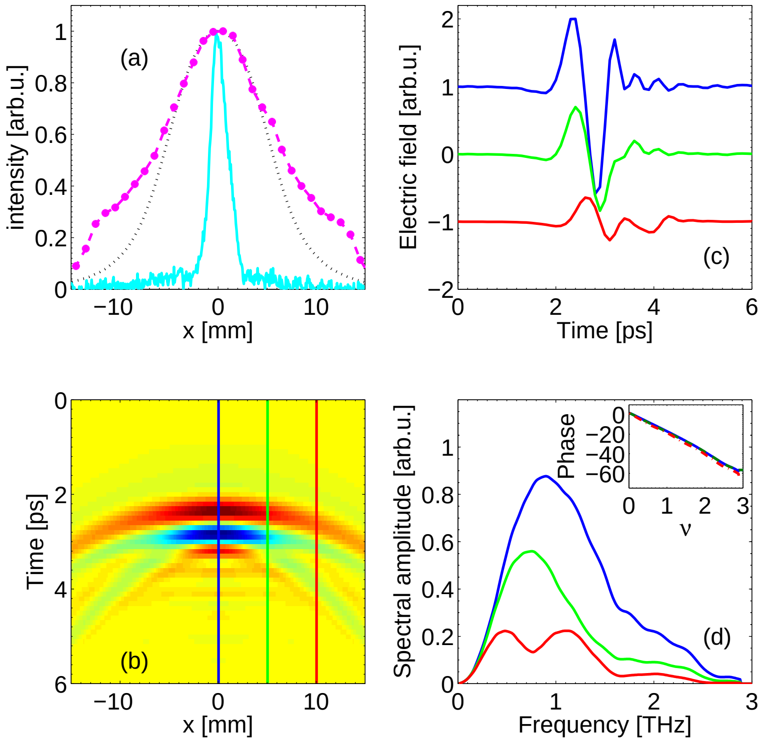

**Figure 7.8:** (a) Single line profile from the center of an unobstructed THz beam after propagating 300 mm for measurements with the Rydberg camera (solid) and bolometer (•), and simulations (dotted). (b) Simulated spatiotemporal profile. (c) Simulated temporal profile and (d) frequency distributions of cross sections at 0, 5 and 10 mm from (b) with in the inset the phase distributions.

components. Again, the appearance of a second wavefront suppresses the ionization probability off-center.

In Fig. 7.10(a), the center line profile of an obstructed THz beam by an obstacle at 200 mm from the Rydberg photocathode is shown. Also here, signal is observed behind the aluminum plate. The measured and calculated intensity has decreased as the obstacle is placed closer to the emitter. The bolometer detector measures more signal right behind the obstacle than predicted by model calculations. This difference is attributed mostly to experimental difficulties. The results in Fig. 7.9 and 7.10 agree qualitatively. Also in this situation, the second wavefront may suppress the ionization probability significantly off-center. The measured high ionization probability in the center is not easily explained by the apparent FCP nature.

Clearly, ionization probability and THz energy are not trivially related. The ionization is a highly nonlinear process that depends on pulse form rather than on electric field strength. Fig. 7.11(a) shows the large difference in response of the bolometer and the Rydberg camera. The relative ionization probability differs by an order of magnitude even resulting in an image only behind the obstacle. The relative ionization probability at $x = 0$ mm is enhanced in the case of an obstacle in comparison to an unobstructed beam. Diffraction reconstructs a pulse behind the object that is better suited for ionization. While further analyzing these results, we found that the

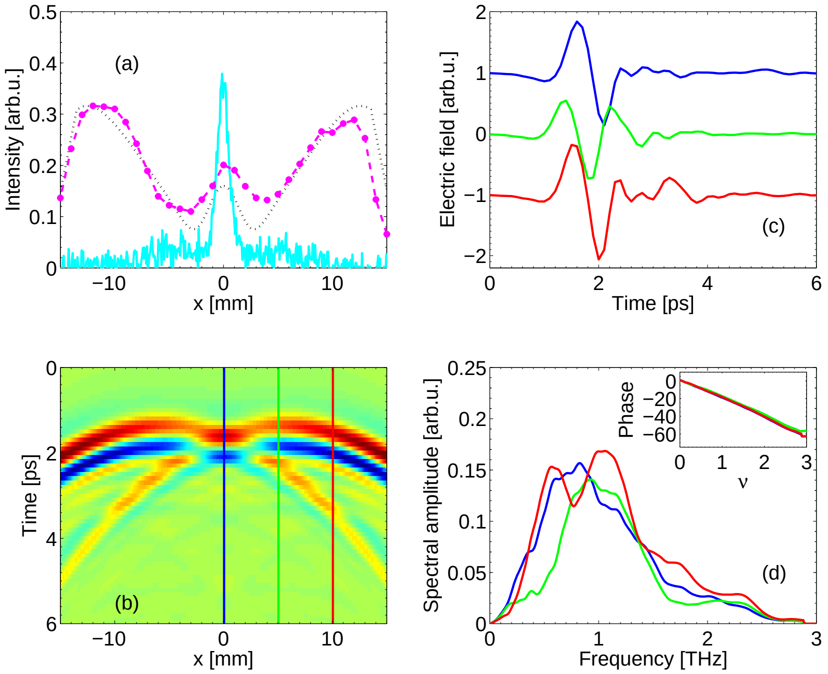

**Figure 7.9:** (a) Single line profile from the center of an obstructed THz beam by a 9 mm opaque obstacle at 100 mm from the Rydberg photocathode for measurements with the Rydberg camera (solid) and bolometer (●), and simulations (dotted). (c) Simulated temporal profile and (d) frequency distributions of cross sections at 0, 5 and 10 mm from (b) with in the inset the phase distributions.

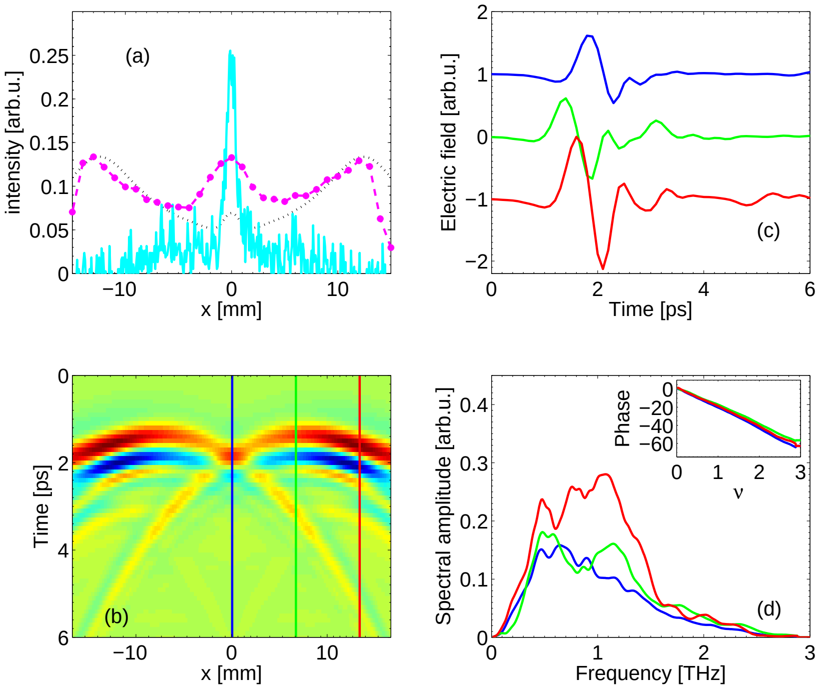

**Figure 7.10:** (a) Single line profile from the center of an obstructed THz beam by a 9 mm opaque obstacle at 200 mm from the Rydberg photocathode for measurements with the Rydberg camera (solid) and bolometer (●), and simulations (dotted). (c) Simulated temporal profile and (d) frequency distributions of cross sections at 0, 5 and 10 mm from (b) with in the inset the phase distributions.

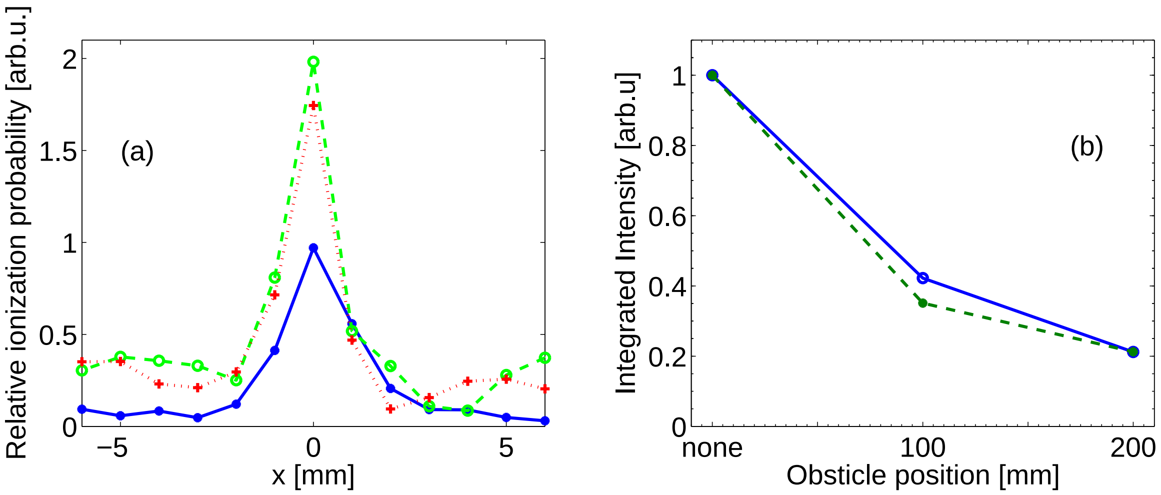

**Figure 7.11:** (a) Relative spatial ionization probability of the THz beam (with respect to the measured bolometer intensity) for an unobstructed (solid) and obstructed THz beam at 100 mm (dotted) and 200 mm (dashed). (b) Integrated intensity of the bolometer (solid) and the integrated ionization of the Rydberg camera (dashed) for a freely propagating and obstructed THz beam at 100 mm and 200 mm.

spatially integrated THz intensity decreases linearly with the integrated ionization probability, which should be fortuitous (see Fig. 7.11(b)).

### 7.5.2 Transparent obstacle

The remarkable behavior of the camera, when using coherent THz radiation, inspired us to search for other effects upon minor beam modification. Here, we present a large effect on the ionization when transmitting a THz beam partially through a high density polyethylene (HDPE) plate of 4 mm thick, that is highly transparent in the far-infrared. The emitter is situated 300 mm in front of the Rydberg photocathode and the HDPE plate, covering different portions of the THz beam, is placed halfway. Fig. 7.12(a) shows the integrated ionization yield (solid) of images that all contain the characteristic 4 mm wide spot. To our surprise, when covering 50% of the THz beam ionization of the Rydberg atoms disappears. Covering 80% of the beam induces an increase of the ionization yield with a factor 2.5. The spatially integrated intensity distribution (dashed), measured with the bolometer, does not reveal any of these large effects. HDPE absorbs about 25% of the THz radiation. The spatially resolved measurements with the bolometer in Fig. 7.12(b) show that the HDPE plate reduces and displaces the spatial intensity distribution. These distributions can not explain the large variation in ionization probability. Therefore, diffraction calculations were performed to simulate the effect of partially covering the THz beam with a HDPE plate.

In Fig. 7.13(a), the simulated (dashed) and the measured bolometer (solid) intensity distribution are depicted for covering 50% of the THz beam, where no ionization was observed. The simulated spatiotemporal profile in Fig. 7.13(b) shows two or more wavefronts for all positions $x$ as half of the THz beam is time delayed by the

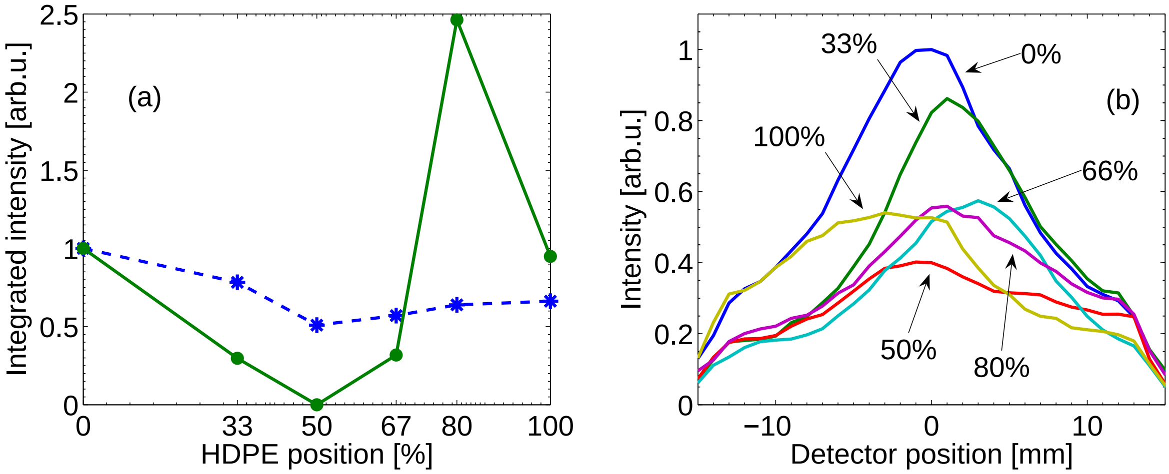

**Figure 7.12:** (a) Integrated ionization yield of the Rydberg camera (●) and intensity of the bolometer ($*$) for covering 0%, 33%, 50%, 66%, 80%, 100% of the THz beam. The Rydberg camera observes a large increase covering 80% and zero ionization covering 50%. (b) Linear measurements of the bolometer for covering different portions of the THz beam.

HDPE plate. We stress, that suppression of ionization occurs also in the center of our photocathode when the pulse shape shows multiple oscillations. The line profiles at $x$ = -5, 0 and 5 mm in Fig. 7.8(b) are depicted as temporal profiles in Fig. 7.8(c). The associated frequency distribution with in the inset the phase distribution are given in Fig. 7.8(d). Both wavefront have comparable field strengths. The interference at the observation plane of the two wavefronts results in a frequency distribution that contains a fringe pattern with frequencies present and absent. An analogy exists with the fringe patterns from two time-delayed pulses as used in Chapter 3 (frequency distribution illustrated in Section 1.5). The phase distribution in the inset shows a significant change at -5 mm, which corresponds to the location of the HDPE plate.

The second large effect using the HDPE plate is the enhanced ionization, when covering 80% of the THz beam. Analysis of the spatiotemporal profile (Fig. 7.14(b)) and selected temporal profiles (Fig. 7.14(c)) reveals that the high ionization is parallelled by an absence of large multiple oscillations after the main pulse. The observed wavefront in front and after the main pulse is very weak as can be seen in Fig. 7.14(c). Diffraction and propagation effects reconstruct at x = 0 a THz pulse with a nearly Gaussian shaped frequency distribution (see Fig. 7.14(d)). The associated temporal pulse is a nearly bandwidth limited pulse with, apparently, a high ionization probability. However, the large enhancement of the ionization yield, due to this reshaping process, remains surprising.

Summarizing, optical elements as well as propagation modify greatly the temporal structure of THz radiative patterns. Asymmetric pulse shapes evolve in other waveforms, often giving rise to multiple wavefronts. We find in all cases that the occurrence of multiple wavefront in simulations is consistent with the suppression of ionization of Rydberg atoms in the photocathode experimentally. Even though the amplitudes in the different wavefronts are often weak, the effect on the ionization is considerable. We note that the quality of the simulations depends on the initial conditions that describe

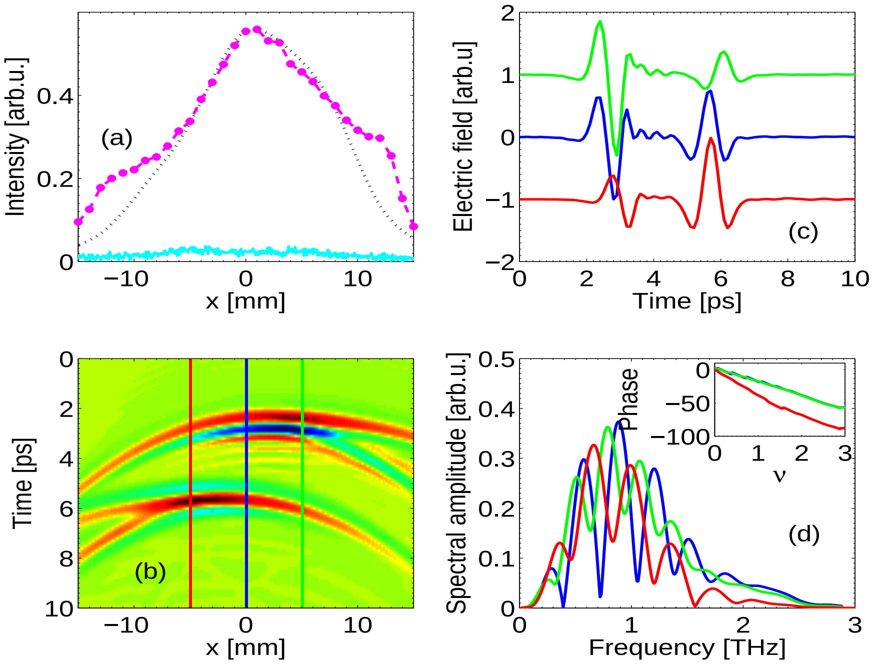

**Figure 7.13:** (a) Center single line profile from the Rydberg camera image (solid), the measured bolemeter (•) and simulated (dotted) intensity distribution for covering 50% of the THz beam with a transparent HDPE plate. (b) Simulated spatiotemporal profile. (c) Simulated temporal profile and (d) frequency distributions of cross sections at -5, 0 and 5 mm from (b) with in the inset the phase distributions.

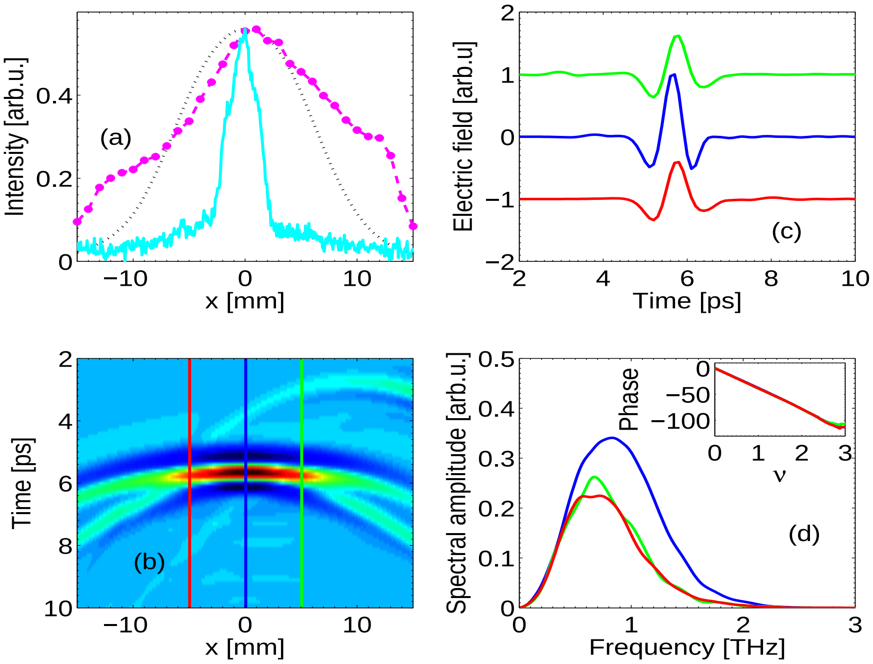

**Figure 7.14:** (a) Center single line profile from the Rydberg camera image (solid), the measured bolemeter (solid) and simulated (dashed) intensity distribution for covering 80% of the THz beam with a transparent HDPE plate. (b) Simulated spatiotemporal profile. (c) simulated temporal profile and (d) frequency distributions of cross sections at -5, 0 and 5 mm from (b) with in the inset the phase distributions.

the radiative pattern from the emitter. The input of the simulations is based on pulse forms measured with THz time domain spectroscopy (THz-TDS) containing a ZnTe emitter, which is assumed to resemble pulses from a GaAs wafer. The properties of the THz radiation in the interaction with Rydberg atoms result in a camera that is highly nonlinear and not well suited for imaging applications. We stress that the ultrashort nature of coherent THz radiation is responsible. As mentioned, ionization by ultrashort THz radiation is nonlinear, each frequency component has insufficient energy for ionization to occur. The coherent superposition of all frequency components provides the instantaneous electric field strength for the momentum kick. However, Ducas and Kleppner[164] has shown that our camera would be perfectly linear upon the use of narrow band FIR radiation in the absence of saturation. We observe here that changes in THz pulse shapes have large effects on the interaction with Rydberg electrons. In Chapter 4 of this thesis, we have encountered an example in which narrow band absorption gives rise to very weak semi-monochromatic transients behind the main pulse, which drive large population changes in multi-level systems. In the present experiments, the use of obstacles splits the THz wave front. It is a challenge to generate situations, in which the time delay between the wavefronts results in a constructive interference and an enhanced ionization. The experiments in Chapter 3 are an example of employing a time-delay in a Michelson interferometer for pulse shaping. In the case of THz radiation, frequency components diffract spatially from the THz beam and the bandwidth off-center becomes smaller. Also, this mechanism induces changes in pulse shapes and the associated electric field has multiple oscillations. As long as pulse shaping provides pulses that are short with respect to the Kepler orbit time of the Rydberg electron, weak oscillations behind the main pulse reverse the ionization. By many authors, this is called recombination[201,204].

## 7.6 Conclusions and outlook

The aim of our research was to develop a far-infrared camera optimized to image pulsed far-infrared sources that matches the exposure time of the Rydberg photocathode. As a light source, an ultrafast coherent THz source was chosen based on generation of charge carriers in a semiconductor with femtosecond pulses. We conclude that this broadband THz radiation is not a good far-infrared source for our Rydberg camera. The highly nonlinear ionization of the "half-cycle" THz pulses makes the interpretation of the obtained images with the Rydberg camera difficult. The ionization of Rydberg atoms in the photocathode depends on the THz pulse structure, rather than on the intensity in contrast to linear cameras. In the far-infrared wavelength regime, propagation, diffraction and refraction greatly affect the temporal THz pulse structure. Our observation that ionization only occurs behind an obstacle, instead of the remaining part of the THz beam, illustrates the large effects of subtle pulse shapes on ionization probability.

The various optical modifications of the THz beam, such as focussing, diffraction on obstacles and transmission through slabs of highly transparent HDPE, show that the ionization probability of a Rydberg atom is reduced considerably when pulse shaping leads to additional wavefronts i.e. oscillations within the classical orbit time of the Rydberg electron. Even, if the field strength of the extra oscillation is weak, the effect on the ”recombination” of the excited electron into the atom seems to be large. Our confidence in this conclusion stems from the combination of energy measurements with the bolometer and the favorable comparison of these measurements with diffraction and beam propagation calculations, and comparisons with the available literature.

The ideal future experiment would involve THz-TDS measurements to probe locally the THz temporal pulse structure in combination with bolometer measurements of the total energy and detection of Rydberg state ionization, Rydberg state excitation and de-excitation at the same position. These experiments are certainly feasible. In fact, most experiments on Rydberg atoms probed only locally the THz field by detecting ionized electrons though a small hole in extraction plates. A first step would be to reshape THz pulses to have multiple oscillations. Synthesis of such THz pulses is possible by tailoring the femtosecond pulse[176–181]. Gradually, the THz temporal pulse structure can be tuned from a single half-cycle to a multi-cycle pulse. It is expected that the ionization probability will vary significantly and will not only show suppression, but also enhancement.

We are convinced that our Rydberg camera can be used throughout the whole infrared spectrum when using more ”classical” narrow band FIR radiation with durations from nanoseconds up to a microsecond. The wavelength sensitivity of the Rydberg camera is continuously tuneable by choosing the principle quantum number $n$ of the Rydberg state in the photocathode and the strength of the external electric field. The Rydberg camera is a very sensitive camera capable of detecting coherent as well as incoherent radiation. The present estimations of the sensitivity of the Rydberg photocathode for the THz pulses shows that only a few nanoJoules of broadband THz energy is sufficient to create an image.

# Acknowledgments

This work is supported by the ”Stichting Technische Wetenschappen (STW)”, which is financially supported by the ”Nederlandse Organisatie voor Wetenschappelijk Onderzoek (NWO)”.

# Bibliography

1. F. Cajori, *History of physics* (Macmillan, 1898).
2. E. Hecht, *Optics, Thirth Edition* (Addison Wesley Longman, Inc, 1998).
3. R. A. Serway and R. J. Beichner, *Physics, for scientists and engineers with modern physics, Fifth Edition* (Harcort Collega Publishers, 2000).
4. B. H. Bransden and C. J. Joachain, *Quantum Mechanics, Second Edition* (Pearson Education Limited, 2002).
5. I. I. Rabi, J. R. Zacharias, S. Millman, and P. Kusch, Phys. Rev. **53**, 318 (1938).
6. N. F. Ramsey, Science **248**, 1612 (1990).
7. R. L. Fork, B. I. Greene, and C. V. Shank, Appl. Phys. Lett. **83**, 671 (1981).
8. R. L. Fork, . E. Martinez, and J. P. Gordon, Optics Lett. **9**, 150 (1984).
9. R. L. Fork, C. H. B. Cruz, P. C. Becker, and C. V. Shank, Opt. Lett. **12**, 483 (1987).
10. J.-C. Diels and W. Rudolph, *Ultrashort Laser Pulse Phenomena, Second Edition* (Elsevier inc., 2006).
11. P. M. Paul, E. S. Toma, P. Breger, G. Mullot, F. Augé, P. Balcou, H. G. Muller, and P. Agostini, Science **292**, 1689 (2001).
12. S. A. Aseyev, Y. Ni, L. J. Ni, H. G. Muller, and M. J. J. Vrakking, Phys. Rev. Lett. **91**, 223902 (2003).
13. M. van Exter and D. Grischkowsky, IEEE Transactions on Microwave Theory and Techniques **38**, 1684 (1990).
14. H. Harde and D. Grischkowsky, J. Opt. Soc. Am. B **8**, 1642 (1991).
15. X. C. Zhang and D. H. Auston, J. Appl. Phys. **71**, 326 (1992).
16. P. U. Jepsen, R. H. Jacobsen, and S. R. Keiding, J. Opt. Soc. Am. B **13**, 2424 (1995).
17. P. U. Jepsen, R. Jacobseb, and S. Keiding, J. Opt. Soc. Am. B **3**, 2424 (1996).
18. M. Shapiro and P. Brumer, *Principle of the Quanutum Control of Molecular Processes* (Wiley, 2002).
19. R. A. Bartels, *Coherent Control of Atoms and Molecules* (The University of Michigan, 2002).
20. D. Meshulach and Y. Silberberg, Phys Rev. A **60**, 1287 (1999).
21. W. S. Warren, H. Rabitz, and M. Dahleh, Science **259**, 1581 (1993).
22. H. Rabitz, R. de Vivie-Riedle, M. Motzkus, and K. Kompa, Science **288**, 824 (2000).
23. T. Baumert, J. Helbing, and G. Gerbert, Adv. Chem. Phys. **101**, 47 (1997).
24. M. Dantus, M. J. Rosker, and A. H. Zewail, J. Chem. Phys. **89**, 6128 (1988).
25. P. Brumer and M. Shapiro, Chem. Phys Lett. **126**, 541 (1986).
26. C. Chen, Y. Yin, and D. S. Elliot, Phys. Rev. Lett. **64**, 507 (1990).

27. S. Lu, S. M. Park, and Y. Xie, J. Chem. Phys. **96**, 6613 (1992).
28. L. Zhu, V. Kleinman, X. Li, S. Lu, K. Trentelman, and R. J. Gordon, Science **270**, 77 (1995).
29. V. Kleinman, L. Zhu, X. Li, and R. J. Gordon, J. Chem. Phys. **102**, 5863 (1995).
30. V. Kleinman, L. Zhu, J. Allen, and R. J. Gordon, J. Chem. Phys. **103**, 10800 (1995).
31. E. Dupont, P. B. Corkum, H. Liu, M. Buchanan, and Z. Wasilewski, Phys. Rev. Lett. **74**, 3596 (1995).
32. S. Schiemann, A. Kuhn, S. Steuerwald, and K. Bergmann, Phys. Rev. Lett. **71**, 3637 (1993).
33. D. J. Tannor, R. Kosloff, and S. A. Rice, J. Chem. Phys. **85**, 5805 (1986).
34. T. Baumert, M. Grosser, R. Thalweiser, and G. Gerber, Phys. Rev. Lett. **67**, 3753 (1991).
35. E. D. Potter, J. L. Herek, S. Pederson, Q. Liu, and A. H. Zewail, Nature **355**, 66 (1992).
36. T. Baumert and G. Gerber, Isr. J. Chem. **34**, 103 (1994).
37. A. H. Zewail, The Nobel Foundation **December 9** (1999).
38. D. Marcuse, Applied Optics **19**, 1653 (1980).
39. A. M. Weiner, D. E. Learid, J. S. Patel, and J. R. Wullert, J. Quantum Electron. **28**, 908 (1992).
40. A. M. Weiner, Rev. Sci. Instrum. **71**, 1929 (2000).
41. R. S. Judson and H. Rabitz, Phys. Rev. Lett. **68**, 1500 (1992).
42. C. J. Bardeen, V. V. Yakovlev, K. R. Wilson, S. D. Carpenter, P. M. Weber, and W. S. Warren, Chem. Phys. Lett. **280**, 151 (1997).
43. A. Assion, T. Baumert, M. Bergt, T. Brixner, B. Kiefer, V. Seyfried, M. Strehle, and G. Gerber, Science **282**, 919 (1998).
44. T. C. Weinacht, J. Ahn, and P. H. Bucksbaum, Nature **397**, 233 (1999).
45. T. Hornung, R. Meier, D. Zeidler, K.-L. Kompa, D. Proch, and M. Motzkus, Appl. Phys. B **71**, 277 (2000).
46. R. Bartels, S. Backus, E. Zeek, L. Misoguti, G. Vdovin, I. P. Christov, M. M. Murnane, and H. C. Kapteyn, Nature **406**, 164 (2000).
47. R. Bartels, S. Backus, I. Christov, H. Kapteyn, and M. Murnane, Chem. Phys. **267**, 277 (2001).
48. J. L. Herek, W. Wohlleben, R. J. Cogdell, D. Zeidler, and M. Motzkus, Nature **417**, 533 (2002).
49. A. Gürtler, *Rydberg atoms in low-frequency fields : fundamental aspects and applications* (Katholieke Universiteit Nijmegen, 2003).
50. R. R. Jones, D. You, and P. H. Bucksbaum, Phys. Rev. Lett **70**, 1236 (1993).
51. A. Wetzels, A. Gürtler, L. D. Noordam, F. Robicheaux, C. Dinu, H. Muller, M. J. J. Vrakking, and W. J. van der Zande, PRL **89**, 273003 (2002).
52. C. Raman, C. W. S. Conover, C. I. Sukenik, and P. H. Bucksbaum, Phys. Rev. Lett. **76**, 2436 (1996).
53. C. Reinhold, M. Melles, H. Shao, and J. Burgdorfer, J. Phys. B: At Mol. Opt phys **26**, L659 (1993).
54. D. You and P. H. Bucksbaum, JOSA B **14**, 1651 (1997).
55. S. Feng, H. G. Winful, and R. W. Hellwarth, Phys. Rev. E. **59**, 4630 (1999).
56. A. Bitzer, M. Walther, A. Kern, S. Gorenflo, and H. Helm, APL **90**, 71112 (2007).
57. M. T. Reiten, S. A. Harmon, and R. A. Cheville, J. Opt. Soc. Am. B **20**, 2215 (2003).
58. A. Bugacov, B. Piraux, M. Pont, and R. Shakeshaft, Phys. Rev. A **51**, 1490 (1995).
59. F. Robicheaux, Phys. Rev. A **56**, R3358 (1997).
60. B. Broers, L. D. Noordam, and H. B. van Linden van den Heuvell, Phys. Rev. Lett.

**69**, 2062 (1992).

61. M. Shapiro, J. Phys. Chem. p. 7396 (1993).
62. N. Dudovich, B. Dayan, S. M. G. Faeder, and Y. Silberberg, Phys. Rev. Lett. **86**, 47 (2001).
63. H. B. Bebb and A. Gold, Phys. Rev **143**, 143 (1966).
64. A. M. Weiner, D. E. Leaird, G. P. Wiederrecht, and K. A. Nelson, J. Opt. Soc. Am. B **8**, 1264 (1991).
65. A. S. Meijer, A. Gijsbertsen, Y. Zhang, D. H. Parker, M. J. J. Vrakking, and W. J. van der Zande, Phys Rev. A. **76**, 023411 (2007).
66. R. D. Levine, *Reaction Dynamics* (Cambridge University Press, Cambridge, 2005).
67. M. J. L. de Lange, M. Drabbels, P. T. Griffiths, J. Bulthuis, and J. G. Snijders, Chem. Phys. Lett. **313**, 491 (1999).
68. D. Zeidler, A. Staudte, A. B. Bardon, D. M. Villeneuve, R. Dorner, and P. B. Corkum, Phys. Rev. Lett. **95**, 203003 (2005).
69. J. Itatani, J. Levesque, D. Zeidler, H. Niikura, H. Pèpin, J. C. Kieffer, P. B. Corkum, and D. M. Villeneuve, Nature **432**, 867 (2004).
70. G. Scoles, ed., *Atomic and Molecular Beams Methods Vol. 14* (Oxford University Press, New York/Oxford, 1988).
71. H. G. Bennewitz, W. Paul, and C. Schlier, Z. Phys. **141**, 6 (1955).
72. A. Gijsbertsen, H. Linnartz, G. Rus, A. E. Wiskerke, S. Stolte, D. W. Chandler, and J. Kłos, J. Chem. Phys. **123**, 224305 (2005).
73. T. P. Rakitzis, A. J. van den Brom, and M. H. M. Janssen, Science **303**, 1852 (2004).
74. H.-L. Dai and R. W. Field, eds., *Molecular dynamics and spectroscopy by stimulated emission pumping* (World Scientific Publishing Co., Singapore, 1995).
75. F. F. Crim, Annu. Rev. Phys. Chem. **44**, 397 (1993).
76. F. F. Crim, J. Phys. Chem. **100**, 12725 (1996).
77. A. C. Kummel, G. O. Sitz, and R. N. Zare, J. Chem. Phys. **85**, 6874 (1986).
78. U. Gaubatz, P. Rudecki, S. Schiemann, and K. Bergmann, J. Chem. Phys. **92**, 5363 (1990).
79. S. Schiemann, A. Kuhn, S. Steuerwald, and K. Bergmann, Phys. Rev. Lett. **71**, 3637 (1993).
80. B. Broers, L. D. Noordam, and H. B. van Linden van den Heuvell, Phys. Rev. A. **46**, 2749 (1992).
81. J. K. Ranka, R. W. Schirmer, and A. L. Gaeta, Phys. Rev. A. **57**, R36 (1998).
82. N. Dudovich, D. Oron, and Y. Silberberg, Phys. Rev. Lett. **88**, 123004 (2002).
83. H. Stapelfeld and T. Seideman, Rev. Mod. Phys. **75**, 543 (2003).
84. M. J. Vrakking and S. Stolte, Chem. Phys. Lett **271**, 209 (1997).
85. F. Rosca-Pruna and M. J. J. Vrakking, Phys. Rev. Lett. **87**, 153902 (2001).
86. F. Lepine, M. Kling, Y. Ni, J. Khan, O. Ghafäur, T. Martchenko, E. Gustafsson, P. Johnsson, K. Varju, T. Remetter,, J. Modern Optics **54**, 953 (2006).
87. J. P. Heritage, T. K. Gustafson, and C. H. Lin, Phys. Rev. Lett. **34**, 199 (1975).
88. C. H. Lin, J. P. Heritage, T. K. Gustafson, R. Chiao, and J. McTague, Phys. Rev. A. **13**, 813 (1976).
89. M. Morgen, W. Price, L. Hunziker, P. Ludowsie, M. Blackwell, and Y. Chen, Chem. Phys. Lett. **209**, 1 (1993).
90. T. Seideman, Phys. Rev. Lett. **83**, 4971 (1999).
91. P. M. Felker and A. H. Zewail, Adv. Chem. Phys. **70**, 265 (1988).
92. N. G. Kalugin and Y. V. Rostovtsev, Opt. Lett. **31**, 969 (2006).
93. A. Nazarkin and G. Korn, Phys. Rev. A. **58**, R61 (1998).
94. N. L. Wagner, E. A. Gibson, T. Popmintchev, I. P. Christov, M. M. Murnane, and

H. C. Kapteyn, Phys. Rev. Lett. **93**, 173902 (2004).

95. H. Hasegawa and Y. Ohshima, Phys. Rev. A **74**, 061401(R) (2006).
96. D. Oron, N. Dudovich, D. Yelin, and Y. Silberberg, Phys. Rev Lett. **88**, 063004 (2002).
97. G. Herzberg, *Molecular Spectra and Molecular Structure, Vol. 1 , Spectra of Diatomic Molecules*, Van Nostrand and Reinhold Company, New York **Vol.1** (1960).
98. R. N. Zare, *Angular Momentum: Understanding spatial aspects in chemisty*, (John Wiley and Sons, New York (1988)).
99. J. M. Holas, *Angular Momentum: Understanding spatial aspects in chemisty and physics Spectroscopy, Third Edition*, Krieger Publishing Co Modern Malabar (1996).
100. C. Amiot, J. Mol. Spectrosc. **94**, 150 (1982).
101. F. Rasetti, Phys. Rev. **34**, 367 (1929).
102. J. M. Brown, J. T. Hougen, K. P. Huber, I. K. J. W. C. Johns, H. Lefebvre-Brion, A. J. Merer, D. A. Ramsay, J. Rostas, and R. N. Zare, J. Mol. Spectrosc. **55**, 500 (1975).
103. B. Friedrich and D. Herschbach, J. Phys. Chem. **99**, 15686 (1995).
104. B. Friedrich and D. Herschbach, J. Phys. Chem. A **103**, 10280 (1999).
105. N. J. Bridge and A. D. Buckingham, Proc. Roy. Soc. A. **295**, 75 (1966).
106. T. Seideman, J. Chem. Phys. **103**, 7887 (1995).
107. M. J. J. Vrakking, D. M. Villeneuve, and A. Stolow, Phys. Rev. A **54**, R37 (1996).
108. F. Rosca-Pruna, E. Springate, H. L. Offerhaus, M. Krishnamurthy, N. Farid, C. Nicole, and M. J. J. Vrakking, J. Phys. B: At. Mol. Opt. Phys **34**, 4919 (2001).
109. E. Springate, F. Rosca-Pruna, H. L. Offerhaus, M. Krishnamurthy, and M. J. J. Vrakking, J. Phys. B: At. Mol. Opt. Phys **34**, 4934 (2001).
110. M. Shapiro and P. Brumer, J. Chem. Phys. **84**, 4103 (1986).
111. D. J. Tannor and S. A. Rice, J. Chem. Phys. **83**, 5013 (1985).
112. A. M. Weiner, Prog. Quantum Electron. **19**, 161 (1995).
113. C. W. Hillegas, J. X. Tull, D. Goswami, D. Strickland, and W. S. Warren, Opt. Lett **19**, 737 (1994).
114. D. Gowswami, Physics Reports **374**, 385 (2003).
115. J. Degert, W. Wohlleben, B. Chatel, M. Motzkus, and B. Girard, Phys. Rev. Lett. **89**, 203003 (2002).
116. C. Petersen, E. Péronne, J. Thögersen, H. Stapelfeldt, and M. Machholm, Phys Rev. A **70**, 33404 (2004).
117. T. Brixner, N. H. Damrauer, G. Krampert, P. Niklaus, and G. Gerber, J. Opt. Soc. Am. B **20**, 878 (2003).
118. T. Martchenko, C. Siedschlag, S. Zamith, H. G. Muller, and M. J. J. Vrakking, Phys. Rev. A **72**, 053202 (2005).
119. M. D. Crisp, Phys Rev. A **1**, 1604 (1970).
120. S. L. McCall and E. L. Hahn, Phys. Rev. **183**, 457 (1969).
121. J. E. Rothenberg, D. Grischkowsky, and A. C. Balant, Phys. Rev. Lett. **53**, 552 (1984).
122. U. Kallmann, S. Brattke, and W. Hartmann, Phys Rev. A **59**, 814 (1999).
123. J. K. Ranka, R. W. Schirmer, and A. L. Gaeta, Phys. Rev. A. **57**, R36 (1998).
124. N. Dudovich, D. Oron, and Y. Silberberg, Phys Rev. Lett **88**, 123004 (2002).
125. A. Gürtler and W. J. van der Zande, Phys Rev. Lett. **93**, 153002 (2004).
126. A. Präkelt, M. Wollenhaupt, A. Assion, C. Horn, C. Sarpe-Tudoran, M. Winter, and T. Baumert, Rev. Sci. Instr. **74**, 4950 (2003).
127. N. Dudovich, D. Oron, and Y. Silberberg, Phys Rev. Lett **92**, 103003 (2004).
128. A. V. Kimel, A. Kirilyuk, P. A. Usachev, R. V. Pisarev, A. M. Balbashov, and T. Rasing, Nature **435**, 655 (2005).
129. C. D. Stanciu, F. Hansteen, A. V. Kimel, A. Kirilyuk, A. Tsukamoto, A. Itoh, and T. Rasing, Phys. Rev. lett. **90**, 047601 (2007).

130. M. Walther, B. Fischer, M. Schall, H. Helm, and P. U. Jepsen, Chem. Phys. Lett **332**, 389 (2000).
131. D. M. Leitner, M. Havenith, and M. Gruebele, Intl. Reviews in Physical Chemistry **25**, 553 (2006).
132. M. C. Nuss, D. H. Auston, and F. Capasso, Phys. Rev. Lett. **22**, 2355 (1987).
133. M. C. Beard, G. M. Turner, and C. A. Schmuttenmaer, NANO LETTERS **2**, 983 (2002).
134. E. Hendry, J. Schins, L. P. Candeias, L. D. A. Siebbeles, and M. Bonn, Phys. Rev. Lett. **92**, 196601 (2004).
135. N. Nagai, M. Sumitomo, M. Imaizumi, and R. Fukasawa, Semicond. Sci. Technol. **21**, 201 (2006).
136. A. Nahata, A. S. Weling, and T. F. Heinz, Appl. Phys. Lett. **69**, 2321 (1996).
137. P. C. M. Planken, H. K. Nienhuys, H. J. Bakker, and W. T. Wenckebach, J. Opt. Soc. Am. B **18**, 313 (2001).
138. K. Liu, J. Xu, and X.-C. Zhang, Appl. Phys. Lett. **85**, 863 (2004).
139. A. Wetzels, A. Gürtler, H. Muller, and L. Noordam, Eur. Phys. J. D **14**, 157 (2001).
140. T. Yasui, E. Saneyoshi, and T. Araki, Appl. Phys. Lett. **87**, 061101 (2005).
141. Z. Jiang and X.-C. Zhang, App. Phys. Lett. **72**, 1945 (1998).
142. J. Shan, A. S. Weling, E. Knoesel, L. Bartels, M. Bonn, A. Nahata, G. A. Reider, and T. F. Heinz, Opt. Lett. **25**, 426 (2000).
143. N. Acquista and E. Plyer, JOSA **43**, 977 (1953).
144. J. A. Harrington, Appl. Opt. **27**, 3097 (1988).
145. H. Rubens and G. Hertz, Berlin **14**, 256 (1912).
146. R. Stolen and K. Dransfeld, Phys. Rev. **139**, 1295 (1956).
147. A. D. Woods, W. Cochran, and B. N. Brockhouse, Phys. Rev **119**, 980 (1960).
148. L. A. Vredevoet, Phys. Rev. **140**, 930 (1965).
149. E. R. Cowley and R. A. Cowley, Proceedings of the Royal Society of London. Series A, Mathematical and Physical Sciences **287**, 1409 (1965).
150. G. D. Mahan, Phys. Rev. B **41**, 10808 (1990).
151. D. R. Bosomworth, Phys. Rev. **157**, 157 (1967).
152. H. H. Li, J. Phys. Chem. Ref. Data **5**, 329 (1976).
153. P. U. Jepsen and B. Fischer, Opt. Lett. **30**, 29 (2005).
154. H. H. Li, Int. J. Thermophys **1**, 79 (1979).
155. M. C. Beard, G. M. Turner, and C. A. Schmuttenmaer, J. Phys. Chem. B **106**, 7146 (2002).
156. S. Biber, M. Bozzi, O. Guenther, L. Perregrini, and L.-P. Schmidt, IEEE Trans. Antennas Propag. **54**, 2638 (2005).
157. R. Rungsawang, Y. Ueno, and K. Ajito, Anal. Sci. **23**, 917 (2007).
158. J. Zhang and D. Grischkowsky, J. Phys. Chem. B. **108**, 18590 (2004).
159. J. Zhang and D. Grischkowsky, Opt. lett. **29**, 1031 (2004).
160. M. J. Golay, Rev. Sci. Instr. **20**, 816 (1949).
161. E. E. Becklin, SPIE conference proceedings **492**, 3356 (1998).
162. P. de Maagt, ESA **Startiger Team** (2003).
163. Proxitronic, *Image Intensifiers Data sheet* (Proxitronic Funk GmbH and Co. KG, Bensheim Germany, 2007).
164. T. W. Ducas, W. P. Spencer, A. G. Valdyanathan, W. H. Hamilton, and D. Kleppner, APL **35**, 382 (1979).
165. H. Figger, G. Leuchs, R. Straubinger, and H. Walther, OPtics Commun **33**, 37 (1980).
166. M. Drabbels and L. D. Noordam, Optics Lett. **22**, 1436 (1997).
167. G. M. Lankhuijzen, M. Drabbels, F. Robicheaux, and L. D. Noordam, Phys. Rev. A

**57**, 440 (1998).

168. M. Drabbels and L. D. Noordam, APL **29**, 1797 (1999).
169. *Simion(TM) version 6.00* (Scientific Instrument Services, 1995).
170. A. Adams and F. H. Read, J. Phys. E. **5**, 150 (1972).
171. D. W. O. Heddle, J. Phys. E: Sci. Instrum. **2**, 1046 (1969).
172. T. F. Gallagher, *Rydberg Atoms* (Cambridge University Press, Cambridge UK, 1994).
173. W. Li, I. Mourachko, M. W. Noel, and T. F. Gallagher, Phys. Rev. A **67**, 052502 (2003).
174. J. H. Hoogenraad and L. D. Noordam, Phys. Rev. A **57**, 4533 (1998).
175. H. Yukawa, *Tabibito (The Traveler)* (World Scientific Pub Co Inc, 1982).
176. A. S. Weling, B. B. Hu, N. M. Froberg, , and D. H. Auston, Appl. Phys. Lett. **64**, 137 (1994).
177. C. Messner, M. Sailer, H.Kostner, and R. Höpfel, Phys. Rev. B **64**, 619 (1997).
178. J. Y. Sohn, Y. H. Ahn, D. J. Park, E. Oh, , and D. S. Kim, Appl. Phys. Lett. **81**, 13 (2002).
179. J. Ahn, A. V. Efimov, R. D. Averitt, and A. J. Taylor, OSA **11**, 2486 (2003).
180. R. Yano, H. Gotoh, Y. Hirayama, T. Hattori, and S. Miyashita, Chem. Phys **326**, 577 (2006).
181. I. M. Minwoo Yi, Kang Hee Lee, J.-H. Son, R. D. Averitt, and J. Ahn, Jpn. J. Appl. Phys. **47**, 2002 (2008).
182. A. Gürtler, A. S. Meijer, and W. J. van der Zande, APL **83**, 222 (2003).
183. D. You, R. R. Jones, P. H. Bucksbaum, and D. R. Dykaar, Opt. Lett **18**, 290 (1993).
184. G. Zao, R. Schouten, N. v. d. Valk, W. Wenkenbach, and P. C. M. Planken, Rev. Sci. Instrum. **73**, 1715 (2002).
185. O. Imafuji, B. P. Singh, Y. Hirose, Y. Fukushima, and S. Takigawa, Appl. Phys. Lett. **91**, 071112 (2007).
186. H.-T. Chen, W. J. Padilla, J. M. O. Zide, A. C. Gossard, A. J. Taylor, and R. D. Averitt, Nature **444**, 597 (2006).
187. J. Kröll, J. Darmo, S. S. Dhillon, X. Marcadet, M. Calligaro, C. Sirtori, and K. Unterrainer, Nature **449**, 698 (2007).
188. J. Pijpers, E. Hendry, M. Milder, R. Fanciulli, J. Savolainen, J. Herek, D. Vanmaekelbergh, S. Ruhman, D. Mocatta, D. Oron,, J. Phys. Chem. C **111**, 4146 (2007).
189. C. Zandonella, Nature **424**, 721 (2003).
190. J. F. Federici, B. Schulkin, F. Huang, D. Gary, R. Barat, F. Oliveira, and D. Zimdars, Semicond. Sci. Technol. **20**, S266 (2005).
191. J. Darmo, V. Tamosiunas, G. Fasching, J. Kröll, K. Unterrainer, M. Beck, M. Giovannini, J. Faist, C. Kremser, and P. Debbage, OSA **12**, 1879 (2004).
192. Q. Wu, T. D. Hewitt, and X.-C. Zhang, APL **69**, 1026 (1996).
193. M. Usami, T. Iwamoto, R. Fukasawa, M. Tani, M. Watanabe, and K. Sakai, Phys. Med. Biol. **47**, 3749 (2002).
194. D. M. Mittleman, S. Hunsche, L. Boivin, and M. C. Nuss, Opt. Lett **22**, 904 (1997).
195. A. B. Ruffin, J. V. Rudd, J. F. Whitaker, S. Feng, and H. G. Winful, Phys. Rev. Lett. **83**, 3410 (1993).
196. R. W. Ziolkowski and J. B. Judkins, J. Opt. Soc. Am. A **11**, 2021 (1992).
197. A. Gürtler, C. Winnewisser, H. P. Helm, and P. U. Jepsen, J. Opt. Soc. Am. A **17**, 74 (2000).
198. A. Nahata and T. F. Heinz, IEEE J. Quantum Electron. **2**, 701 (1996).
199. J. Bromage, S. Radic, G. P. Agrawal, J. C. R. Stroud, P. M. Fauchet, and R. Sobolewski, Opt. Lett **22**, 627 (1997).
200. U. 1808 E. 17th Street, Tucson, *IR Labs inc.* (http://www.irlabs.com, 2008).

201. C. Wesdorp, F. Robicheaux, and L. D. Noordam, PRL **87**, 83001 (2001).
202. Tielking, N. E. Bensky, T. J., and R. R. Jones, Phys. Rev. A **51**, 3370 (1995).
203. M. C. Beard and C. A. Schmuttenmaer, J. Chem. Phys **15**, 2903 (2001).
204. D. Dimitrovski, E. A. Solovev, and J. S. Briggs, Phys. Rev. Lett. **93**, 083003 (2004).

# Summary

In this thesis, we will be concerned with the interaction of ultrafast pulses with rubidium (Rb) atoms and nitric oxide molecules (NO). The short pulse duration and the high peak intensity stress the importance of nonlinear processes. Moreover, according to the uncertainty principle ($\Delta E \Delta t \approx \frac{\hbar}{2}$), short pulses consist of many frequencies with all well defined phases that participate simultaneously in an excitation process. The availability of tools to experimentally control the spectral amplitude-, phase- and/or polarization of the ultrashort light pulses, provides the experimentalist with a large number of "control knobs", that allows for shaping the light pulse. As a consequence of pulse shaping, the transition rate to a final state is modified and interfering quantum mechanical pathways are controlled. The manipulation of quantum interferences is called "coherent control": the ability to steer a quantum mechanical reaction towards a desired final state through its interaction with light, while canceling out other paths leading to undesired outcomes. Coherently controlling quantum mechanical systems involves multiphoton excitation and multilevel systems. In many cases, the temporal electric field structure of the light pulse $\varepsilon(t)$ determines the transition rate to a final state rather than the intensity $|\varepsilon(t)|^2$. We studied the quantum mechanical interference in atoms and molecules for the fundamental understanding of the excitation process.

In experimental physics, often the first step is to limit the number of molecular quantum states involved in an experiment. Optical excitation with femtosecond pulses provides an alternative means for molecular quantum state preparation. We investigate in **Chapter 3** the process of femtosecond stimulated Raman (FSR) in molecular nitric oxide (NO) as a tool to selectively excite rotational levels. Within the bandwidth of the femtosecond pulse, each pair of photons with difference frequency $\omega_p - \omega_s$ equal to a rotational transition frequency $\omega_{J,J'}$ is able to excite a rotational state in NO. We use two identical femtosecond pulses with time delay $\Delta T$. The spectral distribution contains a fringe pattern with a fringe spacing $\Delta\omega_{fr} = 2\pi/\Delta T$. When a multiple of the fringe spacing matches the frequency of a rotational transition, $\Delta\omega_{fr} = n\omega_{J,J'}$, the FSR excitation probability has a maximum, since both photons necessary to drive this process are present in the spectral distribution. When the fringe period equals $\Delta\omega_{fr} = (n + \frac{1}{2})\omega_{J,J'}$, however, the transition amplitude has a minimum since at frequencies where the fringe pattern has a maximum, no suitable accompanying photons exist. An alternative view to the excitation action is that the first femtosecond pulse initiates a "phase clock" $\Delta\phi$ in the plane of excited NO molecules and depending on the time delay of the second pulse, constructive ($n\Delta T\omega_{J,J'} = \Delta\phi_{J,J'}$) or destructive interference ($(n+\frac{1}{2})\Delta T\omega_{J,J'} = \Delta\phi_{J,J'}$) populates or depletes specific rotational states. We measure quantum interferences with time delays up to 20 ps. From our results, we can conclude that one can selectively discriminate between two quantum mechanical pathways climbing the rotational ladder in NO, by choosing a particular time delay, $\Delta T$, between the two femtosecond pulses. The process of FSR is as a versatile tool to selectively excite dense samples of rotationally excited molecules.

The use of femtosecond pulses implies a wide range of frequencies which all participate in the excitation process. This results in a loss of spectral selectivity, since all the transitions within the bandwidth may be excited. We employ in **Chapter 4** "physics-inspired" tailoring mechanisms, like absorption in a gas, to manipulate the quantum interference in the three-level system of Rubidium (5s-5p-5d). We show that tailoring femtosecond pulses with narrow band absorption can selectively enhance or deplete excited state population in a multi-level system. Upon propagation through an absorbing gas, semi-monochromatic transient electric fields appear behind the main pulse. Causality forbids a pre-transient. The linear combination of a frequency-dependent phase and amplitude, according to the Kramers-Kronig dispersion, is programmed in the spatial light modulator of a pulse shaper to simulate absorption. In this way, we study separately the effects of power absorption and dispersion. Three sets of measurements are recorded; only-phase, only-amplitude and, both combined called absorption. We present calculations both in the perturbative regime and in the non-perturbative regime. The two-photon absorption (TPA) signal is probed by measuring the fluorescence decay of the 5d final state to the ground state. Remarkable is that absorption of the transition frequency $\omega_{5s,5p}$ has no influence on the TPA signal. We find that the linear combination of phase and amplitude in absorption is maintained in the TPA process. The product of the only-phase and only-amplitude TPA measurements is in good agreement with the absorption TPA measurement. In the strong field, a theoretical optimal pulse is designed which holds the ability for complete inversion, due to Rabi-cycling of the state population.

Easily visible femtosecond light pulses are converted to UV, near- and far-infrared radiation by nonlinear processes in birefringent crystals, semiconductors and polymers. For instance, a biased semiconductor illuminated with femtosecond pulses, generates far-infrared (FIR) terahertz (THz) pulses of $\approx 475$ fs with a nearly "white light" spectrum extending from 0.1 - 3 THz (3000 - 100$\mu m$). We realized that the large frequency spread in the THz range is one of the causes why a simple spectrometer has not been developed. The THz radiation spans more than one octave and therefore grating-based spectrometers cannot be used. In **Chapter 5**, a terahertz cesium iodine (CsI) prism spectrometer is designed and tested. This spectrometer can be used as a fast monitor for time-depended studies in large molecules, organic and biological samples. The THz radiation from the emitter is collimated and dispersed by a cryogenically cooled 25 K CsI prism mounted in a cryostat. The FIR spectrum is imaged by a TPX lens onto the Fourier plane where a cooled bolometer is situated. In addition, transmission measurements have been used to obtain the optical properties (absorption and dispersion) in the THz frequency range for CsI, and also KBr and KCl for temperatures between 10 and 300K. The alkali halide crystals become more transparent for electromagnetic radiation at low temperatures. The obtained refractive indices are fitted accurately using a two-term Sellmeier representation. The resolution of a prism spectrometer is dominated by the dispersion. CsI has the largest dispersion, $dn/d\lambda$, of the crystals and is therefore the most useful material for a THz prism spectrometer around 1.0 THz. The spectrum from a THz emitter is measured and transmission spectra of a 300 and 600 GHz frequency selective surface filters. A simple algorithm reconstructs a relative frequency scale and simulates the filter characteristics in good agreement with the experimental results. We find that the CsI prism spectrometer is transparent from 0.2 to 1.1 THz with an overall energy throughput better than 10%. The resolving power is about 35 GHz near 1 THz reducing to 173 GHz at 300 GHz.

The research of my doctoral study started with the construction of a prototype real-time Infrared camera (IR). IR cameras are widely used to monitor temperature differences between objects and record infrared sources such as stars. In **Chapter 6**, we investigate an alternative two-dimensional imaging camera for IR radiation based on a photocathode of gas-phase Rubidium atoms in a highly excited Rydberg state. The Rydberg atoms are used as photo-detectors that operates from 1 - 1000 $\mu m$ and has an exposure time of 10 ns, which removes the need for cryogenic cooling. Although the density of gas-phase atoms ($\approx 10^6\ cm^{-3}$) is very low compared with solid-state detectors, the combination of a low ionization threshold with a high photoionization cross section makes a Rydberg atom a very suitable detector for FIR radiation. The energy barrier is continuously tuneable by choosing the principle quantum number $n$ of the Rydberg state and the strength of the external electric field. In a overview, we present a theoretical background of the far-infrared camera. We discuss the designed open electrostatic optics that extract and image the charge particles from the photocathode onto the particle detector plate. The Rydberg states in Rubidium atoms, and the one-photon photo-ionization and -excitation cross sections are investigated. Calculating the detection efficiency, shows that the camera becomes more sensitive towards lower frequencies. Only tens of nanoJoules of far-infrared radiation is needed to create an image. We have tested the imaging properties, the spatial resolution and distortion with 1064 nm light from a YAG laser. These measurements illustrate that the Rydberg camera is capable of capturing real two-dimensional images.

A far-infrared lens system for imaging objects on the photosensitive layer enables the FIR camera to work as a conventional camera. In **Chapter 7**, we investigate the basics of a camera: The ability to distinguish the shadow cast by an object whenever an obstacle is placed midway between a far-infrared source and the photocathode. As a source, we use broadband coherent terahertz (THz) radiation from a biased semiconductor, illuminated with femtosecond pulses. However, the THz pulses are emitted in the form of half a cycle with a high nonlinear ionization behavior on Rydberg atoms. The unipolar THz pulse is much shorter then the electron orbit time around the core and transfers a momentum ’kick’ to the Rydberg electron. In this way, Rydberg atoms in the photocathode are easily photo-ionized. Hence, the temporal structure of the THz beam determines the ionization and thus the creation of an image, rather than the intensity distribution. However, propagation effects, optical elements and diffraction greatly affects the half cycle pulse (HCP) spectral distribution and thus the HCP temporal profile. For instance, in a freely propagating THz beam, high frequency components remain in the center, while low frequency components are concentrated on the outside. On the outside of the beam, the HCP evolves via a single full-cycle pulse (FCP) into a multi-cycle pulse. We characterize the performance of the Rydberg camera for THz pulses by measuring the intensity-dependence, the spatial resolution, and by the use of lenses. Simple obstacles are placed in the freely propagating THz beam and diffraction greatly affects the half-cycle pulse structure. We verified the Rydberg camera measurements with a linear bolometer detector, which measures the energy of the radiation, irrespective of the THz pulse shape. Model calculations solving the diffraction integrals provide the radiative THz pattern, both in space, time and frequency. We simulate that diffraction reconstruct THz pulses with a nearly half-cycle temporal profile at positions with an experimentally high ionization probability. At positions with an experimental low ionization probability, the simulations show multiple wavefronts behind the main THz pulse. We find a strong correlation between the presence of multiple oscillations in the simulations and suppression of Rydberg ionization in the photocathode of the Rydberg camera. The suppression can be seen as a ”recombination” process. We can conclude that broadband THz radiation is not a good far-infrared source for the Rydberg camera. The nonlinear spatial ionization of THz half-cycle pulses makes the interpretation of the obtained images with the Rydberg camera difficult.

# Samenvatting

## Achtergrond

De interactie tussen licht en materie houdt natuurkundigen al vele eeuwen bezig. In 1873 toonde James Clerk Maxwell aan dat licht electromagnetisch van aard is met een golfachtig gedrag. Licht is een dynamisch elektrisch en magnetisch veld dat elkaar telkens weer opwekt en zich voortplant met de snelheid van het licht van 299 792 458 m/s door vacuum. Echter, Max Planck in 1900 en Albert Einstein in 1905, bedachten dat licht ook beschreven kan worden als een transport van energie in de vorm van massaloze elementaire deeltjes genaamd "fotonen".

De dualiteit van licht is duidelijk door het feit dat het zich voortplant door de ruimte op een golfachtige manier, maar deeltjes gedrag vertoont gedurende het proces van absorptie en emissie in atomen en moleculen. Het golfachtig gedrag van licht(-deeltjes) wordt in kwantum mechanica toegepast op alle deeltjes zoals atomen, elektronen, protonen, enz. Als we onbekend zijn met het golfachtig gedrag van materie in het dagelijks leven, dan is dat omdat de deeltjes golflengte te klein zijn om waargenomen te worden.

Golven zoals in water, maar ook lichtgolven of materiegolven, hebben de mogelijkheid om met elkaar te interfereren. Dit kan zowel: (I) destructief, met als gevolg dat de golven elkaar uit doven, (II) als constructief, met als gevolg dat golven elkaar versterken. Iedere lichtgolf of deeltje kan volledig worden beschreven door een frequentie $\omega$, een amplitude $E$, een fase $\phi$ en een polarisatie $\vec{k}$.

Voor het maken van korte licht pulsen vereist de natuur dat er interferentie plaats vindt tussen vele golven van verschillende frequenties. De interferentie van de vele frequenties is constructief op één moment en destructief op alle andere tijdstippen. Ofwel, korte licht pulsen bestaan uit vele verschillende "kleuren" fotonen. Korte laser pulsen van ongeveer 100 femtoseconde (fs) (1 fs = $10^{-15}$ s ofwel 0.000,000,000,000,001 seconde) met een zeer hoge piek intensiteit kunnen tegenwoordig makkelijk worden gemaakt.

Wanneer atomen of moleculen geëxciteerd worden door zulke korte pulsen dan nemen alle frequenties of fotonen tegelijkertijd deel aan het proces. Belangrijk in het excitatie proces is de reactie van het atoom of molecuul op de optelsom van al deze verschillende fotonen. De uitkomst van de licht-materie interactie wordt sterk beïnvloed door de tijdsafhankelijke pulsstructuur ofwel de onderlinge fase, amplitude en polarisatie van fotonen en minder door de intensiteit van de lichtpuls. Om inzicht te krijgen in het excitatie proces van atomen en moleculen maken we gebruiken van twee beelden: (1) een dynamisch beeld waarin de licht-materie interactie tijdsafhankelijk is en licht een elektrisch veld E(t) is. (2) een statische beeld waarin de licht-materie interactie tijdsonafhankelijk is en licht een verzameling foton $\tilde{E}(\omega)$ is.

De beschikbaarheid van hulpmiddelen voor het experimenteel controleren van de eigenschappen van fotonen $\tilde{E}(\omega)$ in korte licht pulsen geeft de experimentalist een groot aantal "controle knoppen" die het mogelijk maakt om licht pulsen E(t) te vervormen. Als gevolg van het vervormen van korte pulsen wordt de waarschijnlijkheid van een atoom of molecuul om van toestand te veranderen gewijzigd. De manipulatie van deze kwantummechanische interferentie in atomen en moleculen heet "coherent control": de mogelijkheid om kwantummechanische reacties te sturen naar een gewenste eindtoestand via de wisselwerking met licht, terwijl paden naar ongewenste resultaten worden uitgesloten.

In dit proefschrift beschrijf ik de wisselwerking van korte licht pulsen met atomen (rubidium: Rb) en moleculen (stikstofmonoxide: NO). We bestuderen de kwantummechanische interferentie in atomen en moleculen voor de fundamentele kennis van excitatie processen met korte licht pulsen en benadrukken de invloed van pulsvervorming op de uitkomst.

## Femtoseconde gestimuleerde Raman

De eerste stap in een natuurkundig experiment is het beperken van het aantal betrokken moleculaire kwantumtoestanden. Optische excitatie met femtoseconde pulsen is een alternatieve mogelijkheid voor het prepareren van moleculaire kwantumtoestanden. We onderzoeken in **Hoofdstuk 3** het proces van "femtoseconde gestimuleerde Raman" (FSR) in moleculair stikstofmonoxide (NO) als een instrument om selectief rotationele toestanden aan te maken. We maken gebruik van dubbele pulsen om het experiment te manipuleren.

FSR is een twee-foton proces waarin (1) alleen foton-paren binnen de bandbreedte van de femtoseconde puls (2) met een verschil frequentie $\Delta\omega = \omega_p - \omega_s$, (3) gelijk aan een rotationele overgang frequentie $\omega_{J,J'} = \Delta\omega$ in staat zijn om de rotationele populaties in NO te veranderen. De spectrale verdeling van de twee-pulse sequentie vormt een franje-patroon, waarin frequenties aanwezig en afwezig zijn, afhankelijk van de tijdsvertraging $\Delta T$ tussen de twee pulsen.

Aan de hand van onze resultaten kunnen we concluderen dat het mogelijk is om selectief onderscheid te maken tussen twee kwantummechanische paden, waarmee FSR de rotationele ladder beklimt, enkel en alleen door een specifieke tijdsvertraging $\Delta T$ te kiezen tussen de twee pulsen. In het excitatie proces met twee pulsen initieert de eerste puls een "fase klok" $\Delta\phi$ in de geëxciteerde (NO) moleculen. Afhankelijk van de tijdsvertraging van de tweede puls treedt er constructieve of destructieve interferentie op en worden specifieke rotationele toestanden "gevuld" of "geledigd".

We concluderen dat het FSR proces een geschikte methode is om grote hoeveelheden moleculen selectief in een specifieke rotationele toestanden aan te maken.

## Absorptie

Het gebruik van femtoseconde pulsen resulteert in het verlies van spectrale selectiviteit, aangezien alle toestanden binnen de bandbreedte van de puls kunnen worden geëxciteerd. We maken in **Hoofdstuk 4** gebruik van ”natuurlijke” puls vervormingen processen zoals absorptie in gas, om kwantum interferentie te manipuleren.

Door absorptie van enkele frequenties uit de femtoseconde puls ontstaat er elektromagnetische straling achter de oorspronkelijke puls. Deze zogenoemde ”transient” representeert het geabsorbeerde licht. De korte puls blijft nagenoeg hetzelfde en het principe van causaliteit verbiedt een elektrisch veld voor de oorspronkelijke puls. We maken gebruiken van een ”puls vervormer”, gebaseerd op ”vloeibare kristallen”, om absorptie na te bootsen. De lineaire combinatie van een frequentie-afhankelijke fase verdraaiing en verzwakking kan zo afzonderlijk worden bestudeerd. Drie sets van metingen zijn uitgevoerd: (I) fase, (II) verzwakking en (III) beide gecombineerd genaamd absorptie.

In gasvormig rubidium worden de eerste drie energie niveaus ($5s \rightarrow 5p \rightarrow 5d$) gebruikt en we inspecteren alleen het twee-foton absorptie (TPA) signaal van het 5d niveau. Opvallend is dat absorptie van de eerste overgang frequentie $\omega_{5s \rightarrow 5p}$ nauwelijks invloed heeft op de TPA signaal. Dit komt omdat de femtoseconde puls nauwelijks wordt vervormd door absorptie en de excitatie kans naar het 5d niveau blijft nagenoeg hetzelfde. Het elektrisch veld achter de femtoseconde puls werkt alleen tussen het eerste en tweede niveau in rubidium en laat het derde niveau nagenoeg ongemoeid.

Ook vinden we dat het product van de afzonderlijke metingen I) fase en II) verzwakking in goede overeenstemming is met iii) de absorptie meting. Zeer verrassend blijft de lineaire combinatie van een fase verdraaiing en een verzwakking gedurende de metingen gehandhaafd! Het manipuleren van femtoseconde pulsen met absorptie leidt tot meer verrassende effecten.

Theoretisch laten we zien dat een ”ontworpen” puls met een hoge intensiteit de mogelijkheid bezit om alle rubidium atomen in de 5d toestand te brengen door gebruik te maken van Rabi-cycling. Populatie inersie is mogelijk in één snelle puls.

We concluderen dat geëxciteerde toestanden in een multi-level systeem selectief versterkt of verzwakt kunnen worden door middel van het vervormen van femtoseconde pulsen met smal bandige absorptie.

## Een ver-infrarood prisma spectrometer

Femtoseconde licht pulsen worden gemakkelijk geconverteerd naar zichtbare, UV, infrarode en ver-infrarode straling met behulp van kristallen en polymeren. We genereren in een halfgeleider een bijna ”wit licht” spectrum van ver-infrarode straling. De grote bandbreedte is één van de oorzaken waarom een eenvoudige spectrometer nog ontbreekt. Het ver-infrarode spectrum van de puls bezit meer dan één octaaf en daarom kunnen grating spectrometers niet worden gebruikt.

In **Hoofdstuk 5** beschrijven we het ontwerp en de testen van een spectrometer met een cesium jodide (CsI) prisma als dispersief element. Het ver-infrarode spectrum wordt ontrafeld door een cryogeen gekoelde 25 K CsI prisma, gemonteerd in een cryostat, en geprojecteerd door een plastic lens op een gekoelde bolometer detector. De resultaten laten zien dat de CsI prisma spectrometer transparant is van 0,2 tot

1,1 THz met een totale energie transmissie beter dan 10%. Het oplossend vermogen is ongeveer 35 GHz in de buurt van 1 THz en vermindert tot 173 GHz bij 300 GHz. In combinatie met snelle pulsen kan deze prisma spectrometer gebruikt worden als een snelle monitor voor tijdsafhankelijke studies in grote moleculen, organische en biologische monsters.

## De Rydberg camera

Het onderzoek van mijn promotie onderzoekis ooit begonnen met de constructie van een prototype real-time infrarood (IR) camera. Deze IR camera is gebaseerd op een fotogevoelige laag van gasvormige rubidium atomen in een hoog geëxciteerde toestand, ook wel een Rydberg toestand genoemd. Er onstaat een beeld door plaats afhankelijke ionisatie van Rydberg atomen door IR licht.

In **Hoofdstuk 6** beschrijven we de theoretisch achtergrond en de experimentele opstelling van de Rydberg camera. Metingen met infrarode bronnen laten zien dat onze Rydberg camera in staat is om echte twee-dimensionale beelden vast te leggen. Het gebruik van een lenssysteem voor het afbeelden van voorwerpen op de fotogevoelige laag van atomen kan onze Rydberg camera laten werken als een conventionele camera. Infrarode camera's worden op grote schaal gebruikt om temperatuur verschillen tussen voorwerpen te meten en infrarood bronnen zoals sterren te inspecteren.

In **Hoofdstuk 7** gebruiken we breedbandig coherente ver-infrarood als licht bron voor de Rydberg camera. Deze straling heet terahertz (THz) straling. Echter, de THz bron zendt pulsen uit in de vorm van een "halve periode" met een hoog niet-lineair ionisatie gedrag op Rydberg atomen. De unipolaire puls is veel korter dan de omloop tijd van het elektron rond de kern en geeft een impuls "trap" aan het Rydberg elektron.

De impuls trap zorgt ervoor dat Rydberg atomen in de fotogevoelige laag gemakkelijk te foto-ioniseren zijn. Het tijdsafhankelijk elektrisch veld van de THz bundel bepaalt de ionisatie en dus ook de opbouw van een afbeelding. Voortplanting effecten, optische elementen en diffractie beïnvloeden de spectrale verdeling van de "halve periode" puls en daarmee de "halve periode" puls tijdafhankelijke structuur. Het blijkt dat de tijdsafhankelijke elektrisch veld belangerijker is dan de intensiteit van de puls. Bijvoorbeeld, in een vrij propagerende THz bundel bevinden hoge frequentie componenten zich vooral in het centrum, terwijl lage frequentie componenten zich concentreren aan de buitenkant. Naar de buitenkant van de THz bundel evolueert de "halve cyclus" puls via een "volledige cyclus" in een puls met meerdere oscillaties.

Model berekeningen simuleren de voortplanting van de THz bundel in ruimte, tijd en frequentie. We vinden een sterke correlatie tussen de aanwezigheid van meerdere oscillaties in de simulaties en de onderdrukking van de Rydberg ionisatie in de fotogevoelige laag van de Rydberg camera. De onderdrukking van de ionisatie kan worden gezien als een "recombinatie" proces. De aanwezigheid van oscillaties is ruimtelijk terug te zien in de vorm van meerdere golffronten achter de THz bundel.

We concluderen dat breedband THz-straling niet een goede ver-infrarood bron is voor de Rydberg camera. De Rydberg camera is weinig afhankelijk van de intensiteit van de THz bundel. Daaraantegen heeft het onderzoek nieuw inzicht verschaft in de interactie tussen korte THz pulsen en Rydberg atomen.

# Dankwoord

Met trots presenteer ik mijn proefschrift waar ik de afgelopen vier jaar met veel plezier aan heb gewerkt. Het onderzoek aan atomen en moleculen in combinatie met korte pulsen was zeer uitdagend en heeft me veel geleerd. Ik ben dan ook blij met de behaalde resultaten. Uiteraard heb ik het behaalde resultaat niet alleen gedaan en daarom wil ik hier een aantal mensen bedanken.

Allereerst mijn promotor Wim van der Zande. Zonder jouw vertrouwen in mijn promotie was dit proefschift nooit tot stand gekomen. Na eerst drie jaar als technicus te hebben gewerkt in jouw groep op het AMOLF institute in Amsterdam, heb jij me deze unieke kans aangeboden. In die jaren ben ik je passie en gedrevenheid voor de natuurkunde gaan bewonderen. Je inzicht en snelle denken is vaak inspirerend, maar soms ook intimiderend. Je hebt je laboratorium nooit "Zandbak" willen noemen, maar voor mij was het een plek waar ik met fotonen en moleculen heb mogen spelen en waar ik heb geleerd om een onderzoeker te zijn. Jouw inzet in het laatste jaar heeft mij enorm gesteund om vol te houden. Dank je!

Andre van Roij dank ik voor zijn snelle en parate technische steun in het laboratorium tijdens experimenten. Vaak zat er haast achter en wist jij toch een goede oplossing vinden. Helaas dat ons experiment met de MOPO niet is gelukt. Ook de technische kennis van Leander, Danny, Cor heb ik vaak geraad pleegd. Als het om de bolometer ging, kon ik Peter 's avonds laat nog bellen voor hulp. De verhuizing naar het nieuwe 'Huygens' gebouw hebben jullie uitstekend weten te organiseren en de laboratoria waren weer snel opgebouwd.

Daarnaast, dank ik alle (ex)-medewerkers van het departement "Molecule en Laser Fyscia" voor de gezellige werksfeer. Viola, for being my office mate when I just arrived in Nijmegen. Unfortunately, we never painted our office, but your personality and happiness decorated the atmosphere bright and colorful. Annemieke, voor jouw altijd opgewekte humeur dat je mee nam wanneer je weer eens in Nijmegen kwam, Wazzzzzupp? Ivo, met jouw komst was ik niet meer de enige promovendus in onze groep. Je interesse en nieuwsgierigheid waren goed voor vele discussies op de uni, Refter of in het cafe. Helaas was je vaak weg voor experimenten in Dusseldorf, maar altijd met een opgewekte stemming kwam je weer terug in Nijmegen. Ivan voor de gave Planet Rose techno feesten in Doornroosje en Markus voor de leuke avonden bij het Open Podium in Merlijn. Kjeld voor de gezellige koffie pauze in het oude Betagebouw toen jij nog student was en de vele daarna ergens anders. Ook mijn collega's van andere afdelingen en universiteiten wil ik bedanken. Ton voor het doorbreken van een werkdag op de universiteit met een bezoek aan mijn bureau en een uitnodiging voor een kop koffie, lunch of een leuke babbeltje. Mark, bedankt voor het helpen met Latex en het geven van onderdak toen mijn verwarming was uitgevallen! Bart, Jisk, Rob, Comrad Anna, Elena, Hilje, Igor, Tim en Margriet voor de leuke avonden en nachten in de stad. During experiments at the University of Bochum in the group of Prof. Havenith, I had a really nice time working together with Erik, Matthias and Benjamin. Thank you for the opportunity to work with a THz-TDS system and saving me late at night, when I had locked myself up in your University.

Met plezier denk ik terug aan de jaren op het AMOLF instituut in de groep Atmospheric Physics met Hester, Andreas, Anouk, Annemieke, Justin, Rüdiger, Laura en Ben. Nooit waren lunches zo gezellig en feestelijk als toen met jullie! Hinco, Rob en Ad bedank ik voor hun technische ondersteuning en de altijd prettige samenwerking. Gedurende mijn promotie in Nijmegen heb ik vaak het AMOLF-instituut bezocht voor overleggen en experimenten. De vertrouwde sfeer in de gangen is er nog altijd en bijna familiaire wanneer je werd ontvangen bij de balie door Trees. Joep, Han-Kwang en Mischa wil ik bedanken voor hun hulp bij de THz-TDS metingen aan de alkali kristallen en hun opbeurende woorden nadat ik de bolometer van tafel had laten vallen. Marc Duursma voor het regelen van de Helium vaten die dan klaar stonden voor gebruik als ik weer eens kwam. Marc en Arjan dank ik voor de vruchtbare discussies en hulp bij de analyse van het NO experiment. Arjan, je toeristische huis in Marken was een mooie plek om aan het artikel te werken. Per en Wing Kiu voor de nachtelijke uren experimenteren bij de XFEL-DESY en de gezellige dag in Hamburg. Mijn begeleider tijdens mijn HBO-stage op het VU in Amsterdam, Wim Roeterdink, wil ik hierbij bedanken voor zijn duwtje in de goede richting naar een promotie.

Op deze plek wil ook mijn familie en vrienden bedanken voor hun steun en toeverlaat tijdens mijn promotie. Allereerst mijn moeder Victoria die een voorbeeld is voor mij in het verzetten van bergen. Hennie, voor jou altijd eerlijke, scherpe en verhelderde visie op het leven. Mijn broers, Mardino voor zijn onbevangen uitspraken en Arjuna voor zijn wijze en handige hulp, Paul voor zijn doordachte adviezen en Julio voor de fijne tijd dat ik bij jou mocht logeren wanneer ik in Amsterdam moest werken. Ja toch! Sandra, Ester, Suzanne, Eugene en Marlies, bedankt voor jullie aanstekelijke vrolijkheid. De Annegarns wil ik bedanken dat ze mij onvoorwaardelijk hebben opgenomen in hun familie en mij altijd hebben laten zien en voelen dat ik er bij hoor. Frans, bedankt voor de tijd die we samen hebben gedeeld. Guuske voor al jouw jaren van vriendschap met leuke avonturen. Kevin voor het zijn van een broer voor mij en Wybeke voor jouw altijd fijne sfeer. Bart, omdat jij er was wanneer ik weer iets had ontdekt en het dan samen met jou mocht vieren. Meredith, for our Lego time together and your keen eye on my thesis. Stikko, voor de geweldige vrijbuiters tijd samen in Den Haag. Yori, Sanka, Christine, Ester, Dumky en Hinco, bedankt voor de gezellige tijd samen. Zahara, thank you for our amazing time together in Nijmegen, see you around Chatta! Erik-Jan en Jeanette, bedankt dat jullie deur altijd open staat. Aan mijn oud-huisgenoten Mark, Inge, Nathalie en Eef op de Weurtseweg voor de geweldige tijd, de fijne gesprekken in de keuken of aan tafel met een goed glas wijn en de leuke feesten in huis of in de stad.

Het laatste jaar van mijn promotie, waarin mijn oudste broer Mardino is overleden was erg moeilijk en zwaar. Velen van jullie, ook die ik hier niet persoonlijk heb genoemd, hebben er voor gezorgd dat ik me gesteund heb gevoeld en mijn promotie heb kunnen afronden. Ik dank jullie allen! Zo ook de verschillende organisaties, zoals de Glind, en alle lieve mensen die mij en mijn broers hebben opgevangen en verzorgd. Marian en Paul, Annemieke en Martin, Ankie en Biki, mede dankzij jullie is het mogelijk geworden dat ik promoveer.

Als laatste aan mijn mooie lieve vriendin en aanstaande vrouw, Wieneke, dank je voor al jouw liefde, geduld en zorg in de stressvolle tijden. Jou aanmoedigingen en steun zijn onmisbaar geweest.

# Curriculum Vitae

| | |
|---|---|
| 2008 - | Postdoctoral position at the Department of Applied Molecular Physics, Radboud University Nijmegen.<br>Title project: *Construction and measurements of coherent Rayleigh Brillouin scattering.* |
| 2003 - 2008 | PhD Student at the Department of Molecular and Biophysics, Radboud University Nijmegen.<br>Title thesis: *Coherent far-infrared excitation processes with ultrafast pulses in multilevel systems.* |
| 2000- 2003 | Technical engineer at the department of Atmospheric Physics, AMOLF institute in Amsterdam.<br>Title project: *Rubidium atoms as Far-infrared detector.* |
| 1996 - 2000 | Bachelor Applied Physics, Technische Hogeschool Rijswijk. Bachelor project at the department of Physical Chemistry, Vrije Universiteit Amsterdam: *Development of a non-linear optical parametric amplifier (NOPA).* Apprenticeship at the department of Technische Physische Dienst, TNO Delft: *Development of an automized tulp harvester* and at the department of DIMES-Nano Facility, TU Delft: *Scanning Tunneling Microscopy.* |
| 1993 - 1996 | MTS Photonics, Technische College Ede. |
| 1989 - 1993 | MAVO, Don Bosco Leusden. |